ABSTRACT

Title of Document: MEMS SENSOR PLATFORMS FOR *IN SITU* CHARACTERIZATION OF LI-ION BATTERY ELECTRODES

Hyun Jung, Doctor of Philosophy, 2016

Directed By: Professor Reza Ghodssi, Department of Electrical and Computer Engineering

Lithium-ion batteries provide high energy density while being compact and light-weight and are the most pervasive energy storage technology powering portable electronic devices such as smartphones, laptops, and tablet PCs. Considerable efforts have been made to develop new electrode materials with ever higher capacity, while being able to maintain long cycle life. A key challenge in those efforts has been characterizing and understanding these materials during battery operation. While it is generally accepted that the repeated strain/stress cycles play a role in long-term battery degradation, the detailed mechanisms creating these mechanical effects and the damage they create still remain unclear. Therefore, development of techniques which are capable of capturing in real time the microstructural changes and the associated

stress during operation are crucial for unravelling lithium-ion battery degradation mechanisms and further improving lithium-ion battery performance. This dissertation presents the development of two microelectromechanical systems sensor platforms for *in situ* characterization of stress and microstructural changes in thin film lithium-ion battery electrodes, which can be leveraged as a characterization platform for advancing battery performance.

First, a Fabry-Perot microelectromechanical systems sensor based *in situ* characterization platform is developed which allows simultaneous measurement of microstructural changes using Raman spectroscopy in parallel with qualitative stress changes *via* optical interferometry. Evolutions in the microstructure creating a Raman shift from 145 cm^{-1} to 154 cm^{-1} and stress in the various crystal phases in the $Li_xV_2O_5$ system are observed, including both reversible and irreversible phase transitions. Also, a unique way of controlling electrochemically-driven stress and stress gradient in lithium-ion battery electrodes is demonstrated using the Fabry-Perot microelectromechanical systems sensor integrated with an optical measurement setup. By stacking alternately stressed layers, the average stress in the stacked electrode is greatly reduced by 75% compared to an unmodified electrode. After 2,000 discharge-charge cycles, the stacked electrodes retain only 83% of their maximum capacity while unmodified electrodes retain 91%, illuminating the importance of the stress gradient within the electrode.

Second, a buckled membrane microelectromechanical systems sensor is developed to enable *in situ* characterization of quantitative stress and

microstructure evolutions in a V_2O_5 lithium-ion battery cathode by integrating atomic force microscopy and Raman spectroscopy. Using dual-mode measurements in the voltage range of the voltage range of 2.8V – 3.5V, both the induced stress (~ 40 MPa) and Raman intensity changes due to lithium cycling are observed. Upon lithium insertion, tensile stress in the V_2O_5 increases gradually until the α- to ε-phase and ε- to δ-phase transitions occur. The Raman intensity change at 148 cm^{-1} shows that the level of disorder increases during lithium insertion and progressively recovers the V_2O_5 lattice during lithium extraction. Results are in good agreement with the expected mechanical behavior and disorder change in V_2O_5, highlighting the potential of microelectromechanical systems as enabling tools for advanced scientific investigations.

The work presented here will be eventually utilized for optimization of thin film battery electrode performance by achieving fundamental understanding of how stress and microstructural changes are correlated, which will also provide valuable insight into a battery performance degradation mechanism.

MEMS SENSOR PLATFORMS FOR *IN SITU* CHARACTERIZATION OF LI-ION BATTERY ELECTRODES

by

Hyun Jung

Dissertation submitted to the Faculty of the Graduate School of the
University of Maryland, College Park, in partial fulfillment
of the requirements for the degree of
Doctor of philosophy
2016

Advisory Committee:
Professor Reza Ghodssi, Chair
Professor Christopher Davis
Professor Martin Peckerar
Professor Alireza Khaligh
Professor Ian White

Dedication

To my wife Jiyoung, my daughter, Yehna, my parents, and my older brother and his family, for their love and support throughout the years. Without them, none of this would have been possible.

Acknowledgements

I would like to thank my advisor Professor Reza Ghodssi for his continuous guidance and support throughout the course of this work. I would also like to thank the members of the Ph.D. dissertation committee, Professor Christopher Davis, Professor Martin Peckerar, Professor Alireza Khaligh, and Professor Ian White for their suggestions and discussions leading to the completion of this work.

A huge acknowledgement is dedicated to all the past and present members of the MEMS Sensors and Actuators Lab (MSAL) for all of their help, advice, and useful discussion. I have been fortunate to have many supportive colleagues and mentors. I would like to thank Mr. Sergio Baron, Dr. Ekaterina Pomerantseva, and Dr. Markus Gnerlich for their assistance and guidance. Particularly, I would like to thank Dr. Konstantinos Gerasopoulos for his guidance and support throughout the times when I was going through difficulties in designing my platforms. I especially thank Thomas Winkler and Sowmya Subramanian, who not only reviewed my writings but also gave constructive suggestions. I also extend thanks to my collaborators on this research, Professor Gary Rubloff and his group members (Dr. Chuan-Fu Lin and Dr. Chanyuan Liu) for providing generous help when necessary and Dr. A. Albert Talin for providing thoughtful discussion and guidance on my work.

I would like to also acknowledge the support I received in the fabrication and characterization from the Maryland NanoCenter staff members (Dr. Jim O'Connor, Mr. Thomas Loughran, Mr. John Abrahams, and Mr. Jonathan Hummel, and Mr. Mark Lecates) and Surface Analysis Center (Dr. Karen Gaskell).

Lastly, this dissertation would have not been possible without funding from the Nanostructures for Electrical Energy Storage (NEES), an Energy Frontier Research Center funded by the U.S. Department of Energy, Office of Science, Basic Energy Sciences.

Table of Contents

List of Tables

List of Figures

Chapter 1: Introduction

1.1 Motivation and background

Lithium-ion batteries (LIBs) are the most pervasive energy storage device providing high energy density while being light-weight and compact, powering a variety of devices such as laptops, smartphones, and tablet computers. Recently, new electric transportation systems including hybrid electric and fully electric vehicles require rechargeable batteries to have even higher energy density and longer cycle life as well as lower cost and improved safety [1]. Therefore, a considerable amount of research has been directed towards developing new electrode materials in order to provide even higher capacity, maintaining long cycle life. A major challenge in these efforts has been characterizing and understanding these materials while batteries are in a state of operation.

Most LIB electrode materials react with Li-ions *via* intercalation into interstitial sites or channels within the host lattice or by alloying mechanism with the electrode material [1,2]. While it is generally accepted that the repeated strain/stress cycles play a role in the long-term battery degradation, the detailed mechanisms still remain unclear [3–6]. Therefore, measurement techniques which are capable of acquiring the microstructural changes and associated stress in real time are crucial for identifying underlying mechanisms of LIB degradation and advancing battery performance.

A variety of chemical and physical processes take place. These include lithium intercalation, volume changes, and crystal phase (hereafter simply

‘phase’) transitions/transformations, which render battery systems more complicated and difficult to understand. *In situ* methods allow direct monitoring of these phenomena and offers the capability to directly link these processes to the electrochemical response of the battery. In the context of batteries, “*in situ*” refers to measurements taken on materials in their original position (*i.e.* inside the device) without disassembling the battery itself [7], which allows more realistic characterization of the batteries. By contrast, *ex situ* measurements take place only after disassembling the battery which can lead to contamination during sample preparation and handling between battery use and characterization.

However, conducting *in situ* experiments can be challenging since batteries must be fully operational under the circumstances imposed by the monitoring tool, which often demands specially designed devices, packaging methods, and measurement setups, thereby preventing straightforward application of *in situ* techniques. Advantageously, in the past few years, significant progress has been made with new, more advanced, *in situ* techniques. Among these, the multi-beam optical stress sensor (MOSS) [8] has proven to be an effective method for characterizing the stress evolution in LIB thin film electrodes during cycling. While the technique has proven to be advantageous for mechanical characterization, the limited ability to directly access the electrode restricts its potential integration with other methods that could provide microstructural and chemical composition information. In addition to stress characterization, significant advances have been achieved in *in situ*

microstructural characterization of LIB electrodes. For example, *in situ* transmission electron microscopy (TEM) [9] provides direct imaging of the microstructural changes of individual nanowire or nanoparticle electrodes with near-atomic resolution in real time. Crystallographic changes which occur inside the battery electrode as it is lithiated and delithiated have also been investigated using *in situ* X-ray diffraction [10] (XRD) and absorption methods [11]. Nevertheless, these methods are restricted to providing only structure or phase evolutions of the electrode during lithium cycling.

This work addresses the aforementioned limitations through the utilization of microelectromechanical systems (MEMS). MEMS technology holds great potential for studying Li-ion battery electrodes. It has been used to characterize mechanical properties of various thin film materials due to its high sensitivity and accuracy [12]. MEMS sensors are compact and light weight, which enables them to be packaged in various forms such as Teflon and coin cells [13,14]. These features of MEMS provide versatility to tailor the experimental setups in less restricted ways, while allowing precise measurement results. In this work, a Fabry-Perot MEMS sensor and a buckled membrane MEMS sensor platforms are designed to enable multi-modal, real-time monitoring of stress and microstructure changes, which are critical factors affecting LIB performance. Additionally, the Fabry-Perot MEMS sensor is utilized to study impact of electrochemically-driven stress and stress gradient in LIB electrode to provide additional insights into the battery degradation

mechanisms. Particular emphasis is placed on the design, fabrication, and packaging of the MEMS sensors which are critical factors enabling the integration of the MEMS sensors with scientific equipment. Moreover, a significant amount of effort is focused on the working principle of the integrated platforms to demonstrate unique advantages of the integrated platforms offering *in situ* analysis on the stress changes and characterization of the microstructural evolutions in different phases of the LIB electrode in a unified setup.

The detailed research goals of this dissertation are: (1) to develop and fabricate MEMS sensors as a key enabling factor for building novel platforms for battery research, (2) to integrate the MEMS sensors with scientific equipment to demonstrate multi-modal, *in situ* characterization platforms for thin film LIB electrodes, (3) to provide additional insights into battery degradation mechanisms by investigating critical factors affecting LIB performance. By selecting a complex $Li_xV_2O_5$ model electrode to demonstrate the utility of the integrated platforms, demonstrating its applicability to other battery electrode materials. Thus, the approaches demonstrated in this work are expected to open up new avenues to investigate critical factors affecting LIB performance.

1.2 Thesis contributions

The research described in this dissertation seeks to utilize the advantages of MEMS technology to develop novel experimental platforms for *in situ* characterization of LIB electrodes. The MEMS sensors are a key contributing factor which enable the *in situ,* multi-modal characterization platforms. This

dissertation contributes to the field of battery research by demonstrating the MEMS sensors integrated with different measurement setups can be utilized in the following aspects:

1.2.1 In situ characterization of qualitative stress and microstructural changes in LIB electrode

Lithium insertion/extraction into/from different host materials is generally accompanied by strain of the host material, causing stress which can lead to degradation of the battery performance. Therefore, characterizing the microstructural changes and associated stress remains a key need for developing high-performance batteries, which has been mainly limited to providing either the structural or stress changes for battery research.

This dissertation demonstrates a novel platform which integrates a Fabry-Perot MEMS sensor with a commercially available Raman microscope which allows simultaneous measurement of microstructural changes using micro-Raman (μRaman) spectroscopy in parallel with qualitative stress changes *via* optical interferometry. Characterization of the evolution in microstructure and stress in various crystal phases in the Li-V-O system is achieved, including both reversible and irreversible phase transitions. Also, spectral shifts in certain Raman active modes are correlated with changes in the electrode stress, confirming previously hypothesized origins of these observations.

1.2.2 Investigation of battery degradation mechanism using Fabry-Perot MEMS Sensor

Continuous volume expansion/contraction-induced stress in LIB electrodes gradually deteriorates battery performance. Therefore, considerable efforts have been made to study *in situ* stress evolution. However, the stress gradient in the electrode and its effect in the battery performance has largely remained unknown since it can only be studied using finite models or numerical simulations. Therefore, there is a need for development of techniques for controlling the stress and stress gradient in LIB electrodes and investigating their relationship with battery degradation mechanisms.

In this part of the work, the stress and stress gradient in a V_2O_5 cathode are modified *via* combining two different crystal phases of the electrode material for investigation of battery degradation mechanisms. The crystal phase-dependent stress changes in the V_2O_5 cathode are characterized *in situ* using the Fabry-Perot MEMS sensor integrated with an optical measurement setup. By stacking alternately stressed layers, the average stress in the electrode is greatly reduced by 75% while a high stress gradient is believed to be induced at the boundary of the layers. This method provides a unique opportunity of exploring effects of the stress and stress gradient on LIB battery performance which have not been achievable previously.

1.2.3 In situ characterization of quantitative stress and microstructural changes in LIB electrode

While the Fabry-Perot MEMS sensor integrated with the Raman spectroscopy setup offers unique advantages in terms of characterizing LIB electrodes, the stress changes studied with the platform remain qualitative. This prevents more detailed investigations such as fracture energy or stress-potential coupling of the lithiated electrode, which can only be deduced from measuring stress changes in the electrode quantitatively.

In order to address this limitation, a buckled membrane MEMS sensor is developed and integrated with equipment capable of performing atomic force microscopy (AFM) and Raman spectroscopy measurements in a unified setup. The buckling height changes are measured using AFM, enabling quantification of the stress changes in the electrode. At the same time, Raman spectroscopy is utilized to probe the electrode in order to examine the microstructural changes during battery operation. Thus, the buckled membrane MEMS sensor platform demonstrates a new technique which can simultaneously analyze the two critical factors related to battery degradation mechanisms. This experimental platform can be utilized for optimization of the thin film battery electrode performance by achieving a fundamental understanding of how the stress and the microstructural changes are correlated.

1.3 Literature review

1.3.1 Li-ion battery principle of operation

Secondary (rechargeable) Li-ion batteries are the most popular energy storage devices which provide high gravimetric/volumetric capacity, high power rates, low self-discharge and low maintenance requirements [15–18]. Commercially available Li-ion batteries are mostly composed of a carbonaceous anode (generally graphite), an anode current collector, an organic electrolyte with a Li-containing salt (*e.g.* $LiPF_6$), a lithium metal oxide cathode (*e.g.* $LiCoO_2$ or $LiMnO_2$), and a cathode current collector as shown in Figure 1-1.

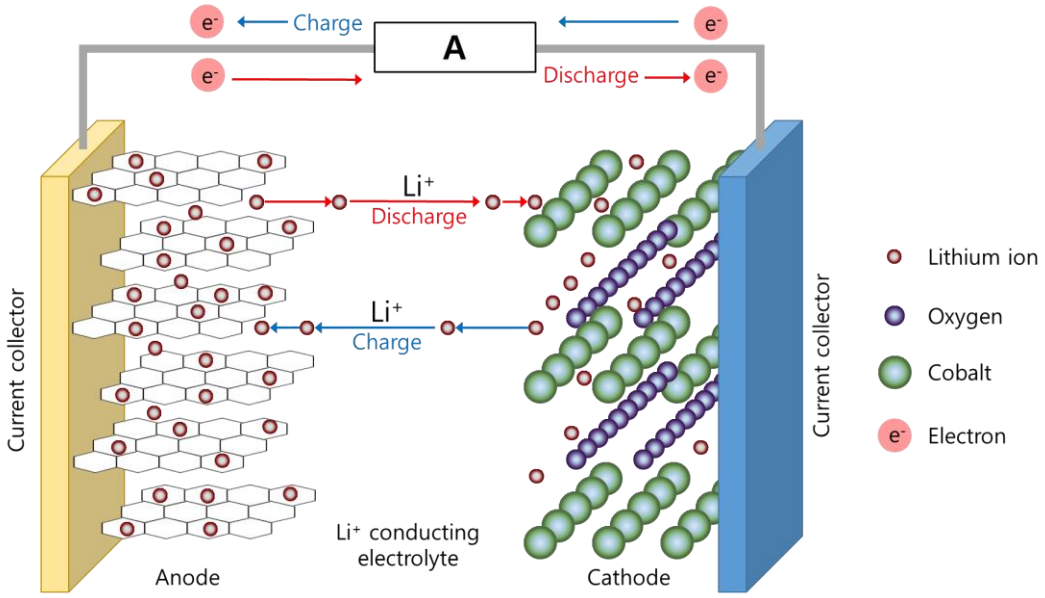

Figure 1-1: Schematic diagram drawing of a conventional Li-ion battery showing the anode, cathode and electrolyte. When the cell is charged, Li-ions are extracted from the cathode, transported through the Li-ion conducting electrolyte, and inserted into the anode. When discharging, the Li-ions are extracted from the anode and inserted into the cathode while migrating through the electrolyte under an opposite electrochemical potential gradient.

Reversible insertion/extraction into/from an electrode material during the discharge/charge process occurs in Li-ion batteries. The lithium insertion/extraction process occurs with a flow of ions through the electrolyte, which is accompanied by a reduction/oxidation (redox) reaction of the host matrix assisted with a flow of electrons through the external circuit [19].

Recently, alloying anodes such as Si, Sn, Sb, Al, which form alloys with lithium, have received significant attention since they can provide much higher specific capacity compared to the commercially available graphite anode (372 mAh g^{-1}) [20–22]. Unfortunately, these alloying anodes are accompanied by large volume changes during lithium cycling which lead to a large irreversible capacity loss at the initial cycle and poor cycling behavior. However, it is reported in literature that properly designed microstructure can reduce the electrode degradation due to the volume changes during discharge (lithiation) and charge (delithiation). As an example, silicon has been considered as one of the most promising anode materials due to its very high gravimetric and volumetric capacity. Silicon, which is abundant and environmentally safe [23,24], has a theoretical specific capacity of 4212 mAh g^{-1} when it forms a fully lithiated alloy ($Li_{4.4}Si$). Its commercial use in rechargeable Li-ion batteries has been limited by the poor cycling stability of bulk silicon. During lithiation, the large volume change (> 300%) induces high internal stress, pulverization of the electrode and subsequent loss of electrical contact between the electrode and current collector. As the electrode loses its electrical connection, it can no longer

participate in the electrochemical reaction which causes poor reversibility and rapidly declining capacity [25]. Adapting nano-scale morphologies has the potential to solve this limitation by accommodating the large stresses associated with the expansion and contraction inside the electrode during electrochemical cycling.

A number of morphologies have been investigated to minimize electrode pulverization and capacity loss in silicon, including thin films, and nano-scale materials [26,27]. These morphologies improve cycling stability by incorporating pores and voids to accommodate volume expansion, or by utilizing high surface-to-volume ratio to manage the internal stress. Amorphous thin silicon films (> 200 nm) have demonstrated the highest capacities and longest cycle lives. Scanning electron and optical microscope observation of electrochemically cycled thin films have revealed that the cracked films, which form islands resembling mudflats, remain attached to the substrate after lithium extraction. Figure 1-2 shows the morphology of a thin silicon film after cycling [28]. The active material can be cycled without additional cracking after initial fracture occurs in early cycles. Thin silicon films with optimized thickness retain their capacity after capacity loss at the first cycle since electrical contact between the active material and the current collector is maintained.

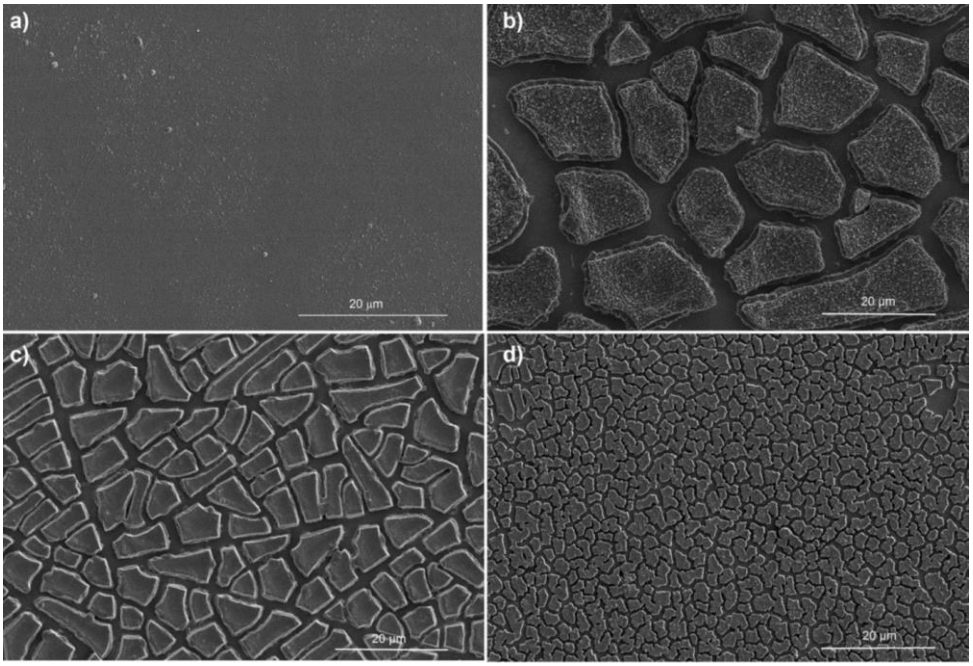

Figure 1-2: (a) SEM image of a 500 nm silicon film before electrochemical cycling; (b)-(d): cracking patterns formed on silicon films of different thicknesses: (b) 1000 nm thick, after 5 cycles, (c) 500 nm thick after 5 cycles, (d) 200 nm thick, after 10 cycles [28]. (Reprinted with permission from J. Li, A.K. Dozier, Y. Li, F. Yang, and Y.-T. Cheng, *Journal of The Electrochemical Society*, 158, A689 (2011), Copyright 2011, The Electrochemical Society)

Silicon is an exemplary case which indicates the importance of correlating electrode microstructure and stress with device performance. This information also demonstrates the optimized microstructure of the material can be efficiently used to fully utilize its promising potential. However, as illustrated in Figure 1-2, a forensic, destructive examination of the electrode is generally needed to provide this correlation. Little has been reported on the *in situ* measurement of mechanical, compositional and structural parameters, despite their general recognition as major factors in the degradation of battery performance. To improve battery life, it is important to understand how materials change during

each cycle and degrade over time inside an actual battery cell. Therefore, *in situ* measurement techniques are needed to enable real-time identification of operational parameter contribution to battery failure (*i.e.* current and voltage range used), as well as enable understanding of dynamic changes of stress and microstructure during electrochemical charge/discharge. The understanding of such changes could be applied to the design criteria for various electrode systems.

Throughout this work, thin film Vanadium pentoxide (V_2O_5) is selected as a model electrode to demonstrate the capability of the MEMS sensor platforms. V_2O_5 is an attractive material as cathode in LIB due to its high capacity. It can accommodate up to three lithium ions per mole of oxide, providing a specific capacity of 450 mAh g^{-1} within the voltage range from 1.5V – 4V [3,29–31]. The electrochemical performance of LIB electrodes are strongly dependent on the structural changes caused by the lithium insertion/extraction process, and considerable efforts have been made to study the structural dependent characteristics of V_2O_5 and its lithiated $Li_xV_2O_5$ phases, which make it suitable for verifying the feasibility of the MEMS sensor platforms.

1.3.2 Advantages of utilizing MEMS technology

MEMS is a relatively new technology aiming towards the miniaturization of sensors, actuators and systems. MEMS stems from the same technologies that produced transistors, which subsequently revolutionized the electronic industry. The term MEMS is now widely applied to a wide variety of miniaturized devices mostly fabricated from silicon using techniques that are adapted from the

microelectronics industry. These techniques are isotropic and anisotropic etching, various thin film deposition methods, wafer bonding, masking and doping. The main advantage of MEMS technology is that the scaling properties of the different structural materials and transduction mechanisms (*e.g.* electrical, magnetic, thermal etc.) allow MEMS devices to be smaller, lighter, more energy-efficient, and more sensitive than their macroscopic counterparts [19]. MEMS technology has been extremely successful in the context of physical sensing and has produced a wide range of small and inexpensive devices such as accelerometers, strain gauges, microphones, pressure sensors, and many more [32].

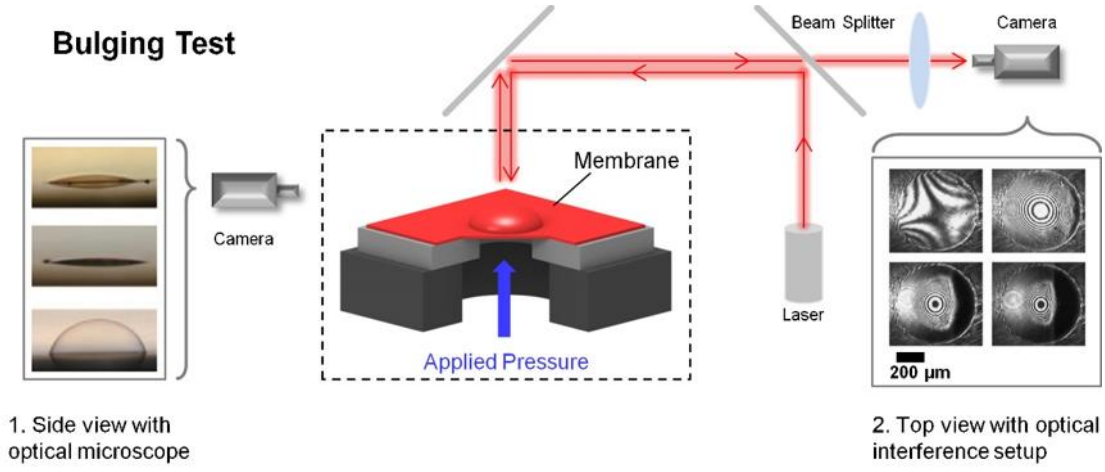

Figure 1-3: Micromechanical characterization of nano-membranes. A bulging test measures the response of a suspended membrane to an overpressure. The membrane deflection is measured to produce a pressure versus deflection curve, from which mechanical parameters can be extracted. The deflection can be measured optically either by viewing the film from the side (left) or by using an interferometry setup (right). The rings of the interference pattern can be correlated to the membrane deflection [33]. (Reprinted with permission from W. Cheng, M.J. Campolongo, S.J. Tan, and D. Luo, *Nano Today*, 4, 482 (2009). Copyright 2009, Elsevier)

An important aspect in MEMS technology is to increase the reliability of the devices, which largely depends on understanding the mechanical properties of the component materials [34–36]. However, standard methods for characterization of materials have not yet established. For the purpose of mechanical characterization of active materials, many efforts are under way by different research groups to investigate the mechanical properties on free standing thin films utilizing MEMS technology [37]. Typical methods impose a fixed displacement on MEMS fabricated devices (*e.g.* cantilever and membrane) using a nano-positioning motor or an on-chip actuator and measure the load as shown in Figure 1-3.

A pressure is applied to one side of a clamped membrane, causing the membrane to expand in the opposite direction. The relationship between the pressure difference and the observed membrane deflection is recorded. By analyzing the load-deflection behavior of the film, biaxial modulus and in-plane residual stress can be extracted. These techniques show that MEMS devices have distinctive capabilities, making them capable of characterizing free standing thin films with greater sensitivity and precision.

Utilization of MEMS technology in characterizing Li-ion battery electrodes has been demonstrated as well [13,38–41]. During battery operation, Li-ion battery electrodes experience compressive/tensile stress due to volume expansion (and contraction) induced by Li-ion insertion/extraction as explained in the previous section. A cantilever or membrane fabricated using MEMS

technology and coated with Li-ion battery electrodes on one side is small enough to be embedded in Li-ion battery cells. The stress changes in the Li-ion battery electrodes during battery operation cause deflection due to the stress gradient along the devices. The deflection of the devices are generally measured using optical methods in order to analyze the stress changes in the Li-ion battery electrode during battery operation. However, the analysis has been limited to the stress changes in the electrode. But it has not been able to demonstrate simultaneous quantitative stress and microstructure changes in the electrode as discussed in more detail later.

1.3.2 Membrane theory

Membranes are an important mechanical basic element in MEMS. They are made out of silicon, silicon dioxides, silicon nitrides, polymers, and metals. The thickness of typical membranes are in the range of 0.5-500 μm. The lateral dimensions of the membranes are in the range of 100 μm and 10 mm. In general, there are two types of membranes which are frequently used in MEMS Thick and thin membranes as shown in Figure 1-4.

A membrane is called thick when its maximum deflection (w_0) is smaller than its thickness (d_M). When the deflection is larger than the thickness, it is called thin membrane [42]. A thick membrane is sometimes called a plate as well. These membranes can be used for a multitude of applications such as pressure sensors, switches, microvalves, and micro-pumps [43]. In this work, the thick membrane is utilized for characterizing mechanical and microstructural changes

in Li-ion battery electrodes. The thick membrane is chosen over other candidate platforms since it has distinct advantages: first, it is easier to fabricate compared to other microstructures such as cantilevers since membranes do not suffer from stiction and experience less fracture. Another advantage is that it can separate the measurement side from the battery side and as such it enables Raman spectroscopy of the active battery material underneath the membrane for characterizing microstructural changes without fluorescence generated from an electrolyte. An organic electrolyte, which is frequently used for Li-ion battery operation, creates a much more intense signal compared to the Raman signal when it is exposed to laser light, and this can limit Raman utilization.

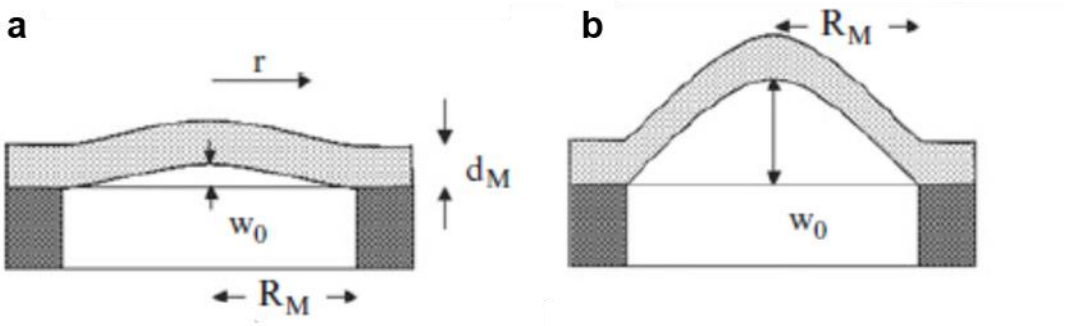

Figure 1-4: Simple schematic showing (a) thick and (b) thin membranes [42].

1.3.3.1 Membrane buckling

Buckling is a mechanical phenomenon which can occur in structures such as beams or membranes. When the compressive stress in the structure becomes high, the structure becomes unstable. When the compressive stress in the structure reaches a critical stress, the membrane will buckle vertically without applying any external load. The buckling phenomenon is a result of two

competing effects. The first effect is the tendency of a membrane structure to release the compressive stress by an out-of-plane deflection. The second effect is the restoring force which tends to drive the deflected structure to move back to its flat position due to a flexural rigidity of the structure. The buckled membrane has a lower total strain energy compared to the simply compressed state [44–46].

Buckling of the membrane has been utilized in the literature in the form of MEMS-based switches, micro-pumps, and mechanical memory devices due to its bi-stable nature and ability to translate small in-plane strain into relatively large vertical displacement, particularly useful in sensing and actuation for microsystems [45]. In this work, the membrane will be designed to translate the residual stress changes in Li-ion electrode into corresponding vertical displacement changes in the membrane. Therefore, it is a primary concern to calculate the buckling height (w_0) due to the stress in the membrane. Since buckling of the membrane is a specific status of a general membrane behavior, the buckling height can be derived from an equation which describes the relationship between the pressure drop (Δp) and the membrane deflection [42]

$$\Delta p = \frac{4 d_M w_0}{R_M^2}\left(\frac{4}{3}\frac{d_M^2}{R_M^2}\frac{E_M}{1-v_M^2} + \sigma_0 + \frac{64}{105}\frac{w_0^2}{R_M^2}\frac{E_M}{1-v_M^2}\right) \qquad (1)$$

where E_M, v_M, R_M, and σ_0 are the Young's modulus, Poisson's ratio, radius, and residual stress of the membrane, respectively. The buckling height of a membrane can be calculated by inserting a pressure drop equal to zero into (1)

$$\Delta p = 0 = \frac{4 d_M w_0}{R_M^2}\left(\frac{4}{3}\frac{d_M^2}{R_M^2}\frac{E_M}{1-v_M^2} + \sigma_0 + \frac{64}{105}\frac{w_0^2}{R_M^2}\frac{E_M}{1-v_M^2}\right) \tag{2}$$

Equation (2) can have three different solutions with respect to w_0

$$w_0 = 0 \tag{3}$$

and

$$\frac{4}{3}\frac{d_M^2}{R_M^2}\frac{E_M}{1-v_M^2} + \sigma_0 + \frac{64}{105}\frac{w_0^2}{R_M^2}\frac{E_M}{1-v_M^2} = 0 \tag{4}$$

which leads to

$$w_0 = \pm\frac{\sqrt{35}}{4} d_M \sqrt{\frac{\sigma_0}{-\frac{4}{3}\left(\frac{d_M^2}{R_M^2}\right)\left(\frac{E_M}{1-v_M^2}\right)} - 1} \tag{5}$$

The first solution (3) corresponds to a flat membrane. On the other hand, equation (5) describes the deflection of a bi-stable membrane, which can deflect either up or down, induced by the compressive stress in the membrane as shown in Figure 1-5.

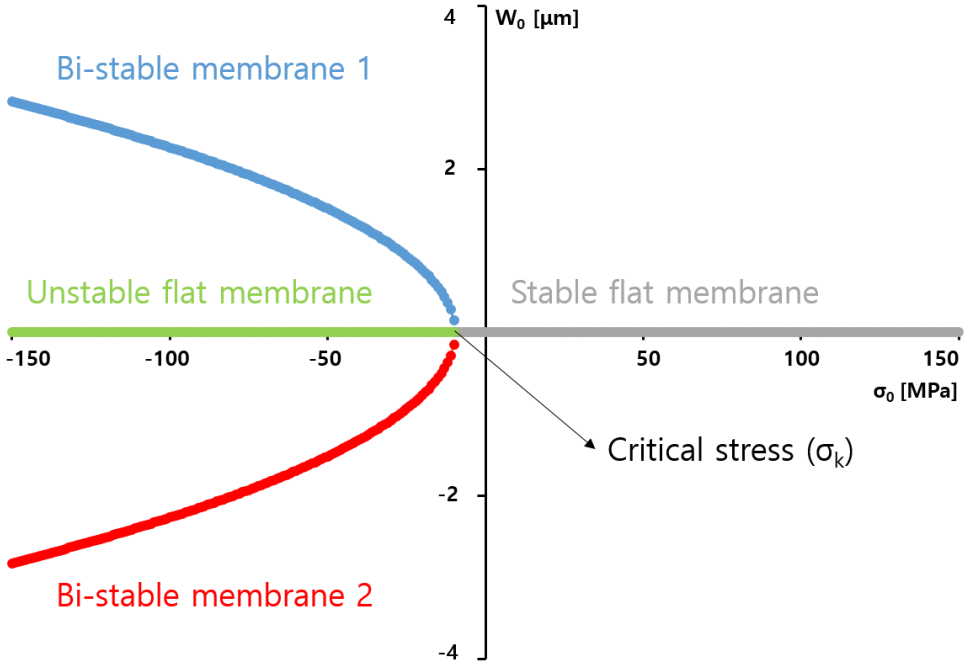

Figure 1-5: Deflection of a circular membrane as a function of its residual stress.

The denominator under the square root in equation (5) is the critical stress, and this solution allows proper result only if the residual stress is more compressive than the critical stress. Equation (3) satisfies all residual stress states of the membrane. However, it is the only solution when the residual stress is more tensile than the critical stress. In fact, it is the only solution since the term under the root in equation (5) becomes negative. Therefore the membrane becomes stable flat membrane (Figure 1-5). When the residual stress becomes

more compressive than the critical stress, the membrane can either deflect up/down (Figure 1-5 (Bi-stable membrane 1 and Bi-stable membrane 2)) or stay flat (Figure 1-5 (Unstable flat membrane)).

One aspect that needs to be noticed here is that all the equations shown above are derived under the assumption that the membrane is composed of a single layer. However, as shown in our previous work [13], the membrane structure needs to be composed of different layers in order to perform electrochemical tests as a Li-ion battery. Therefore, a proper approach should be used in order to correctly account residual stress, Young's modulus and Poisson's ratio of the multi-layer structure membrane, which are important parameters for calculating the buckling height of the membrane (equation (5)). A simplistic approach is used in this work, which assumes the multi-layer membrane is operating as a single-layer membrane with effective mechanical properties. It has been shown in the literature that this approach adds negligible errors to the overall estimation of the membrane deflection [46–49], and analytical calculation results achieved from this approach will be compared to finite element analysis (FEA) results to validate the approach.

1.3.3.1 Membrane structure

The membrane layer structure design is adapted from our previous work [13], which is composed of silicon nitride (Si_3N_4), silicon dioxide (SiO_2), current collector (Cr/Au) and active battery material. The Si_3N_4 and SiO_2 layers are selected as structural layers, while providing initially buckled height when they

are released from the silicon (Si) substrate. Cr layer serving as an adhesion layer between SiO_2 and Au current collector layers. Finally, the active battery material is deposited to form the electrode. The membrane structure is redrawn in Figure 1-6, and naming rule of each layer's residual stress (σ_i), Young's modulus (E_i), Poisson's ratio (v_i), and thickness (d_i) is specified. The thicknesses of the layers are subject to change based on the residual stresses of each layers, which depend on different thin film deposition methods.

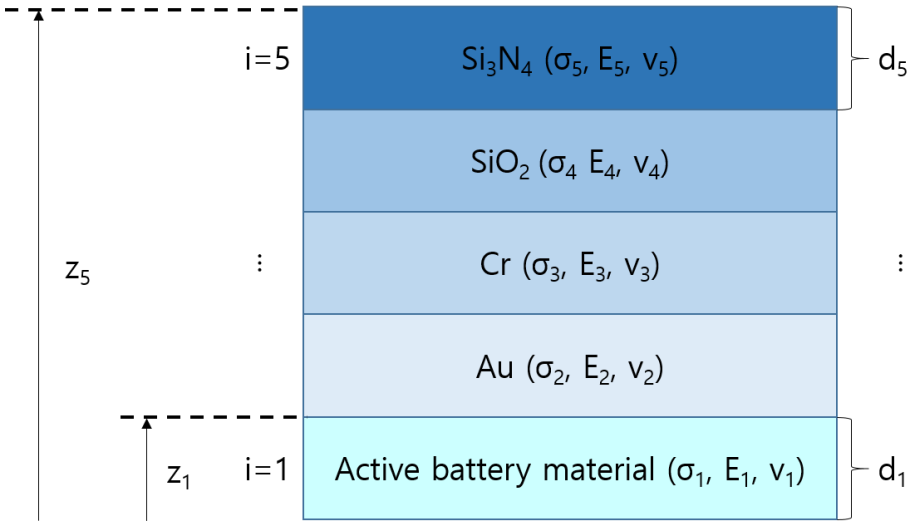

Figure 1-6: Simple schematic representation of the multi-layer membrane (not drawn to scale).

1.3.3.1 Effective residual stress

Stresses in thin films have two primary origins, which are intrinsic and thermal [50]. Intrinsic stress arises during the deposition process such as sputtering, painting, spin coating, vapor deposition, and electrodeposition. The mechanisms that how intrinsic stress is generated are not well characterized quantitatively. It can be induced by grain growth, defect annihilation, phase

transition, and evaporation of solvent [50]. On the other hand, thermal stress is created due to changes in temperature when the film and substrate have different coefficients of thermal expansion. For some cases, thermal stress can be extremely high (*i.e.* several GPa), and it can be a driving force for mechanical failure [50]. In this work, calculation of effective residual stress in multilayer membrane is the main focus.

Effective residual stress (σ_{eff}) of the multi-layer membrane is estimated by the following equation [51]

$$\sigma_{eff} = \left(\frac{\sum_{i=1}^{5} (\sigma_i \times d_i)}{\sum_{i=1}^{5} d_i} \right) \quad (6)$$

Based on the thicknesses of the films and the average stress values, a simple calculation provides the expected net stress. By using equation (6), as long as the film thicknesses can be precisely controlled, the overall stress in the structure can be optimized and accounted for, and a membrane structure with any desired stress state can be created.

1.3.3.1 Effective flexural rigidity

Flexural rigidity (*D*) of a single layer membrane can be defined by the Young's modulus, Poisson's ratio and cube of the membrane's thickness (*h*) as shown in equation (7), which give you a measure of the rigidity of a membrane.

$$D = \left(\frac{Eh^3}{12(1-v^2)}\right) \tag{7}$$

The flexural rigidity needs to be estimated since the buckling height of the membrane is a combination of the residual stress and the flexural rigidity. In this work, effective flexural rigidity needs to be calculated due to the fact that the membrane structure is composed of multiple layers as shown in the previous section (1.3.3.1 Membrane structure). In calculation of the effective flexural rigidity, two different methods are reported in the literature. The first is a "law of mixtures", which gives an average value of the Young's modulus based on a volume fraction of each layers. The second method accounts for the non-homogeneous distribution of different material properties within the structure better than a "law of mixture" treatment [47]. The effective Young's modulus (E_{eff}) of a multi-layer structure of a membrane can be calculated using the "law of mixtures" approach as shown in equation (8)

$$\frac{1}{E_{eff}} = \sum_{1}^{n} \frac{vo_n}{E_n} \tag{8}$$

where E_n and vo_n are the Young's modulus and volume fraction for each layer, respectively. However, the "law of mixtures" approach may not be appropriate

for this work since the method is acceptable for specimens under uniaxial stress. On the other hand, Muralt *et al.* provide a model for clamped multi-layer membranes in piezoelectric micromachined ultrasonic transducers (pMUTs) utilizing a layer-wise formulation of an effective flexural rigidity. The effective flexural rigidity for a n-layer membrane is given by

$$D_{eff} = \frac{1}{3}\sum_{1}^{n} \frac{E_n((z_n - z_s)^3 - (z_n - z_s)^3)}{(1 - v_n^2)} \tag{9}$$

with

$$z_s = \frac{1}{2}\frac{\sum_1^n E_n(z_n^2 - {z_{n-1}}^2)}{\sum_1^n E_n d_n} \tag{10}$$

where z_n is the height from the bottom plane of the membrane and d_n is the thickness of the nth layer. The position of the z_s is the position of the neutral plane. Utilizing equation (7) and (9), buckling height of the multi-layer membrane (equation (5)) can be rewritten as below

$$w_0 = \pm\frac{\sqrt{35}}{4} z_5 \sqrt{\frac{\sigma_{eff}}{-16\left(\frac{1}{R_M^2 z_5}\right) D_{eff}} - 1} \tag{11}$$

1.3.3 In situ characterization methods for Li-ion battery electrodes

In situ, non-invasive characterization techniques are considered to be vital since they enable better understanding of the underlying mechanisms of Li-ion battery operation. *Ex situ* methods inevitably experience exposure to atmosphere during post-mortem analysis and this may affect some bulk and/or surface material properties. *In situ* characterization methods can be divided into two different categories depending on the purpose of the study: characterization of stress and microstructure changes.

1.3.3.1 Stress change

Measurement of stress evolution during battery operation has been a main focus of *in situ* characterization methods since the stress is responsible for cracking and capacity fading of LIB electrodes. Stress in electrodes can occur due to the internal chemical reactions taking place during electrochemical cycling. Also, external mechanical loads acting on the battery pack during manufacturing can cause stress in the electrodes [52]. In this work, the stress which is caused by the electrochemical processes (internal stress) will be discussed.

The stress in the electrodes is primarily induced by changes in lattice dimensions, changes in crystal structures and phase transformations including both crystalline and amorphous phases, which are triggered by the insertion/extraction of lithium ions into/from electrodes. These effects are generally accompanied with volume changes that lead to deformation of the

electrode against the constraining effects of the inactive regions of the electrodes or other parts of the cell (*e.g.* binder or current collector), causing mismatches regions leading to the stress development. The stress generation mechanisms which will be discussed in this work are schematically shown in Figure 1-7 and more detailed review on the causes of the stress development in electrode materials are reported by Mukhopadhyay and Seldon [52].

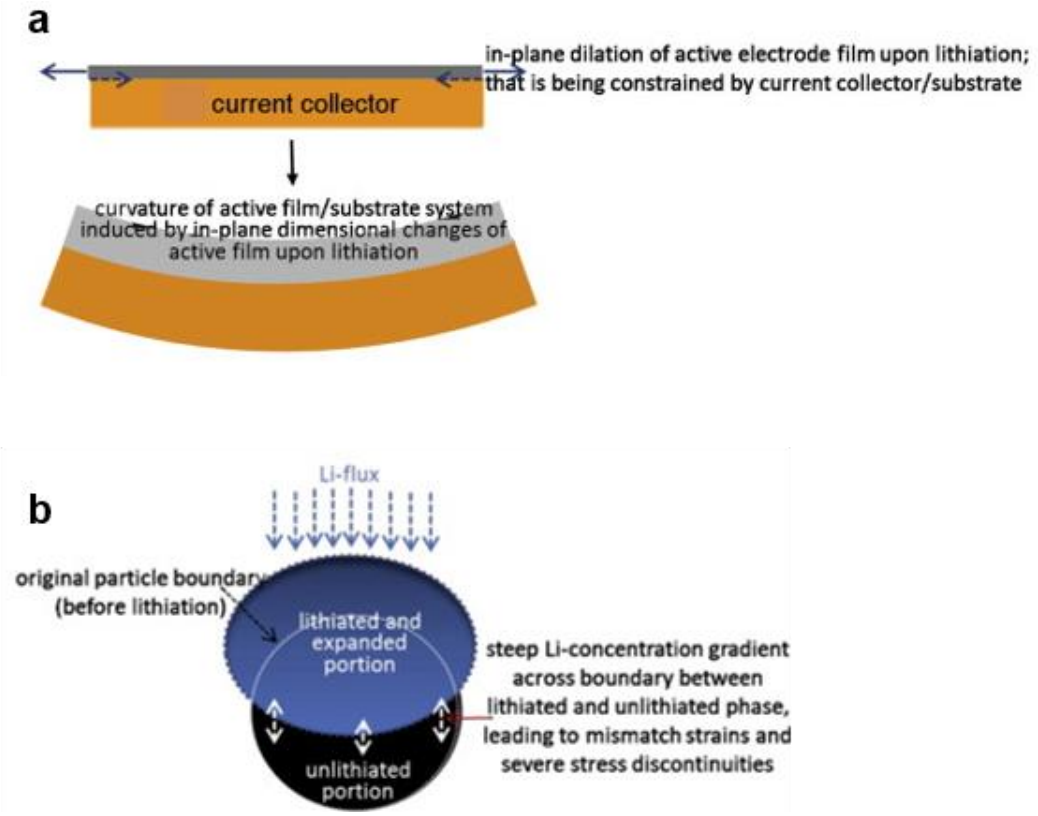

Figure 1-7: Schematic illustrations of (a) constraining of the in-plane dilation of thin film electrodes upon lithiation, by the inactive current collector/substrate and (b) Li-concentration gradient between lithiated and unlithiated portions of a particle, resulting in the development of stress discontinuities. The same is true for adjacent regions possessing different crystal structures/phases [52]. (Reprinted with permission from A. Mukhopadhyay and B.W. Sheldon, *Progress in Materials Science*, 63, 58 (2014). Copyright 2014, Elsevier)

In situ characterization of stress change has been reported using various techniques. Cantilever beam-bending methods [38–41] have been adapted to measure changes in curvature of the substrate for stress calculation in thin film electrodes using the Stoney equation [53,54]. An exemplary case of a cantilever beam-bending experimental setup is shown in Figure 1-8.

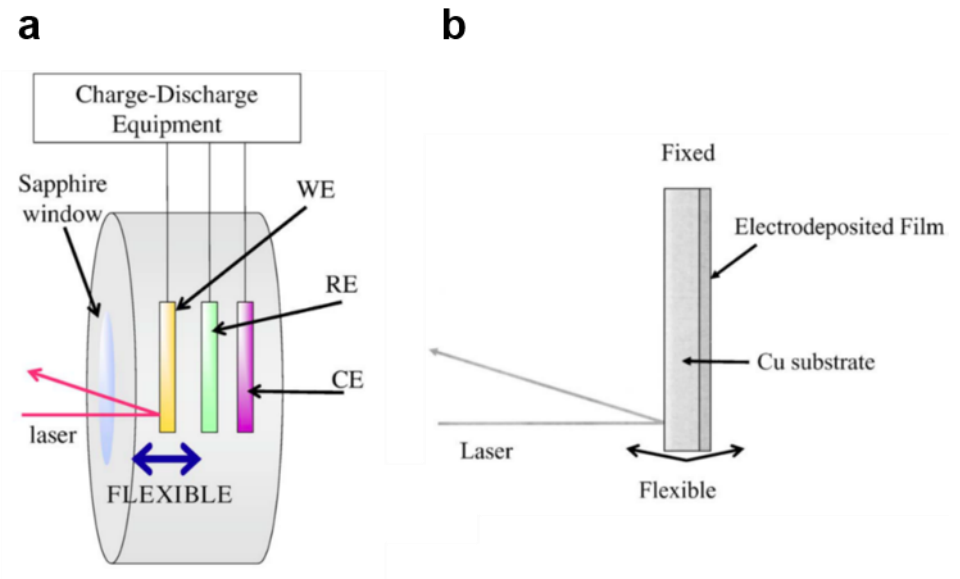

Figure 1-8: Schematic illustration of the experimental setup used for *in situ* stress transition measurement. a) The electrochemical cell and (b) the enlarged view of the cantilever-like working electrode [39]. (Reprinted with permission from H. Mukaibo, T. Momma, Y. Shacham-Diamand, T. Osaka, and M. Kodaira, *Electrochemical and Solid-State Letters*, 10, A70 (2007). Copyright 2007, The Electrochemical Society)

The active materials (pure Sn and Ni-62 atom % Sn alloy thin-film electrodes) are electrodeposited on a Cu cantilever. The deflection of the Cu cantilever induced by the stress generated at the interface between the active material and the substrate are measured using optical method. The alloy electrode exhibits a

better cycle endurance than that of the pure Sn thin-film electrode due to lower stress generated within the electrode.

However, the observations only remain qualitative and do not allow quantification of the desired mechanical properties due to the approximations required to accurately measure stress (*i.e.* uniformity of the film and substrate thickness).

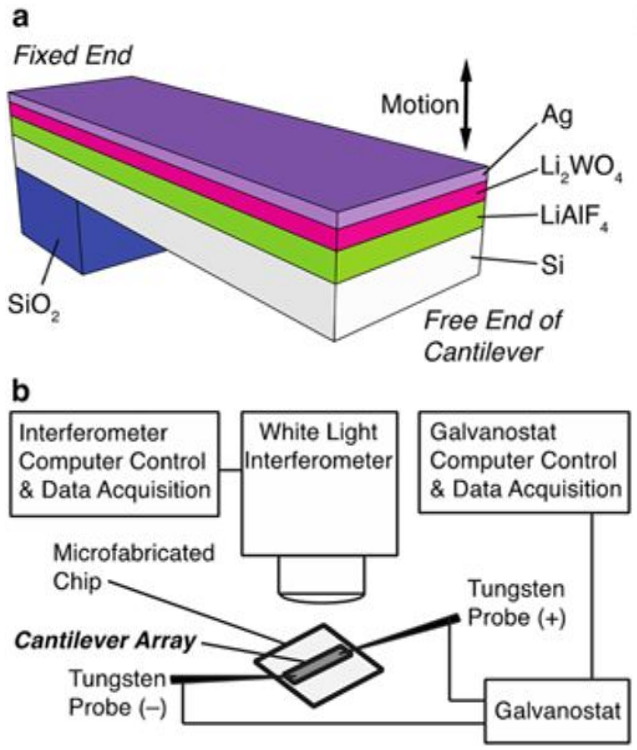

Figure 1-9: Overview of experimental system. (a) Cantilever overview and cross-section. Si cantilevers were fabricated to support a solid-state electrochemical cell on the top surface of the cantilever. Motion of the free end of the cantilever was observed during experiment. (b) Overview of experiment. Cantilever arrays supported on a microfabricated chip were electrically driven by a galvanostat while a white light interferometer was used to observe deflection of the cantilevers [55]. (Reprinted with permission from J.J. Brown, S.-H. Lee, J. Xiao, and Z. Wu, *Physica Status Solidi (a)*, 1, (2016). Copyright 2016, WILEY)

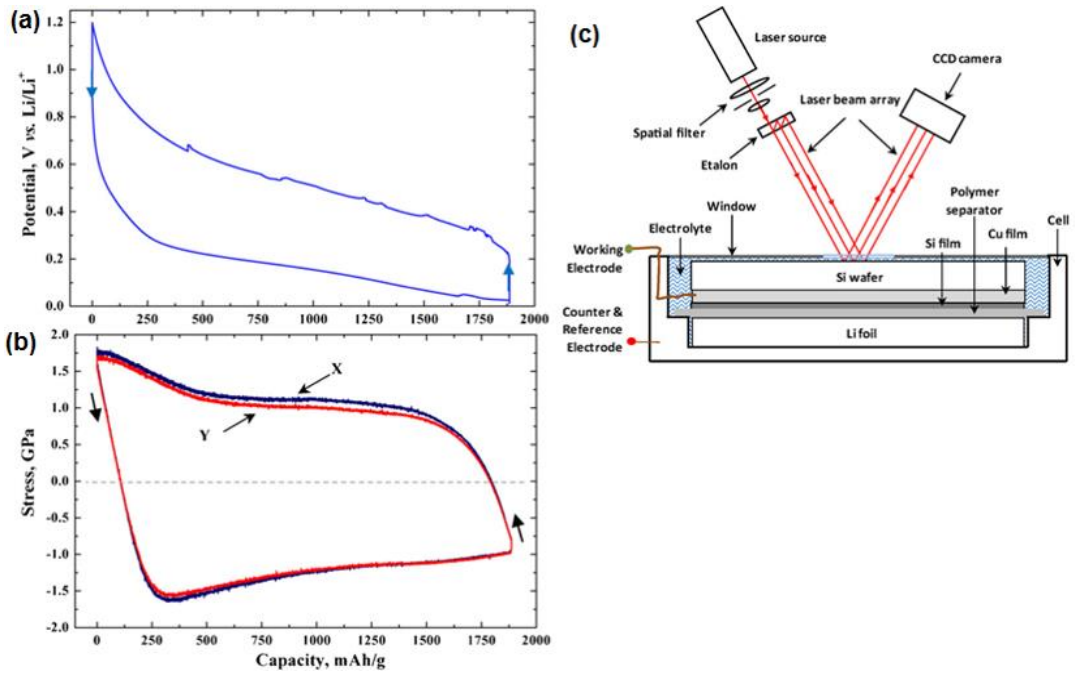

Figure 1-10: (a) Cell potential vs. capacity curve corresponding to lithium insertion and extraction in a Si thin film electrode cycled at a C/4 rate, (b) corresponding stress curve calculated from wafer curvature measurements, (c) schematic illustration of the electrochemical cell assembly and measurement set-up [8]. (Reprinted with permission from V.A. Sethuraman, M.J. Chon, M. Shimshak, V. Srinivasan, and P.R. Guduru, *Journal of Power Sources*, 195, 5062 (2010). Copyright 2010, Elsevier)

Recently, quantitative measurement of mechanical stress during lithium cycling in thin film silicon electrode was reported using cantilever platforms [55,56]. As shown in Figure 1-9, the composite cantilevers consist of suspended single-crystal silicon cantilevers, $LiAlF_4$ electrolyte, Li_2WO_4 lithium reservoir, and Ag electrode layers are utilized, and the deflection of the cantilever associated with stress is monitored by white light interferometry [55]. After charge and discharge cycles, the cantilevers relax upwards which indicate that the material system used in this work experiences time-dependent stress relaxation and continues to restructure itself after both lithiation and delithiation.

Different approaches for quantitative analysis of stresses and strains have also been reported. Digital image correlation has been used to quantify diffusion induced strains in a graphite electrode by tracking lithiation regions with optical microscopy [57]. This is feasible due to color changes in graphite during ion insertion/extraction and cannot be readily applied to any electrode. However, the resolution of the optical microscopy is fundamentally limited due to the diffraction limit of visible light, which is not capable of monitoring microstructural changes. A more general and applicable method using multi-beam optical stress sensor (MOSS) has proven to be an effective method for characterizing Li-ion battery thin film electrodes [5,6,8,14,58–60] (Figure 1-10).

In MOSS technique, the substrate silicon wafer is coated with a silicon dioxide passivation layer, current collector and thin film active battery material of interest. The wafer is packaged in a customized electrochemical cell with an optical window. The electrode is in contact with lithium foil reference/counter electrode and electrolyte. During battery operation, the stress generated in the active battery material during lithium cycling changes curvature of the wafer. The change in the curvature is measured by shining an array of parallel laser beams on the wafer, and the stress is quantified by applying Stoney equation. This method enabled achieving important mechanical parameters such as average stress, biaxial modulus and fracture energy for both silicon thin film and commercial electrodes. While the technique is proven to be beneficial for mechanical characterization, inability to access the electrode limited its

combination with other techniques. The parallel laser beams need to shine the bare silicon wafer surface through the optical window while the electrode surface needs to be facing opposite side of the optical window. This limitation restricted its potential integration with other methods for providing structural information on the electrodes.

1.3.3.2 Microstructural change

It is important to investigate the reaction kinetics and microstructural changes during battery operation in order to improve battery design and gain fundamental knowledge of physical mechanisms. A significant amount of research has been devoted to developing various *in situ* methods for battery studies. These techniques include optical microscopy, scanning electron microscopy (SEM), transmission electron microscopy (TEM), X-ray diffraction (XRD), nuclear magnetic resonance (NMR) spectroscopy, and Raman spectroscopy [7].

Optical microscopy has been also utilized for monitoring microstructural changes in various LIB electrodes. Electrochemically induced macroscopic structural changes of electrodes and dendritic lithium formation can be investigated through (digital) optical microscopy [61–69]. Beaulieu and colleagues used *in situ* AFM optical microscopy to study the colossal volume changes and morphology of Si-Sn sputtered thin films during lithium cycling [70]. When lithium is inserted to alloy films on rigid substrates, the films expand perpendicular to the substrate. When lithium is extracted, the films contract both

perpendicular and parallel to the substrate, generating crack patterns similar to those found in dried mud (Figure 1-11). The *in situ* microscopy enabled characterization of the onset and evolution of dendrites as well [71]. However, due to poor resolution of the optical method, different techniques such as AFM and SEM have to be used in parallel in order to achieve more quantitative and conclusive experimental results.

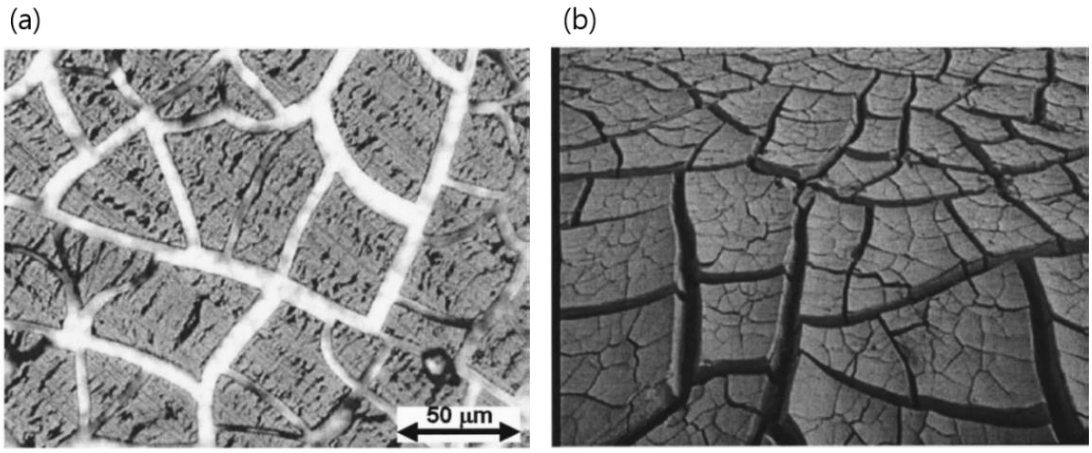

Figure 1-11: The resemblance of an optical micrograph of a Li-alloy film after expansion and contraction (a) to cracked mud in a dry lake bed (b) [70]. (Reprinted with permission from L.Y. Beaulieu, K.W. Eberman, R.L. Turner, L.J. Krause, and J.R. Dahn, *Electrochemical and Solid-State Letters*, 4, A137 (2001). Copyright 2001, The Electrochemical Society)

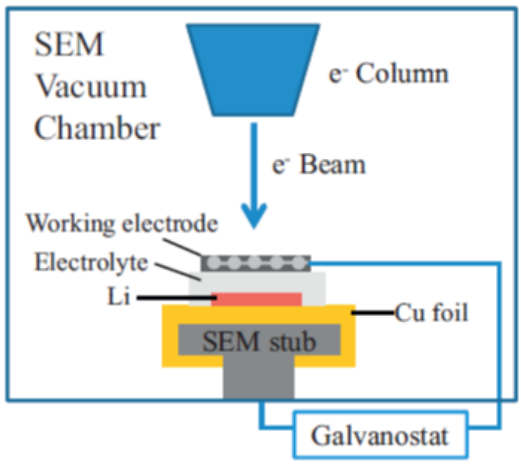

Figure 1-12: Setup of the lithium-ion cell for the *in situ* experiment in the SEM. Using a mesh as current collector allows permeation of electrolyte and the imaging of the electrode [72]. (Reprinted with permission from D. Chen, S. Indris, M. Schulz, B. Gamer, and R. Mönig, *Journal of Power Sources*, 196, 6382 (2011). Copyright 2011, Elsevier)

In situ SEM/TEM has been introduced for its unique capability of resolving the microstructural evolution of LIB electrodes with high spatial and temporal resolution. The *in situ* SEM method allows for the observation of microscopic mechanisms up to 1 nm resolution depending on the SEM equipment [72–79] (Figure 1-12). As a result, the experimental platform can be utilized for investigating chemical reaction pathways, monitoring phase changes in electrodes or studying degradation effects in batteries.

In situ TEM has its unique capability of offering a direct study of the structural evolution of individual nanowire or nanoparticle electrodes with near-atomic resolution in real time [9,80–82]. However, both methods have limitations of using volatile organic electrolytes due to the high pressure inside the vacuum chamber of the SEM/TEM. In order to overcome this limitation, an

"open-cell" concept is introduced by creating the first working nanobattery in the TEM [9,80] (Figure 1-13). It utilizes an individual SnO_2 nanowire anode, an ionic liquid electrolyte (ILE) and a bulk $LiCoO_2$ cathode. The microstructural evolution of the SnO_2 anode was observed during battery operation.

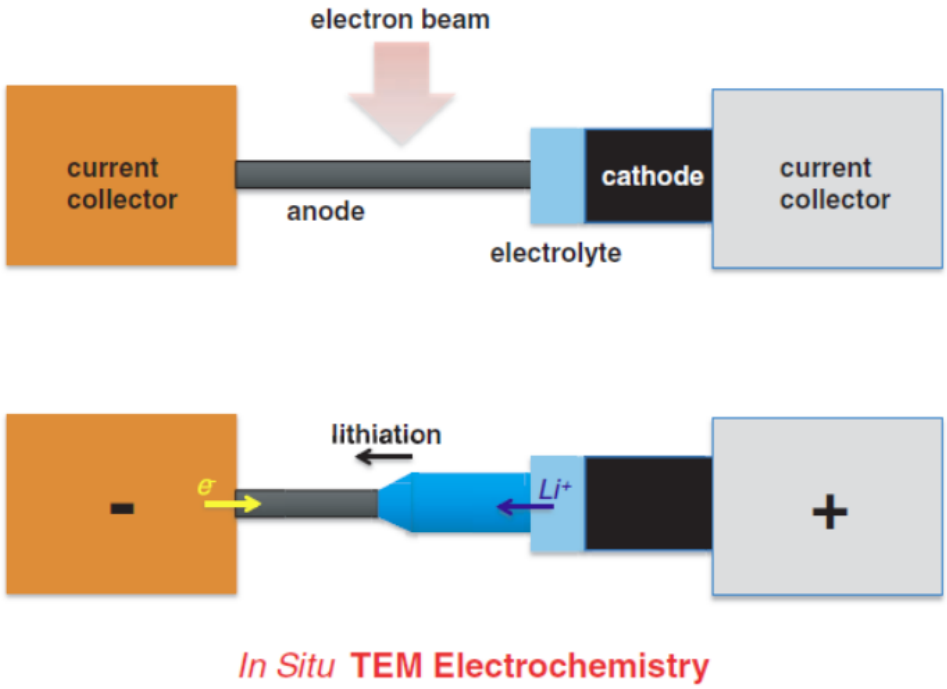

Figure 1-13: Schematic illustration of *in situ* TEM electrochemical tests setup. Top: A nanobattery setup for anode study. The key components include an electron-transparent anode (such as a nanowire or nanoparticle), a vacuum-compatible electrolyte (such as ionic liquid, polymer or solid-state electrolyte), a stable Li source (such as a bulk discharged cathode) and the current collectors. Bottom: Operation of the nanobattery for lithiation of the anode. Potential is applied to the current collectors to drive the electrons and Li ions flow across the circuit, and the microstructural evolution is monitored in real time [9]. (Reprinted with permission from X.H. Liu, Y. Liu, A. Kushima, S. Zhang, T. Zhu, J. Li, and J.Y. Huang, *Advanced Energy Materials*, 2, 722 (2012). Copyright 2012, WILEY)

Crystallographic changes which occur inside the battery electrode as it is lithiated and delithiated have been investigated using *in situ* XRD [10,83–115]. Obrovac and Christensen confirmed an amorphization of crystalline silicon during battery operation and showed that highly lithiated amorphous silicon crystallizes to a new $Li_{15}Si_4$ phase below 50 mV [84]. Hatchard and Dahn gathered *in situ* XRD data on a sputtered amorphous silicon film during lithiation and showed the formation of the $Li_{15}Si_4$ phase below 30 mV [85]. Li and Dahn investigated crystalline silicon composite electrodes and were able to draw a phase diagram based on the electrochemical and XRD data. This showed the phase changes and regions of phase stability during the lithiation and delithiation of the silicon electrode [86]. High-energy x-ray diffraction (HEXRD) has been also utilized to study the structural evolution of the electrodes. Liu *et al.* used the HEXRD to show that V_2O_5 undergoes phase transformations during the first Li+ ion intercalation (*i.e.* discharge) process [83]. He *et al.* utilized an *in situ* high energy synchrotron XRD to identify the dynamic structural change of graphite during battery operation using 1/3 C-rate. Monitoring of the detailed structure evolution of the graphite was achieved due to the fast data collecting detector and high energy X-ray beam of the characterization method (Figure 1-14).

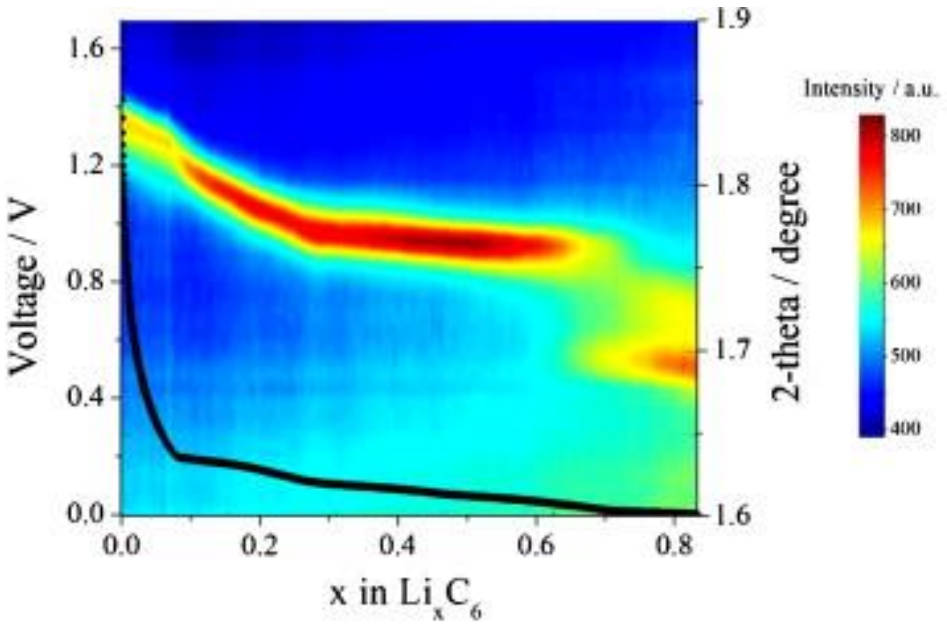

Figure 1-14: Contour plot of XRD patterns and discharge curve over the Li/graphite cell discharged from 1.53 to 0.001 V at 1/3 C [94]. (Reprinted with permission from H. He, C. Huang, C.-W. Luo, J.-J. Liu, and Z.-S. Chao, *Electrochimica Acta*, 92, 148 (2013). Copyright 2013, Elsevier)

While long-range structural information is typically available from the diffraction methods, nuclear magnetic resonance spectroscopy (NMR) is an extremely useful technique for characterizing local structure of Li-ion battery electrodes, even when the system is highly disordered [116–126]. A range of *in situ* and *ex situ* studies have been reported to investigate the Li-Si system using NMR [127–129]. These studies show the crystalline silicon is converted into an amorphous Li_xSi phases during the first lithiation, which transforms into a metastable crystalline phase and possibly over-lithiated phases [130]. Recently, Ogata and colleagues performed *in situ* NMR studies, which enable studying detailed kinetics of the electrochemical lithiation and delithiation reactions in nm-sized silicon based anodes over multiple cycles [130] (Figure 1-15).

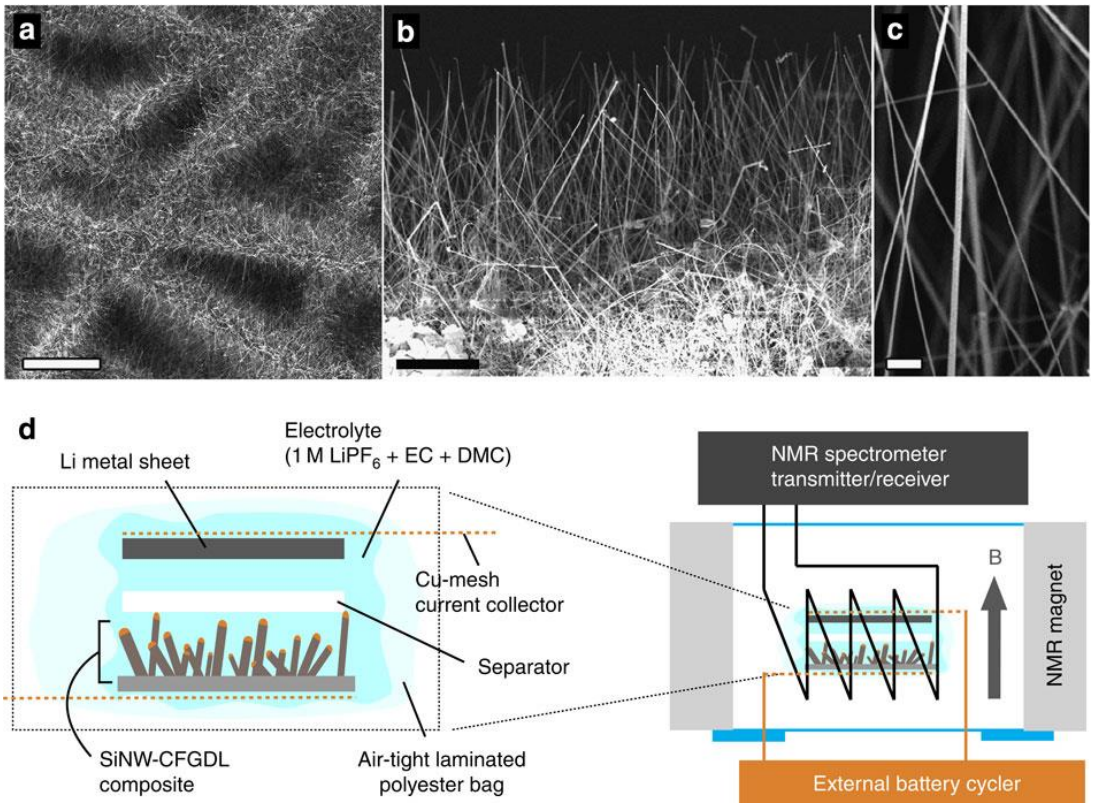

Figure 1-15: SEM images of as-grown SiNWs on fibre-based gas diffusion layer (CFGDL) (a) Planar view, (b) cross sectional view and (c) a magnified image of (b). The scale bars for (a–c) are 50, 15 and 500 nm, respectively. (d) Schematics of the SiNW-composite based cell and the set-up for the *in situ* 7Li NMR measurements. The cell design comprises Si nanowires (SiNW), a carbon fibre based gas diffusion layer support (CFGDL), electrolyte (1M $LiPF_6$ in ethylene carbonate (EC) and dimethyl carbonate (DMC) solution), a porous glass fibre mat and a Cu mesh sealed in a polyester bag [130]. (Reprinted with permission from K. Ogata, E. Salager, C.J. Kerr, A.E. Fraser, C. Ducati, A.J. Morris, S. Hofmann, and C.P. Grey, *Nature Communications*, 5, 3217 (2014). Copyright 2014, Macmillan)

Compared to the aforementioned techniques which rely on bulky external equipment for the measurement and complex electrochemical cells, Raman spectroscopy is a valuable and sensitive tool for probing structural and chemical variations of Li-ion electrodes in a relatively simple fashion [3,131–145] (Figure 1-16).

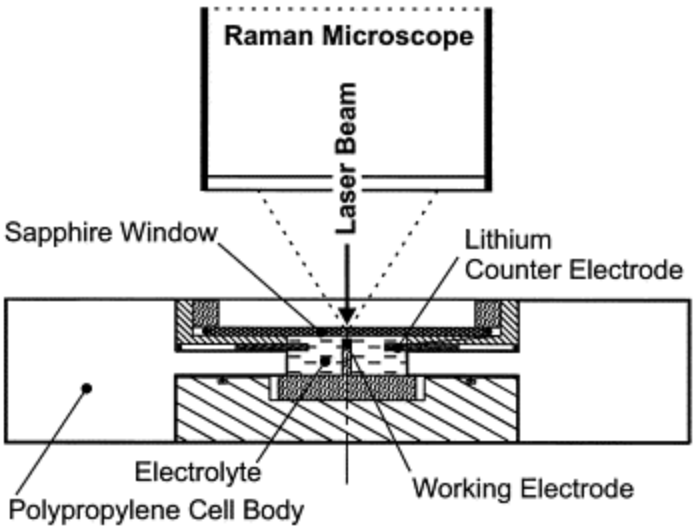

Figure 1-16: The electrochemical cell for in situ Raman microscopy [146]. (Reprinted with permission from P. Novák, J.-C. Panitz, F. Joho, M. Lanz, R. Imhof, and M. Coluccia, *Journal of Power Sources*, 90, 52 (2000). Copyright 2010, Elsevier)

Raman spectroscopy is a spectroscopic method based on inelastic scattering of monochromatic light, generally a laser source is used. Inelastic scattering of a monochromatic light occurs when the frequency of photons in the monochromatic light changes upon interaction with a sample. Photons of the laser light are absorbed by the sample and then reemitted. The frequency of the reemitted photons is shifted up or down in comparison with original monochromatic frequency, which is called the Raman effect [147].

The Raman effect is based on molecular deformation in electric field (E), which is determined by molecular polarizability (α) of the sample. The laser beam can be considered as an oscillating electromagnetic wave with the electric field. When the laser interacts with the sample, it induces electric dipole moment $P = \alpha E$, causing the molecular deformation. Due to the molecule's periodical

deformation, it starts vibrating with characteristic frequency (ν_{vib}). When the monochromatic laser light with frequency (ν_0) excites the molecules, it transforms the molecule into oscillating dipoles. Such oscillating dipoles emit light of three different frequencies as shown in Figure 1-17.

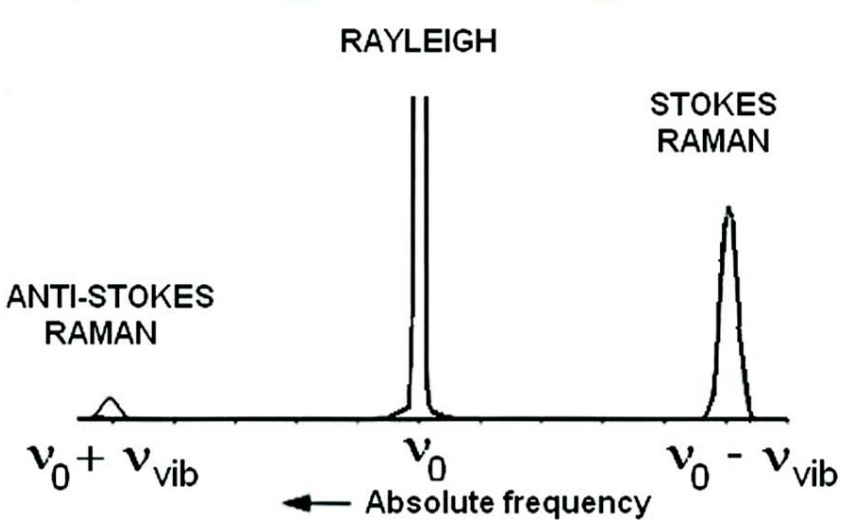

Figure 1-17: Raman and Rayleigh scattering of excitation at a frequency ν_0. The molecular vibration in the sample is of a frequency ν_{vib} [3]. (Reprinted with permission from R. Baddour-Hadjean, and J.-P. Pereira-Ramos, "Raman Microspectrometry Applied to the Study of Electrode Materials for Lithium Batteries," *Chemical Reviews*, 110, 1278 (2010). Copyright 2010, American Chemical Society)

The molecules can absorb the photon with the frequency ν_0 and become excited. When the molecule returns back to the same basic vibrational state, it emits light with the same frequency ν_0 as the excitation source. This type if interaction is called an elastic Rayleigh scattering. When the photon with frequency ν_0 is absorbed by the molecule, which is in the basic vibrational state, part of the photon's energy can be transferred to the molecule with frequency ν_{vib}. As a result, frequency of the scattered light is reduced to $\nu_0 - \nu_{vib}$. This Raman

frequency is called Stokes frequency. When the photon with frequency v_0 is absorbed by the molecule, which is already in the excited vibrational state, excessive energy of excited state can be transferred to the photon as it returns to the basic vibrational state. The resulting frequency of scattered light goes up $v_0 + v_{vib}$. This Raman frequency is called Anti-Stokes frequency [3].

A plot of the intensity of Raman scattered radiation as a function of its frequency difference from the incident radiation is called a Raman spectrum Figure 1-17, and this difference is called the Raman shift [3]. Due to the fact that the basic vibration state population is greater than that of the excited vibration state, the Stokes has higher intensity than the Anti-Stokes line. Therefore, Raman spectrum is generally plotted as a function of intensity versus the Stokes-shifted frequencies in wavenumbers (cm^{-1}). The Raman spectrum provides unique information of the sample. This is due to the fact that the frequency shifts between the incident radiation and the Raman-scattered radiation correspond to the vibrational energy levels of the molecule or the crystal.

Information that can be obtained using this technique involves local disorder, changes in bond length, bond angles, coordination and Li dynamics, all correlating capacity loss mechanisms to surface composition [3,148]. Using this method, both anode and cathode materials such as graphite, Si-C composites, V_2O_5 and lithium containing metal oxides have been studied, providing information both about the peaks (absence, presence, splitting, shift) as well as the spatial distribution [3]. The value of Raman spectroscopy in battery research

is further illustrated by its integration in commercially available tools that combine Raman with atomic force microscopes.

The major limitation of the work describe above lies in achieving quantitative data on the stress or mechanical property changes in electrodes, which prevents acquiring insights on how the microstructural changes lead to stress changes in the electrodes. As in the case of silicon, composition changes and phase transformations during the lithiation process change the lattice configuration, causing strains that in turn result in loss of mechanical integrity and device failure. Continuous battery cycling affects the electrode/electrolyte interface and also contributes to progressive capacity loss and coulombic efficiency deterioration. Notwithstanding individual advantages and valuable insights provided by the aforementioned real-time monitoring techniques, interpretation of the obtained data is often limited by the difficulty in decoupling these interrelated phenomena. The next generation energy storage electrode research requires the use of multi-modal experimental platforms, capable of providing mechanical, compositional, chemical and structural information for the electrodes under investigation. Such platforms can complement theoretical and computational studies and further assist in the optimization of both electrode structure and device operating parameters.

1.3.3.3 Summary of *in situ* characterization methods for Li-ion battery research

Table 1 summarizes the state-of-the-art *in situ* characterization methods for LIB research under different techniques.

Table 1: Summary of the *in situ* methods for LIB research

***In situ* methods**	**Investigated electrodes**
Stress/strain	
MEMS	$LiMn_2O_4$ [38], Sn alloy [39], $Ni(OH)_2$/NiOOH [40], Si [13,14,41,55,56]
Optical microscopy	C [57]
Multi-beam optical stress sensor	Si [5,6,8,58,60], Graphite-based electrodes [59]
Microstructural	
Optical microscopy	C [61,62,64], Li [63,65,67–69,71], Si [66,70], Sn [70]
SEM	SnO_2 [72], $LiMn_2O_4$ [73], $Li(Ni_{0.8}Co_{0.15}Al_{0.06})O_2$ [74], Si [75–77], Li [78,79]
TEM	SnO_2 [80,82], $LiCoO_2$ [81], Si [82]
XRD	Sn [10], V_2O_5 [83], Si [84–87,89], $Ag_2VO_2PO_4$ [88], $LiNi_{0.5}Mn_{1.5}O_4$ [90,112], Ge [91], TiO2 [92], $Li[Li_{0.2}Ni_{0.2}Mn_{0.6}]O_2$ [93], C [94], $LiMn_2O_4$ [95], $LiFePO_4$ [96,100,104], CuF_2 [97], $Ag_2VP_2O_8$ [99], Li_2FeSiO_4 [101], $Li_{1.2}Co_{0.1}Mn_{0.55}Ni_{0.15}O_2$ [102], $K_{0.25}Mn_2O_4$ [103], $LiNi_{0.8}Co_{0.2}O_2$ [105], $0.5LiNi_{0.292}Co_{0.375}Mn_{0.333}O_2$ [106], $Li_{1.23}Ni_{0.09}Co_{0.12}Mn_{0.56}O_2$ [107], TiO_2 [108], $LiNi_{1/2}Mn_{3/2}O_4$ [109], $LiCoPO_4$ [110], Li_2RuO_3[111], Li_2FeSiO_4/C [113], $Li_xMn_{1.5}Ni_{0.5}O_4$ [114,115]
NMR	Si [129,130], Li [122,123,127], $Li_{1.08}Mn_{1.92}O_4$ [119,120], $LiCoO_2$ [121], Cu_3P [124], C [125], Liquid electrolyte [117,118]
Raman spectroscopy	V_2O_5 [131,133], $LiFePO_4$ [132], $LiCoO_2$ [134], Au/SiO_2 [135], C [136,139–142,145], Li_2MnO_3 [137], Si [138], SEI on Li [143],

1.4 Structure of dissertation

Chapter 1 has presented the motivation for this research and the relevant work found in literature. Chapter 2 discusses the MEMS Fabry-Perot sensor design, fabrication, and integration with Raman microscope for *in situ* characterization of qualitative stress and microstructural changes in LIB

electrodes. Chapter 3 proposes a unique approach of modifying stress and stress gradient in V_2O_5 cathode electrode and discusses crystal phase-dependent stress changes in the V_2O_5 cathode investigated using the Fabry-Perot MEMS sensor integrated with an optical measurement setup. Chapter 4 studies on the design and fabrication of the buckled membrane MEMS sensor. Chapter 5 is focused on the integration of the buckled membrane MEMS sensor with AFM-Raman spectroscopic setup for *in situ* characterization of quantitative stress and microstructural changes in LIB electrodes. Chapter 6 summarizes the contributions of this dissertation and discusses the future direction of this study.

Chapter 2: *In situ* study of V_2O_5 electrode using Fabry-Perot MEMS sensor platform

This chapter discusses the principle of operation and experimental results of a Fabry-Perot MEMS sensor platform. The discussion also presents the development of the multi-modal sensing platform that is capable of *in situ* characterization of qualitative stress and microstructural changes in a V_2O_5 cathode in a single experimental setup.

Mr. Sergio Baron contributed to developing the Fabry-Perot MEMS sensor, integrating with an optical measurement setup, and coin cell packaging. Dr. Ekaterina Pomerantseva contributed to assembling coin cells and running electrochemical experiments. Dr. Markus Gnerlich contributed to developing MATLAB code for analyzing experimental results. Dr. Konstantinos Gerasopoulos and Dr. Albert A. Talin contributed to developing the Fabry-Perot MEMS sensor platform. Dr. Karen Gaskell contributed to utilizing and scheduling the Raman microscope for experiments.

2.1 Fabry-Perot MEMS sensor

2.1.1 Sensor design and fabrication

Figure 2-1(a) shows the Fabry-Perot MEMS sensor, composed of an array of mechanically flexible circular membranes. The membranes separate the sensor into two cavities, referred to as the ‘optical’ and ‘battery’ cavities. The optical cavity is created by anodically bonding glass and silicon wafers. The deeper battery cavity is formed on the other side of the membrane, enabling the

deposition of an insulating layer, current collector and active battery material, as well as providing a channel for the liquid electrolyte. We selected thin film V_2O_5 as the active battery material to demonstrate the capability of the platform. The detailed fabrication procedure is described in our previous work [13] (see Figure 2-2 for simplified fabrication process).

Figure 2-1(b) illustrates the cross-section of a single membrane with 150 μm diameter, formed by the 700 nm thick Si_3N_4 and 200 nm thick SiO_2 layers inside the 12 μm deep optical cavity. Inside the 288 μm deep battery cavity, a 50 nm thick SiO_2 is used as a barrier coating to prevent lithium intercalation into the silicon wafer, followed by thin layers of Cr/Au as the current collector. Finally, a 137 nm thick V_2O_5 thin film electrode (0.81 Å/cycle) is conformally coated as an active battery material by atomic layer deposition (ALD). The cross-section scanning electron microscope (SEM) image of the fabricated sensor is shown in Figure 2-3(a).

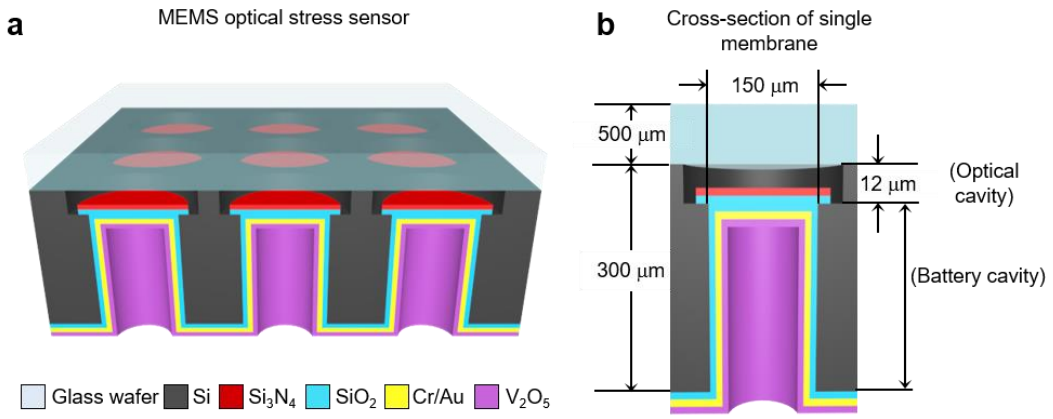

Figure 2-1: (a) 3D schematic of Fabry-Perot MEMS sensor. (b) Cross-section diagrams of a single membrane (not drawn to scale).

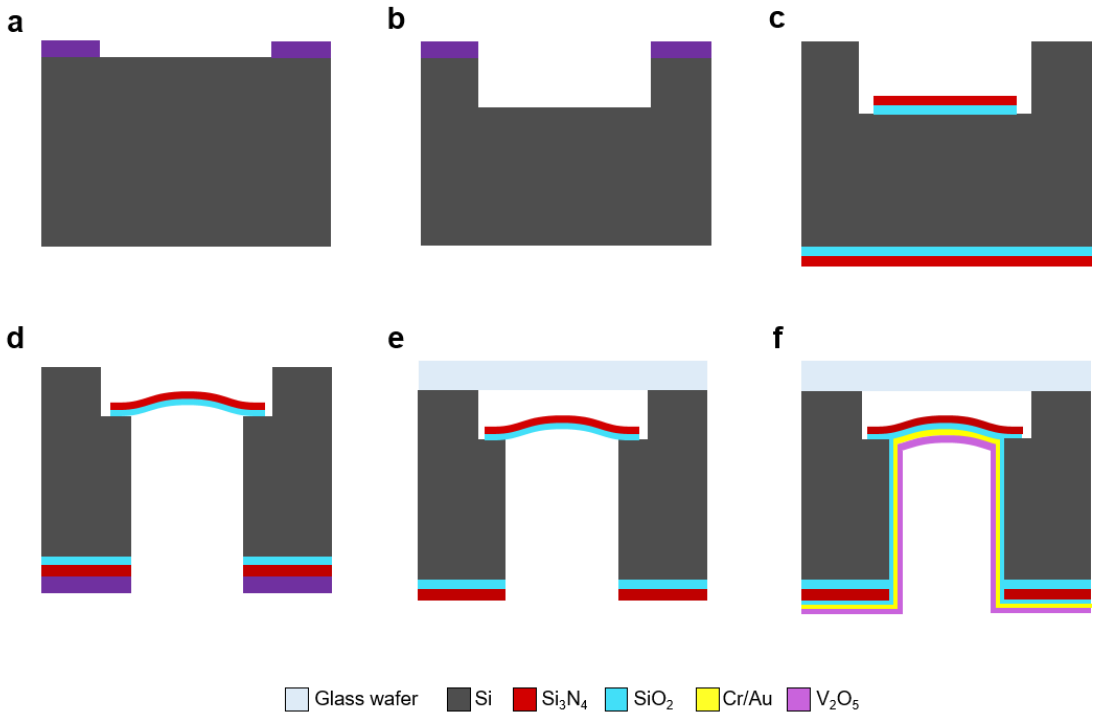

Figure 2-2: (a) Photoresist etch mask for optical cavity. (b) Deep reactive ion etching. (c) Thermally grown SiO_2 and low pressure chemical vapor deposition of Si_3N_4 after reactive ion etching. (d) Released Si_3N_4 and SiO_2 membrane using deep reactive ion etching, while the SiO_2 serves as the etch stop layer. (e) Anodic bonding of glass wafer to Si substrate. (f) Deposition of SiO_2 passivation layer, Cr/Au current collector layer, and ALD-deposited V_2O_5.

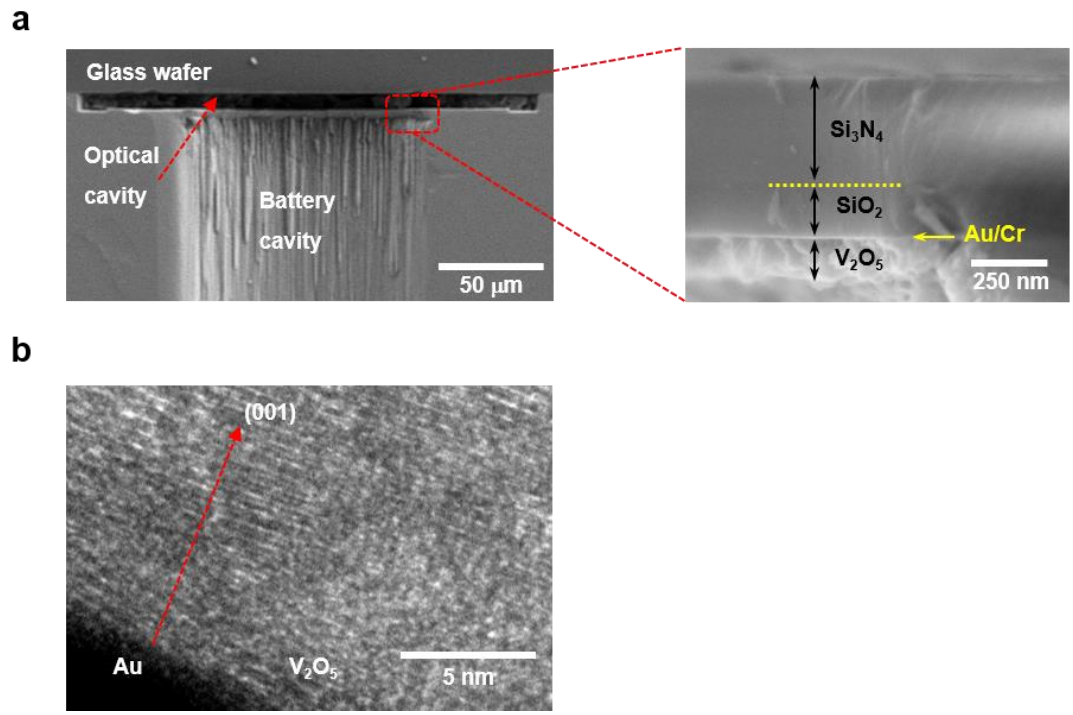

Figure 2-3: (a) Left panel: Cross-section SEM image of the membrane in the Fabry-Perot MEMS sensor. Right panel: Enlarged view of the membrane, showing multi-layer structure. (b) TEM image of a V_2O_5 layer grown on top of Au layer.

It has been reported previously that the V_2O_5 film shows preferential growth along (001) direction on an Au-coated stainless steel [149]. This preferential growth on the Au-coated membrane is confirmed using transmission electron microscopy (TEM) (Figure 2-3(b)) and by X-ray diffraction (XRD) (Figure 2-4).

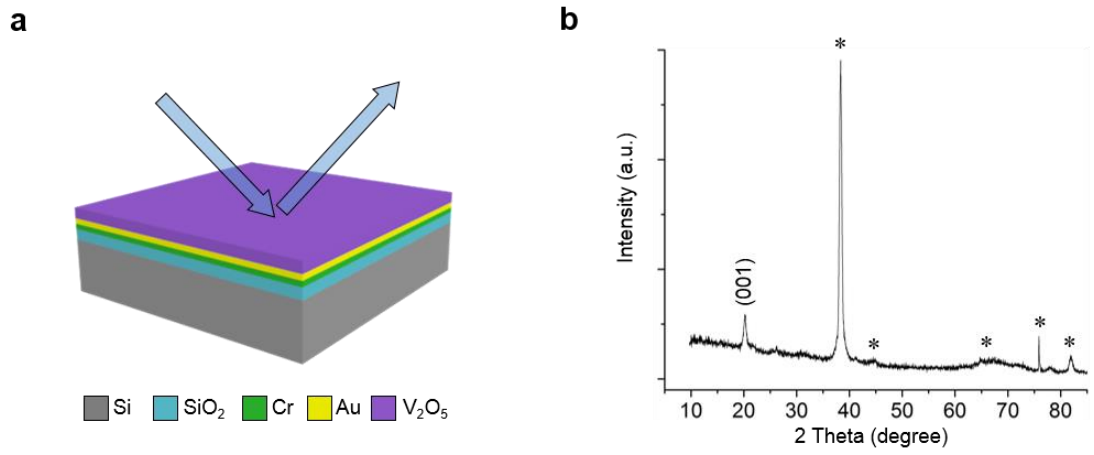

Figure 2-4: (a) Schematic showing material stack of XRD measurement sample: (from bottom to top) Diced silicon wafer, SiO_2, Cr, Au, and ALD-deposited V_2O_5. (b) Measured XRD spectrum showing the V_2O_5 (001) peak as well as peaks from the Au layer and Si substrate (marked with stars).

The optical cavity of the sensor is utilized for monitoring the membrane deflection due to the stress change in the electrode using optical interferometry. At the same time, the optical cavity allows μRaman spectroscopy to probe the V_2O_5 thin film electrode layer through the transparent glass wafer and the multi-layer membrane, which is sufficiently thin to be semi-transparent. Thus, this unique design of the sensor addresses the challenge of *in situ* characterization of both the stress and structural changes during battery operation.

2.1.2 Sensor characterization

Correlation between the stress in the electrode, membrane deflection, and fringe radius change are analyzed using COMSOL simulation and analytical calculation. First, correlation between the stress change in the electrode and membrane deflection is simulated using COMSOL. A clamped circular membrane with three different layers (Si_3N_4, SiO_2, and V_2O_5) is used for the simulation. Detailed information about parameters that are used for the simulation can be found in Table 2. The stress-induced membrane deflection is simulated in the V_2O_5 electrode and the results are shown in Figure 2-5(a),(b). When the stress in the V_2O_5 electrode is varied from −1 to 1 GPa, the membrane deflection changed from 1.08 to 0.78 μm. These results show that the membrane deflection becomes larger when the stress in the V_2O_5 is more compressive. The COMSOL simulation results are compared to the analytical calculation results computed using MATLAB.

The same parameters used in the COMSOL simulation are utilized for the analytical calculation and the membrane deflection is numerically computed depending on the stress change in the electrode. When the stress in the V_2O_5 electrode is varied from −1 to 1 GPa, the membrane deflection changed from 1.16 to 0.84 μm, respectively (Figure 2-5(c)). The analytical calculation results correspond well with the COMSOL simulation results, indicating the membrane deflection indeed becomes larger when the stress in the electrode is more compressive.

Table 2: Parameters used for COMSOL models

Materials	Thickness (nm)	Young's modulus (GPa)	Poisson's ratio	Residual stress (GPa)	Radius (μm)	Pressure (MPa)
Si_3N_4	700	290	0.27	1	75	0.5
SiO_2	300	59	0.17	−0.25		
V_2O_5	120	129.2	0.25	−1 to 1		

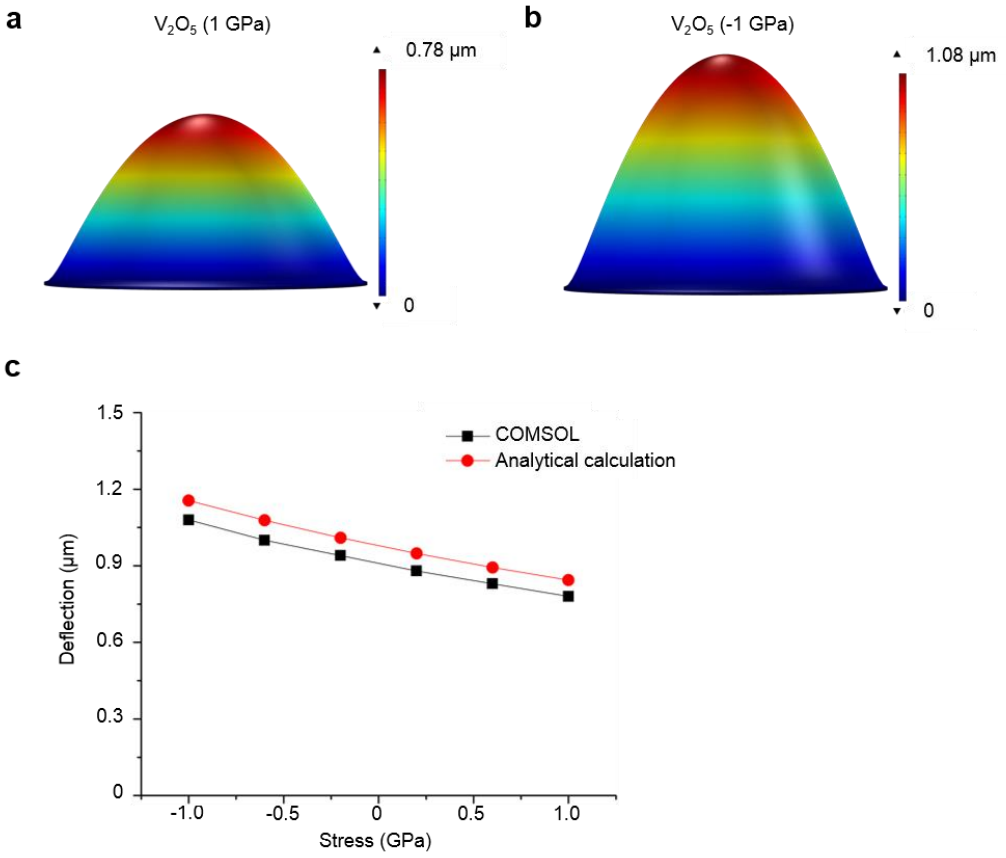

Figure 2-5: (a,b) Total deflection of the clamped circular membrane with stresses in the V_2O_5 film at +1 GPa and −1 GPa, respectively. (c) Total deflection of the clamped circular membrane achieved from the COMSOL simulation (in black) and analytical calculation (in red) as a function of the V_2O_5 stress.

After verifying how the membrane deflects according to the stress change in the electrode, the fringe radius change is analyzed depending on different membrane deflections. When the light source illuminates the optical cavity, incident light is reflected and the intensity of the reflected light varies depending on the shape of the membrane. The shape of the membrane can be described as below [150]:

$$w(r) = w_0 \left(1 - \frac{r^2}{R^2}\right)^2 \tag{12}$$

where w is the local membrane deflection along the radial membrane coordinate r. Using Fabry-Perot interferometry principle, the reflected light intensity change due to membrane deflection can be written as below:

$$I_r = \frac{F \sin^2\left(\frac{\delta}{2}\right)}{1 + F \sin^2\left(\frac{\delta}{2}\right)} I_i \tag{13}$$

$$\delta = \frac{4\,\pi\,n\,d}{\lambda} \cos(\theta) \tag{14}$$

where I_r is the reflected light intensity, I_i is the incident light intensity, and F is the finesse of the optical cavity. δ is phase difference between each successive reflection described in equation (14), where n is the refractive index, d is the optical cavity depth, λ is the wavelength of the light source, and θ is the angle of the incident light source. By replacing the optical cavity depth d with the local membrane deflection as described in equation (12), the reflected light intensity I_r can be rewritten as a function of the membrane diameter (r). Using equation (12), two different membrane shapes are drawn using MATLAB (Figure 2-6(a)). Based on different membrane shapes, the reflected light intensity profiles are simulated using equations (13) and (14) (Figure 2-6(b)). The results confirm that the membrane deflection becomes larger when the fringe radius becomes bigger (Figure 2-6(c)). Therefore, it is verified that more compressive (tensile) stress induces more positive (negative) fringe radius change.

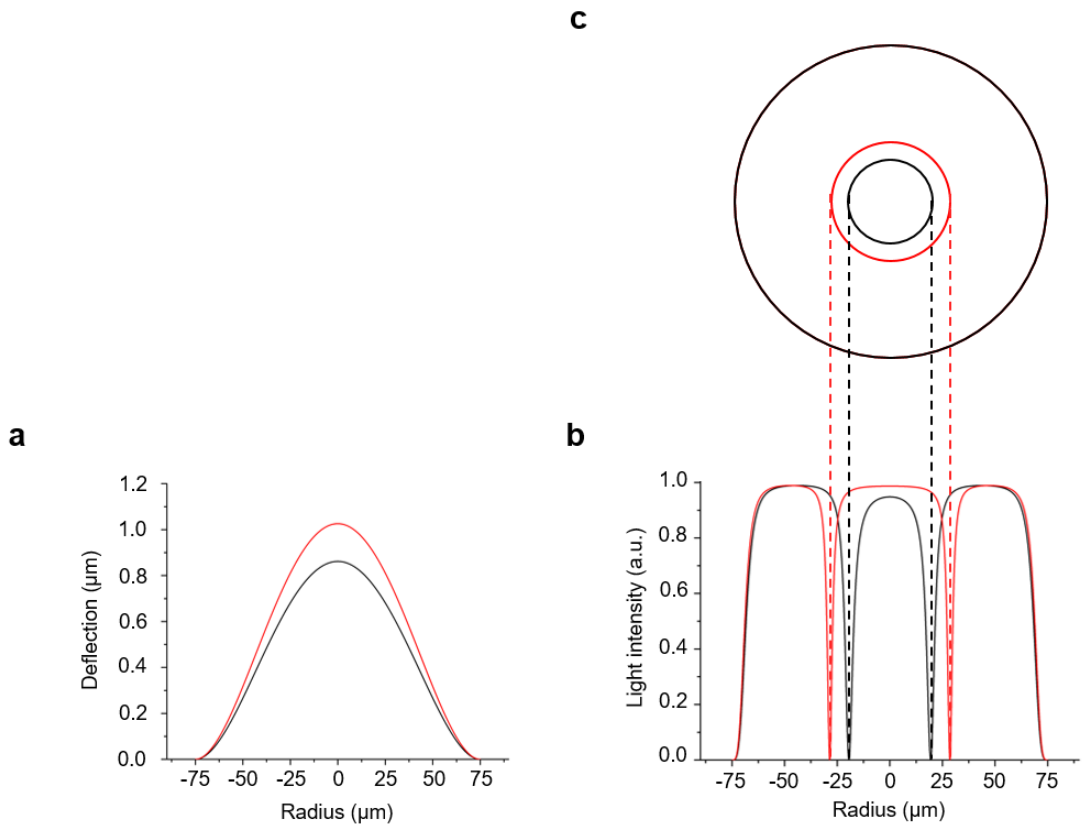

Figure 2-6: (a) Color-coded graphs showing two different membrane shapes as a function of the membrane radius. Red and black lines correspond to membrane deflection of 0.86 and 1.03 μm, respectively. (b) 2-D reflected light intensity graph along the center of the membrane. (c) Reconstructed interference patterns based on the 2-D reflected light intensity.

2.2 Experimental setup and integration

A modified coin cell with an optical window is devised to facilitate the experiment during battery operation (Figure 2-7(a)). In the coin cell, the Fabry-Perot MEMS sensor is placed with other coin cell parts and assembled together to build a half-cell configuration. The hermetic sealing of the coin cell is achieved using the aluminium foil tape with conductive adhesive to interface the sensor to the conductive top coin cell manifold for proper battery operation (See Methods). The assembled coin cell is connected to the potentiostat and placed

under the Raman microscope for a galvanostatic cycling test (Figure 2-7(a)). The white-light illumination source of the Raman microscope is replaced with a despeckled laser (Figure 2-7(a), interferometric laser) for interferometric measurement of the membrane deflection [13,151]. By employing the interferometric method, the same microscope used for the Raman spectroscopy analysis can be used to collect information on the membrane deflection, thus enabling multi-modal, real-time monitoring in a unified setup. All of the measurements are conducted in air under normal ambient conditions. The imaging software installed on the computer connected to the Raman microscope supports automation functions controlled by user specific operations programmed in JavaScript. This enables automatic switching between the two laser sources repeatedly throughout the experiment and computerized recording of the corresponding data. The recorded interference pattern and Raman spectra are automatically saved in the computer (Appendix A: JavaScript).

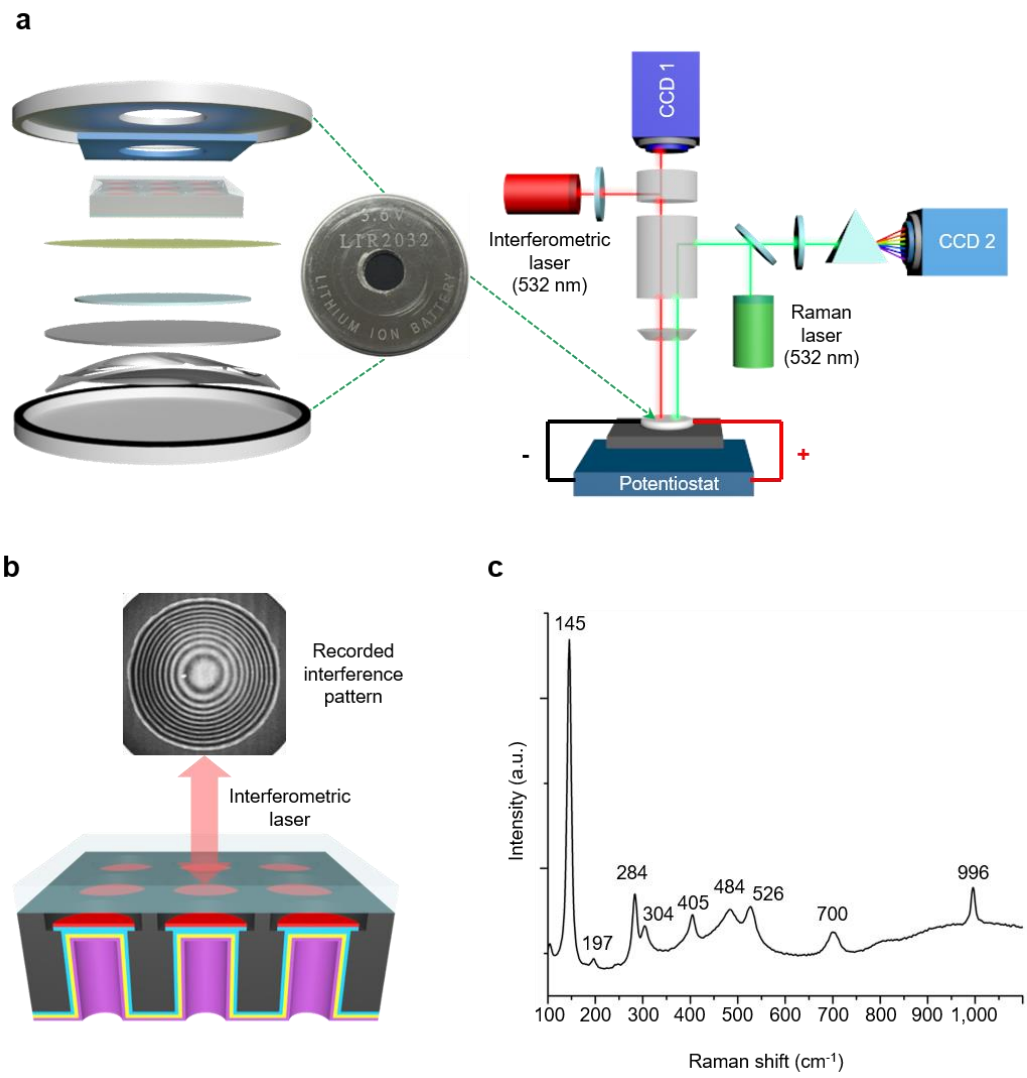

Figure 2-7: (a) Schematic of the coin cell parts (from top to bottom: cathode cap, adhesive tape, Fabry-Perot MEMS sensor, separator, lithium anode, stainless steel, spring, and anode cap) for *in situ* experiment and simplified schematic diagrams of the experimental setup showing the location of the coin cell under test relative to the Raman microscope. (b) Optical image of the experimentally obtained interference pattern from the membrane. (c) Experimentally obtained Raman spectrum of as-deposited V_2O_5 thin film electrode underneath the membrane.

When the interferometric laser illuminates one of the membranes in the optical cavity of the sensor, it produces an interference pattern (Figure 2-7(b)). The as-fabricated sensor membranes have some residual stress associated with the fabrication

and the anodic bonding processes which result in upward curvature [13]. Due to this pre-deflected circular membrane, the initial interference pattern already shows multiple concentric rings [151]. The Raman laser is used as the excitation source for Raman spectroscopy measurements to probe the V_2O_5 electrode underneath the membrane. The Raman spectrum of the as-deposited V_2O_5 thin film exhibits nine peaks in the 100-1000 cm^{-1} range, located at 145, 197, 284, 304, 405, 484, 526, 700, and 996 cm^{-1} (Figure 2-7(c)), in agreement with previously reported Raman spectra [152], indicating that the excitation laser penetrates the glass wafer and the semi-transparent multi-layer membrane to probe the V_2O_5 electrode underneath.

2.3 Experimental results

2.3.1 Depth of discharge dependent studies

2.3.1.1 *In situ* visualization of structural changes of V_2O_5 electrode

The Fabry-Perot MEMS sensor coated with ALD-deposited V_2O_5 thin film electrode is first used to evaluate the electrochemical properties of the V_2O_5 inside the modified coin cell (Figure 2-8(a)). The discharge curve shows several resolved plateaus corresponding to well-known phase transitions during lithiation of V_2O_5 [3,153,154]. The α-, ε-, δ-, γ-, ω-V_2O_5 phases are identified within the voltage range from 3.75 to 1.5 V. The α- to ε-phase and ε- to δ-phase transformation plateaus appeared at 3.4 and 3.2 V, respectively. Then the δ- to γ-phase and γ- to ω-phase transitions are observed at the 2.3 and 2.05 V plateaus, respectively. The observed electrochemical behavior validates that the customized cell is functional both in terms of its design to provide

good electrical contacts to the cathode layers, as well as adequate hermetic seal such that the cell can be reliably operated in the ambient.

Table 3: Lattice parameters for different phases of $Li_xV_2O_5$ electrode [3,155].

Lattice parameters	**$Li_xV_2O_5$**					
	x = 0.0 (α-V_2O_5)	x = 0.4 (ε-V_2O_5)	x = 1.0 (δ-V_2O_5)	x = 1.4 (δ-V_2O_5)	x = 2.0 (γ-V_2O_5)	x = 3.0 (ω-V_2O_5)
a (Å)	11.51, 11.51	11.38, 11.44	11.24, 11.26	11.42	9.69	4.1
b (Å)	3.56	3.57	3.60	3.57	3.60	4.1
c (Å)	4.37, 4.38	4.52, 4.50	9.91, 4.96	4.96	10.67	4.1

In Figure 2-8(b)-(d), we show schematically the structural transformations in $Li_xV_2O_5$ as x increases from 0 to ~3, corresponding to the series of α- to ω-phases [153,154]. During lithiation, the structure of the $Li_xV_2O_5$ layer remains stable in the α-, ε-, and δ-phases (Figure 2-8(b),(c)). However, a light puckering of the V_2O_5 layers is observed in the δ-phase (Figure 2-8(c)) due to the decrease in the *a* lattice parameter [154] (Table 3). When the voltage reaches the 2.3 V plateau ($1<x<2$ in $Li_xV_2O_5$), the δ-phase is transformed into the γ-phase, a substantially distinct structure (Figure 2-8(d)). While the V_2O_5 layers remain perpendicular to the *c*-axis, the Li-ions are shifted along the *a*-axis direction and the puckering of the V_2O_5 layers becomes more pronounced as the *a* lattice parameter further contracts [3,30,154]. Finally, when the voltage reaches the 2.05 V plateau ($x>2$), the γ-phase is irreversibly transformed into the ω-phase.

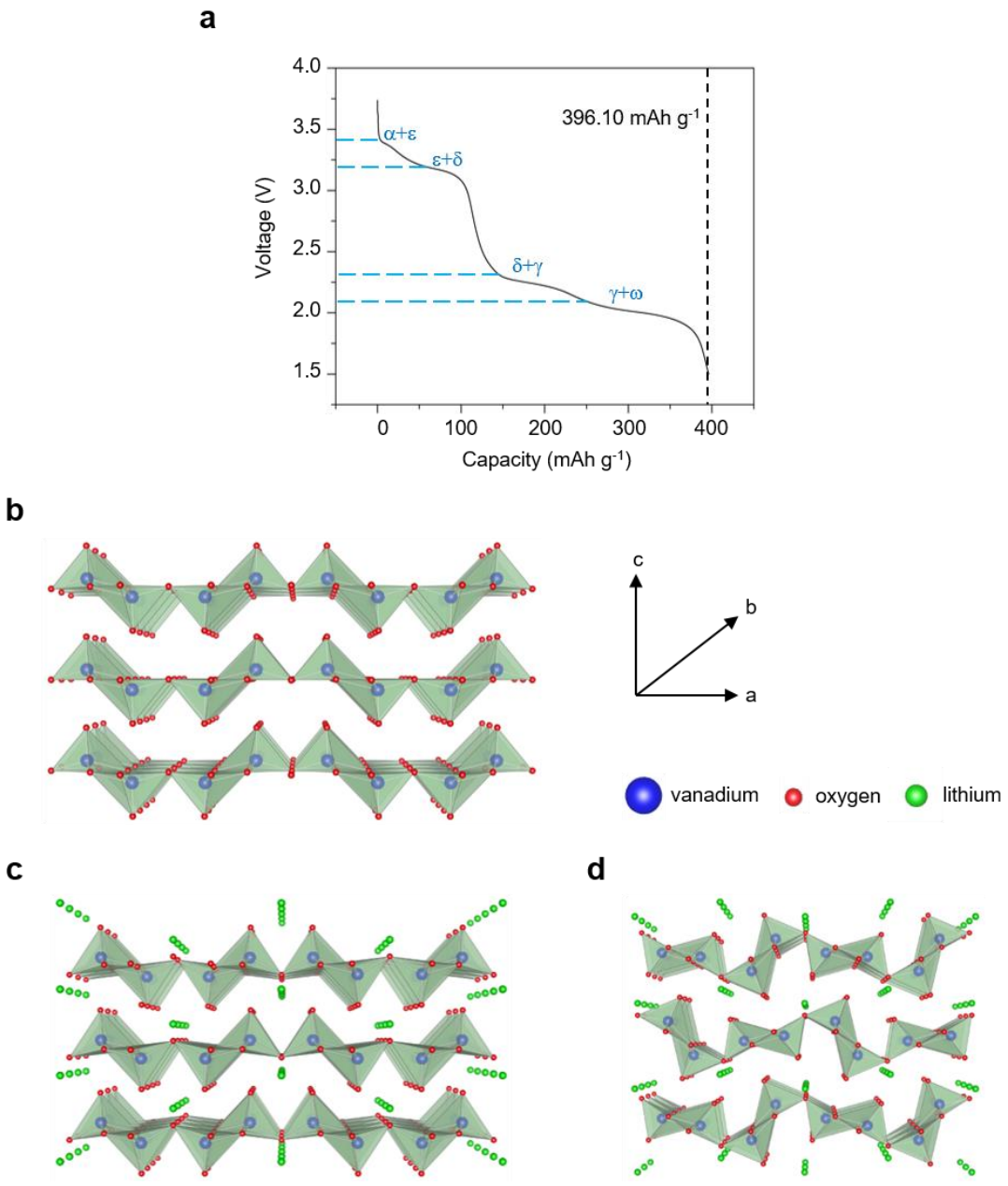

Figure 2-8: Electrochemical discharge curve of ALD-deposited V_2O_5 thin film electrode in the customized cell and schematic representation of the electrochemically produced $Li_xV_2O_5$ structure. (a) Galvanostatic Li-ion insertion curve at C/12 rate. Phase-transformation plateaus at 3.4 V (α- to ε-phase), 3.2 V (ε- to δ-phase), 2.3 V (δ- to γ-phase), and 2.05 V (γ- to ω-phase) are observed (labeled in blue). (b-d) Perspective view of the $Li_xV_2O_5$ structure in different phases: (b) α-phase, (c) δ-phase, and (d) γ-phase.

Figure 2-9(a) displays galvanostatic discharge-charge curves of the ALD-deposited V_2O_5 thin film electrode at a current of 4.563 μA in three different voltage windows. These voltage ranges are chosen in order to induce different phase transitions in the $Li_xV_2O_5$ electrode [3,153,154]. The first window (3.75 - 2.8 V) corresponds to the reversible α-, ε-, and δ-phase transitions and the pristine V_2O_5 phase is recovered upon lithium extraction [3]. In this voltage range, the pristine V_2O_5 structure remains intact except for a minor puckering occurring along the *a* axis (Figure 2-8(b),(c)). However, in the second window (3.75 - 2.1 V) the δ-phase is transformed into the metastable γ-phase at 2.3 V. This transformation is accompanied by irreversible structural changes in the $Li_xV_2O_5$ film. The third window (3.75 - 1.5 V) leads to a weakly crystallized ω-phase with a tetragonal [156] or cubic [157] structure when the voltage reaches the 2.05 V plateau.

Within the first window of 3.75 to 2.8 V where the pure V_2O_5 layer structure is preserved, the optical interference patterns from the circular membrane remain relatively symmetric (Figure 2-9(b)(1),(2),(3)), as expected since there are no significant asymmetric contractions in the V_2O_5 lattice (Table 3). In the second window (3.75 - 2.1 V) the δ-phase is transformed into the γ-phase with pronounced puckering of the V_2O_5 layers. These structural changes are reflected as loss in symmetry in the interference pattern (Figure 2-9(b)(4)). Given that the δ- to γ-phase transition is irreversible[41], it is not surprising that the interference pattern remains asymmetrical, even as the potential is cycled back to 3.75 V (Figure 2-9(b)(5)). In the third window (3.75 - 1.5 V), $Li_xV_2O_5$ is transformed from the γ- to the ω-phase with significant

structural rearrangement [153], which is again captured well by the evolution of the interference patterns during the lithiation process (Figure 2-9(b)(6),(7),(8)). The previously observed asymmetric interference patterns becomes even more pronounced due to the further asymmetric contraction in the *a* lattice parameters during the δ- to γ-phase transition. However, after when the γ-phase is completely transformed into the ω-phase, the *a* and *b* lattice parameters becomes equal, resulting in the recovery of the symmetric interference pattern (Figure 2-9(b)(8)). Since the ω-phase is irreversible, the interference pattern remains symmetric throughout further electrochemical cycling (Figure 2-9(b)(9),(10)). The weakly crystalline ω-phase exhibits similar electrochemical behavior of an amorphous V_2O_5 electrode upon further cycling. These results demonstrate how structural evolutions in electrode material during lithiation can be optically imaged in real time using the Fabry-Perot MEMS sensor platform. This visualization is enabled by the unique design of the Fabry-Perot MEMS sensor, which has the thin and flexible membrane inside the optical cavity, which allows monitoring of significant structural evolution in the electrode by merely observing the series of interference pattern images recorded during the experiment.

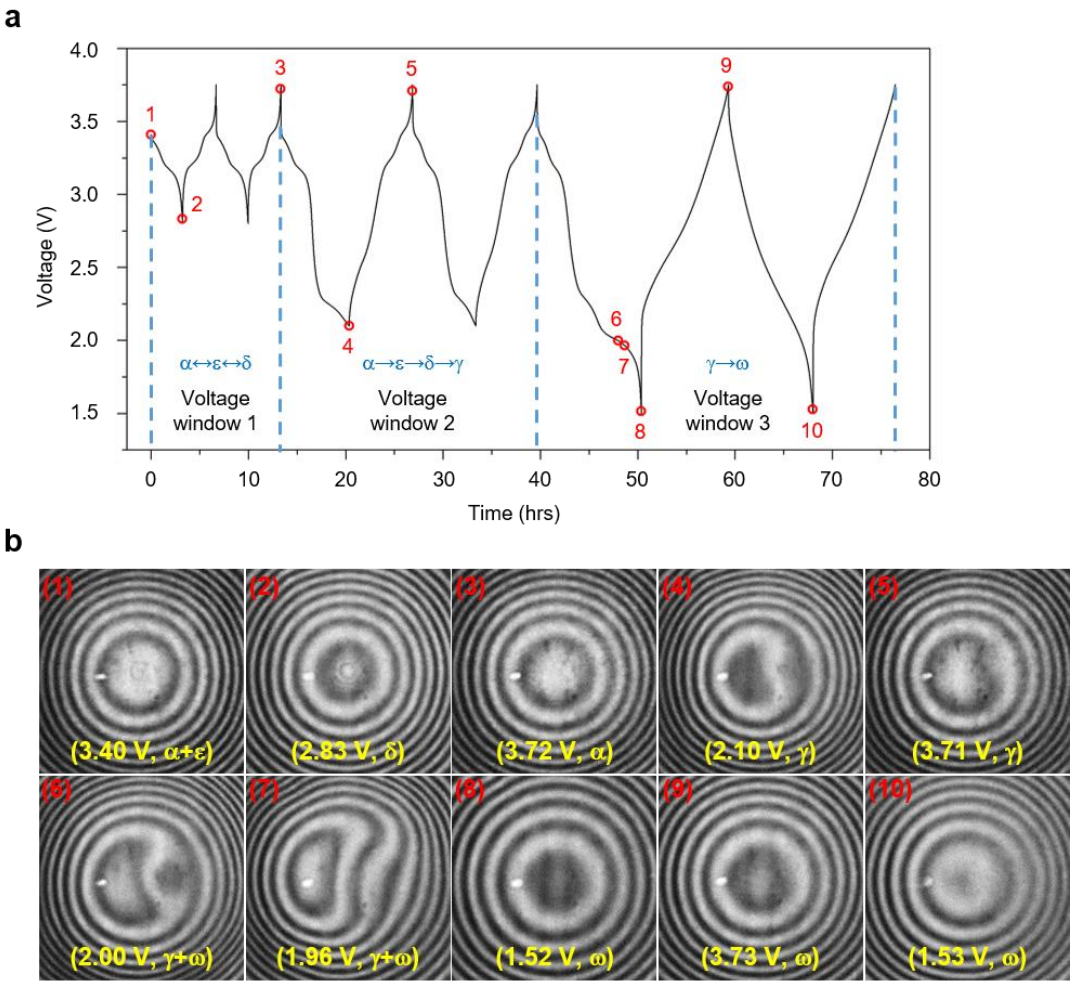

Figure 2-9: (a) Galvanostatic discharge-charge cycling curve of the ALD-deposited V_2O_5 electrode achieved from the *in situ* experimental setup. The phase transitions corresponding to the voltage windows are specified in blue. Red circles correspond to the point where the interference patterns are recorded. (b) Series of experimentally obtained interference patterns collected along the discharge-charge curve (red circles) indicated with the potential and phase (in yellow). Initial deformation of symmetric interference pattern is observed (4), followed by dramatic interference pattern change (6-7), and symmetric interference pattern is recovered (8).

2.3.1.2 *In situ* analysis of qualitative stress

To analyze the stress changes in the V_2O_5 electrode during lithiation, the recorded interference patterns are processed using MATLAB. First, the interference pattern of the pristine electrode is compared to the interference patterns of the electrode

under testing (Figure 2-10(a)). Each of the interference patterns is composed of multiple concentric rings and the edge of the inner most ring is utilized to track the radius change (Figure 2-10(b), fringe radius change). In our previous work, it was verified that the fringe radius change varies linearly with the stress residing in the membrane [13] ($R^2 = 0.987$). Therefore, expansion of the fringe radius is denoted with a positive sign, and corresponds to compressive stress, with negative values conversely indicating tensile stress [13].

Correlation between the stress change and electrochemical discharge-charge of the first two cycles (Figure 2-9(a), first voltage window) are show in Figure 2-11(a),(b). Upon lithium intercalation, the stress in the electrode becomes more tensile. This result should be explained in accordance with changes in the *a* and *b* lattice constants of the $Li_xV_2O_5$. As previously shown in Figure 2-3(b), the V_2O_5 film has a preferred (001) orientation with respect to the membrane. Therefore, changes in the *c* parameter do not affect the stress in the membrane since it is free to expand. However, elongation (contraction) in the *a* and *b* lattice parameters result in an increasing compressive (tensile) stress. Previous XRD studies have shown that the *a* lattice parameter continuously decreases as $Li_xV_2O_5$ changes from α- to δ-phase while the *b* parameter remains relatively constant (Table 3). This agrees with the observed increase in the tensile stress in the electrode. Inflections in the stress-potential curves such as regions I and II in Figure 2-11(b) likely correspond to α- to ε-phase and ε- to δ-phase transitions which we discuss in more detail later. Upon lithium extraction, the stress returns to its initial value.

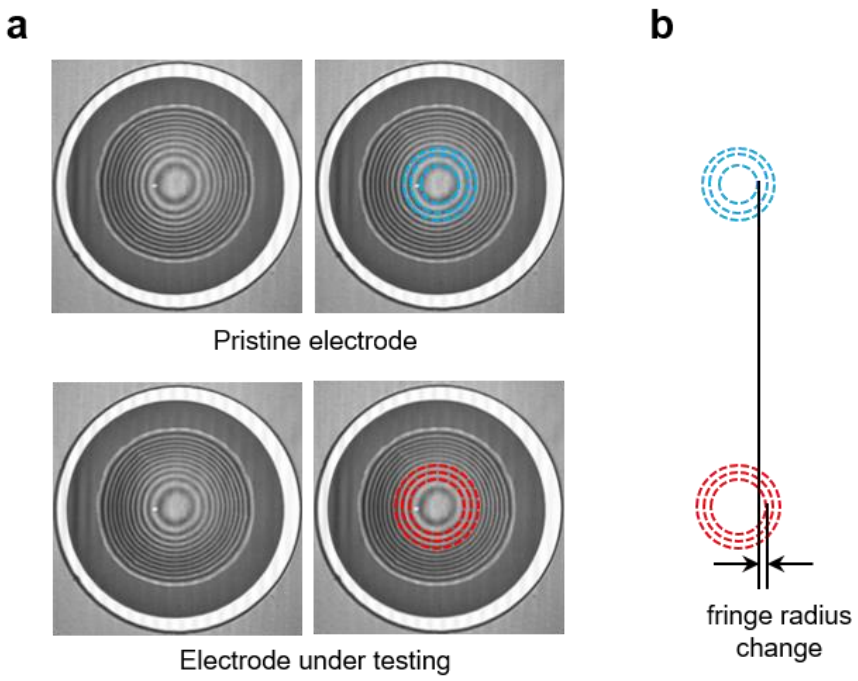

Figure 2-10: (a) Optical images of experimentally obtained interference patterns from pristine electrode and electrode under testing (blue and red dotted lines are for visual guidance). (b) Diagram showing the 'fringe radius change' between the pristine electrode and electrode under testing.

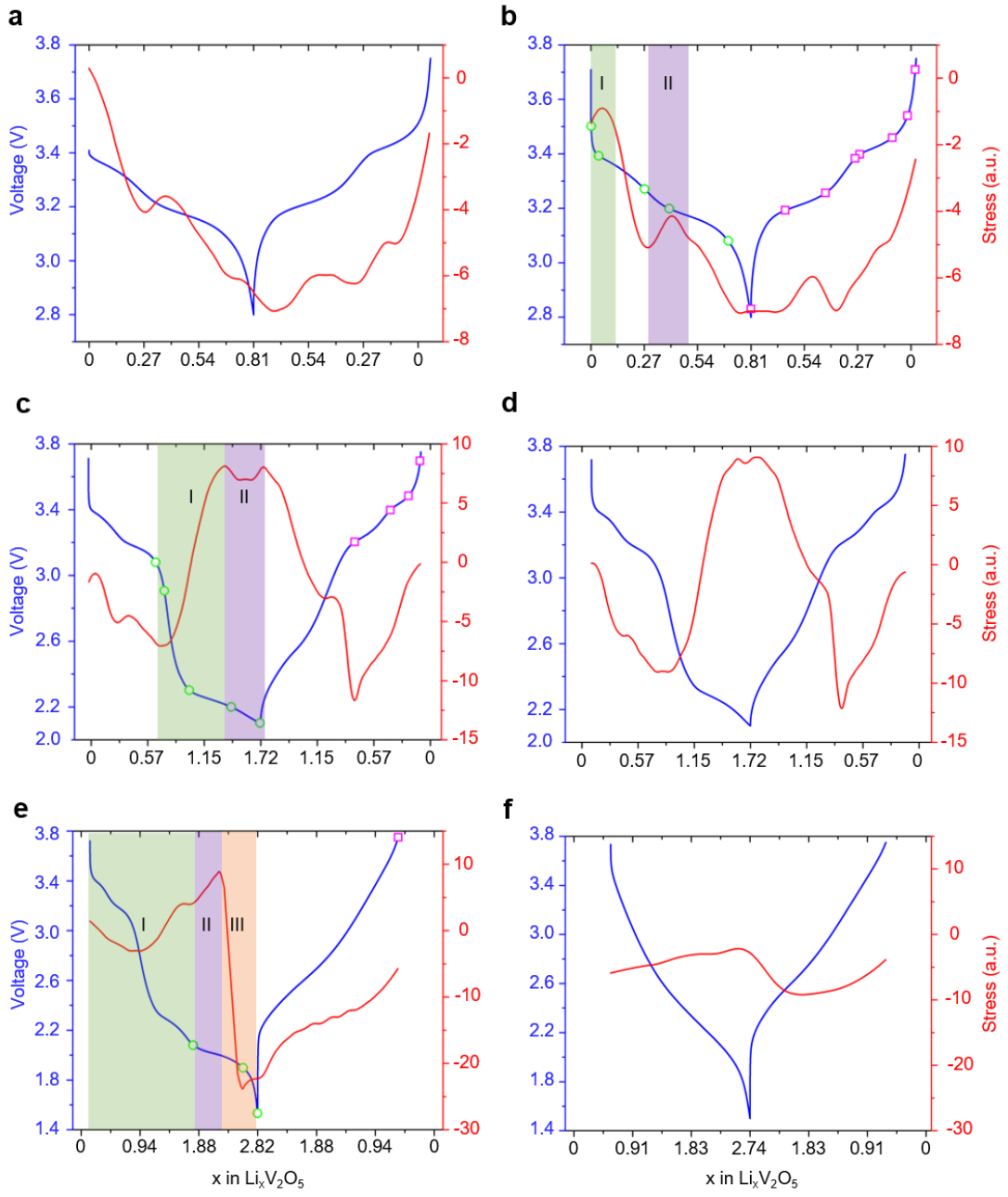

Figure 2-11: (a,b) Correlation between the stress change and potential variation during discharge-charge of the first and second cycles. (b) Circles in green and rectangles in magenta correspond to the representative points where *in situ* µRaman spectra are analyzed during the second discharge-charge cycle, respectively. (c,d) Correlation between the stress and discharge-charge curves of the third and fourth cycles. (c) Circles in green and rectangles in magenta correspond to representative points where *in situ* µRaman spectra are analyzed during the third

discharge-charge cycle, respectively. (e,f) Correlation between the stress change and discharge-charge curves of the fifth and sixth cycles. (e) Circles in green and rectangles in magenta correspond to the representative points where *in situ* μRaman spectra are analyzed during the fifth discharge-charge cycle, respectively.

Analysis on the stress change and electrochemical discharge-charge of the third and fourth cycles Figure 2-9(a), second voltage window) are shown in Figure 2-11(c),(d), with similar stress change upon discharge as seen in Figure 2-11(a),(b). However, further lithiation (discharge) alters this trend with stress becoming more compressive stress (Figure 2-11(c), region I). This can be attributed to the elongation of the a lattice parameter during the δ- to γ-phase transformation [158]. However, upon further discharge, the stress in the electrode becomes more tensile (Figure 2-11(c), region II). This change coincides with the pronounced puckering of the V_2O_5 layer in the γ-phase (Fig. 3d) due to the contraction in the *a* lattice parameter (Table 3). Upon charge, the same trend is observed as the relative stress returns to its initial value. The fourth cycle exhibits a similar stress change as observed for the third cycle (Figure 2-11(d)), even though the $Li_xV_2O_5$ electrode is transformed from δ- to γ-phase. This indicates that the overall V2O5 layer structure is generally preserved in the γ-phase compared to the δ-phase structure, except the puckering of the V_2O_5 layers (Figure 2-9(b)(5)).

Superpositions of the discharge-charge curves with the stress changes for the fifth and sixth cycles (Figure 2-9(a), third voltage window) are show in Figure 2-11(e),(f). The same trend is observed until the voltage reaches 2.1 V

(Figure 2-11(e), region I). Upon further discharge, stress in the electrode becomes more compressive (Figure 2-11(e), region II) due to the more pronounced puckering of the V_2O_5 layer in the γ-phase, as indicated by the augmented asymmetric fringe pattern (Figure 2-9(b)(6)). Still further lithiation induces a sudden change in the stress (Figure 2-11(e), region III) which rapidly becomes highly tensile, indicating the electrode experiences a dramatic structural transformation from the γ-phase to the tetragonal ω-phase [153]. This tetragonal structure has significantly shorter lattice parameter (a = 4.1 Å) compared to the γ-phase (Table 3), which explains the sudden increase in the tensile stress [159]. The ω-phase remains stable even after lithium extraction [157] consistent with the completely different stress change during the sixth cycle (Figure 2-11(f)). Upon lithium insertion, the stress in the electrode becomes more compressive, implying that the $Li_xV_2O_5$ thin film electrode became amorphous [159]. However, upon charge, the stress in the electrode becomes more tensile initially but turns into more compressive stress again in the middle of the process. This may be attributed to the rocksalt type structure of the ω-phase, resulting in the non-linear stress change. The stress evolution during lithiation is in good agreement with the previously reported phase changes and lattice parameters changes in $Li_xV_2O_5$, confirming the high sensitivity of the platform.

2.3.1.3 *In situ* analysis of microstructural changes

Concomitant with the stress measurements, a series of *in situ* μRaman spectra of the $Li_xV_2O_5$ electrode are collected and analyzed. The Raman spectra reveal a

complete recovery of the pristine V_2O_5 electrode, with regard to relative intensities and peak positions (Figure 2-12) during the second cycle.

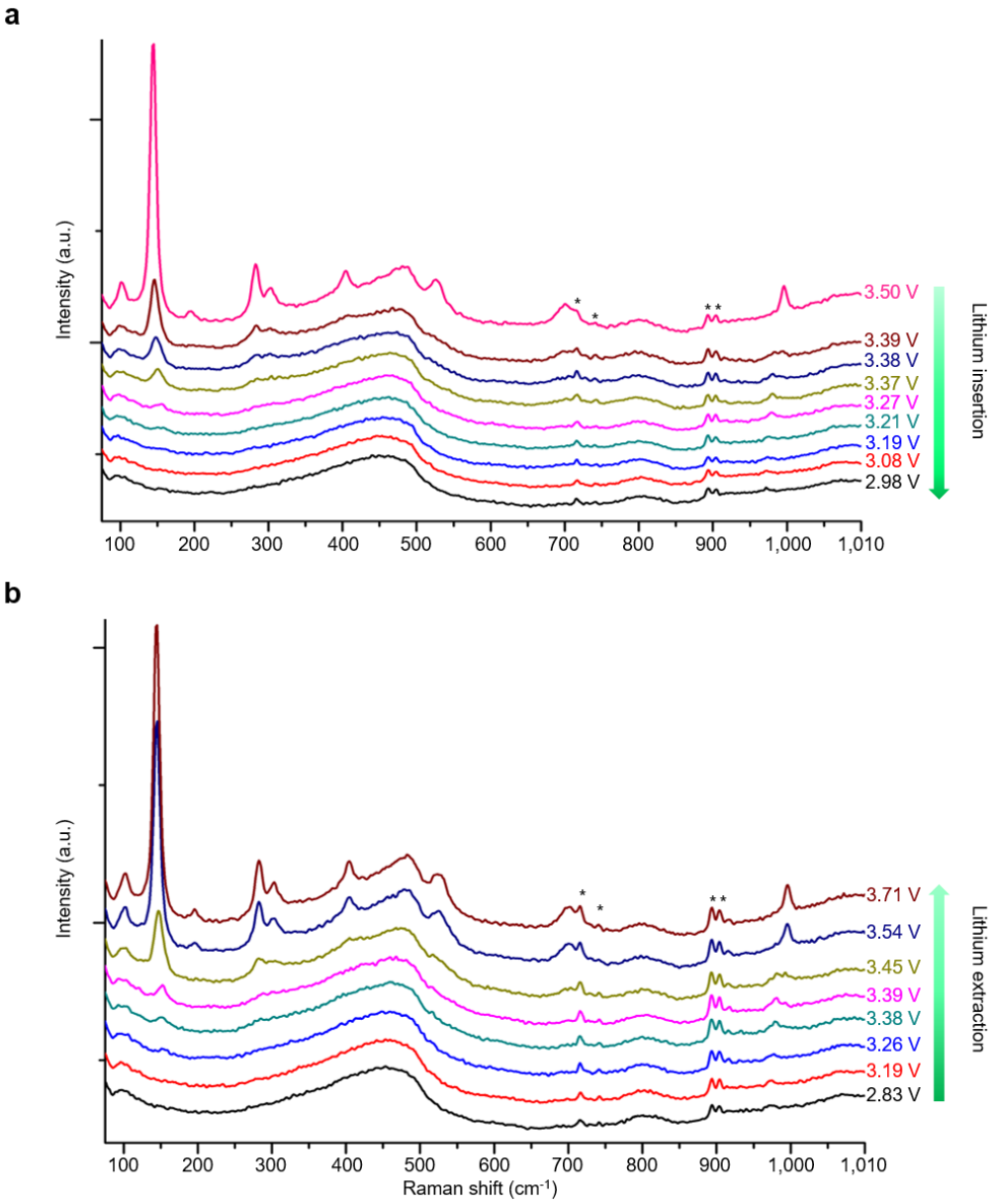

Figure 2-12: Full intensity *in situ* Raman spectra collected during the (a) second discharge (lithium insertion) and (b) charge (lithium extraction) cycle of the $Li_xV_2O_5$ electrode. *Stars denote $LiPF_6$/EC/DMC bands.

This finding is consistent with the high electrochemical reversibility associated with the first voltage window [29,160] (3.8 - 2.8 V).

During the second cycle discharge process (Figure 2-11(b)), a progressive decrease in the intensity and the Raman shift (145 - 154 cm^{-1}) are observed for the low frequency vibration modes (mixture of B_{1g} and B_{3g} modes) sensitive to long range order in the $Li_xV_2O_5$ structure (Figure 2-13). There is also a considerable loss of intensity for all the Raman peaks in the 195 to 705 cm^{-1} range. Finally, in the vanadyl stretching mode (996 cm^{-1}), a new peak at 983 cm^{-1} is observed at potential of 3.39 V while the initial peak (996 cm^{-1}) disappears at potential of 3.27 V. The new peak progressively shifts down to 972 cm^{-1} as more Li-ions are inserted into the electrode. These findings are consistent with previous Raman studies of $Li_xV_2O_5$ electrodes [3,133,152]. The emergence of the new peak at 983 cm^{-1} in the vicinity of the 996 cm^{-1} at potential of 3.39 V has been previously related to a coexistence of the α- and ε-phases [161] and the 973 cm^{-1} peak at the potential of 3.20 V has been ascribed to the presence of ε- and δ-phases [161]. This coexistence of two distinct phases of $Li_xV_2O_5$ as suggested by Raman spectra coincides with the abnormal stress changes observed with the Fabry-Perot MEMS sensor during the second cycle discharge process (Figure 2-11(b), region I and II).

It has been proposed that the Raman shift from 145 cm^{-1} to 154 cm^{-1} is due to an increase in the restoring force as a consequence of tensile stress in the $Li_xV_2O_5$ film [31]. The combined approach is now able to confirm this hypothesis by correlating the evolution of the Raman shift at 145 cm^{-1} with the stress change as a function of the

lithium insertion in $Li_xV_2O_5$ electrode (Figure 2-14). As the amount of lithium increases during lithiation, the translational mode at 145 cm^{-1} progressively increased to 154 cm^{-1}.

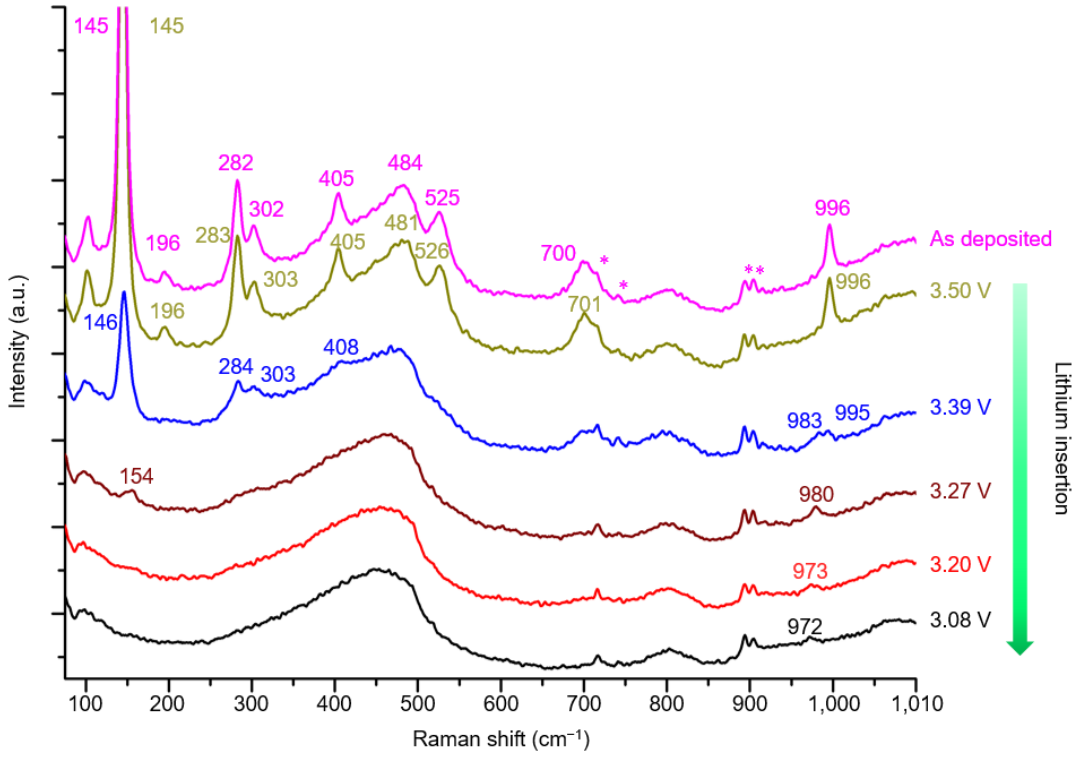

Figure 2-13: Detailed view of *in situ* Raman spectra. Detailed view of the *in situ* Raman spectra collected during the second discharge (lithium insertion) process of the $Li_xV_2O_5$ electrode. *Stars denote $LiPF_6$/EC/DMC bands.

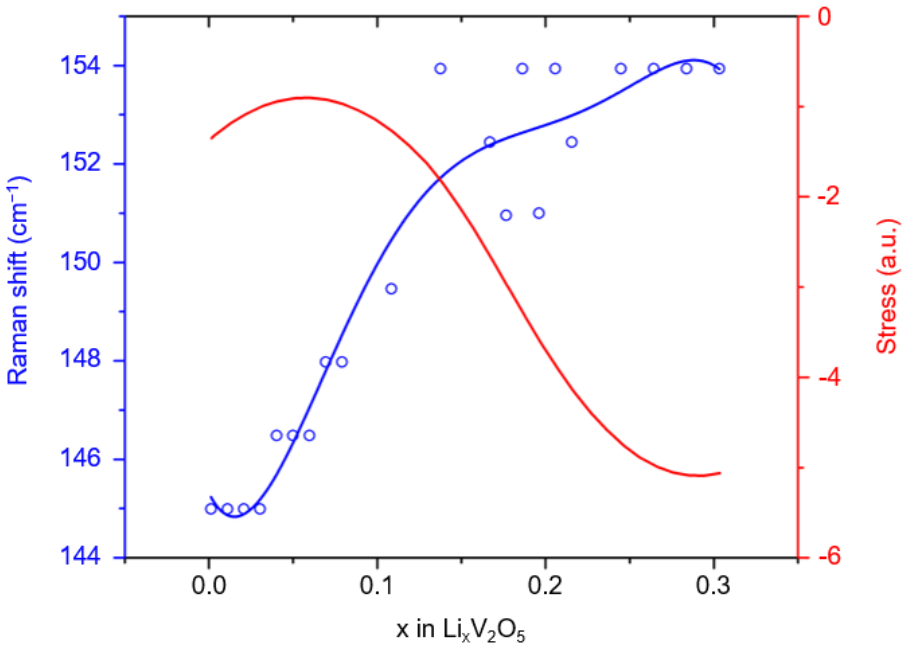

Figure 2-14: Raman shift and stress change. Correlation between the peak shift of the Raman translational mode at 145 cm^{-1} (associated with long range order) and the stress change as a function of the lithium insertion in $Li_xV_2O_5$ electrode.

The *in situ* Raman spectra collected for the third discharge and charge processes (Figure 2-11(c)) are shown in Figure 2-15. Upon discharge, the same stretching mode (972 cm^{-1}, Fig. 7 at 3.08 V) is observed at 3.08 V (Figure 2-15(a)). However, the peak shifts to higher wavenumbers upon further lithiation and completely disappears at 2.10 V (Figure 2-15(a)). These spectral changes can be attributed to irreversible loss in crystallinity during formation of the γ-phase [30]. This irreversible change is also evidenced by the fact that some of the modes (196, 302, 484, and 700 cm^{-1}) are no longer observed after the electrode is charged back to 3.70 V (lithium extraction) (Figure 2-15(b)). Similarly, the peaks at 144 cm^{-1} and vanadyl stretching mode at 997 cm^{-1} do not recover their original intensity, indicating high degree of disorder in the

V_2O_5 layer. Finally, the peak at 975 cm^{-1} associated with the γ-phase is still observed even after all the lithium extraction (Figure 2-15(b), 3.70 V), which is consistent with the irreversibility of this phase [154].

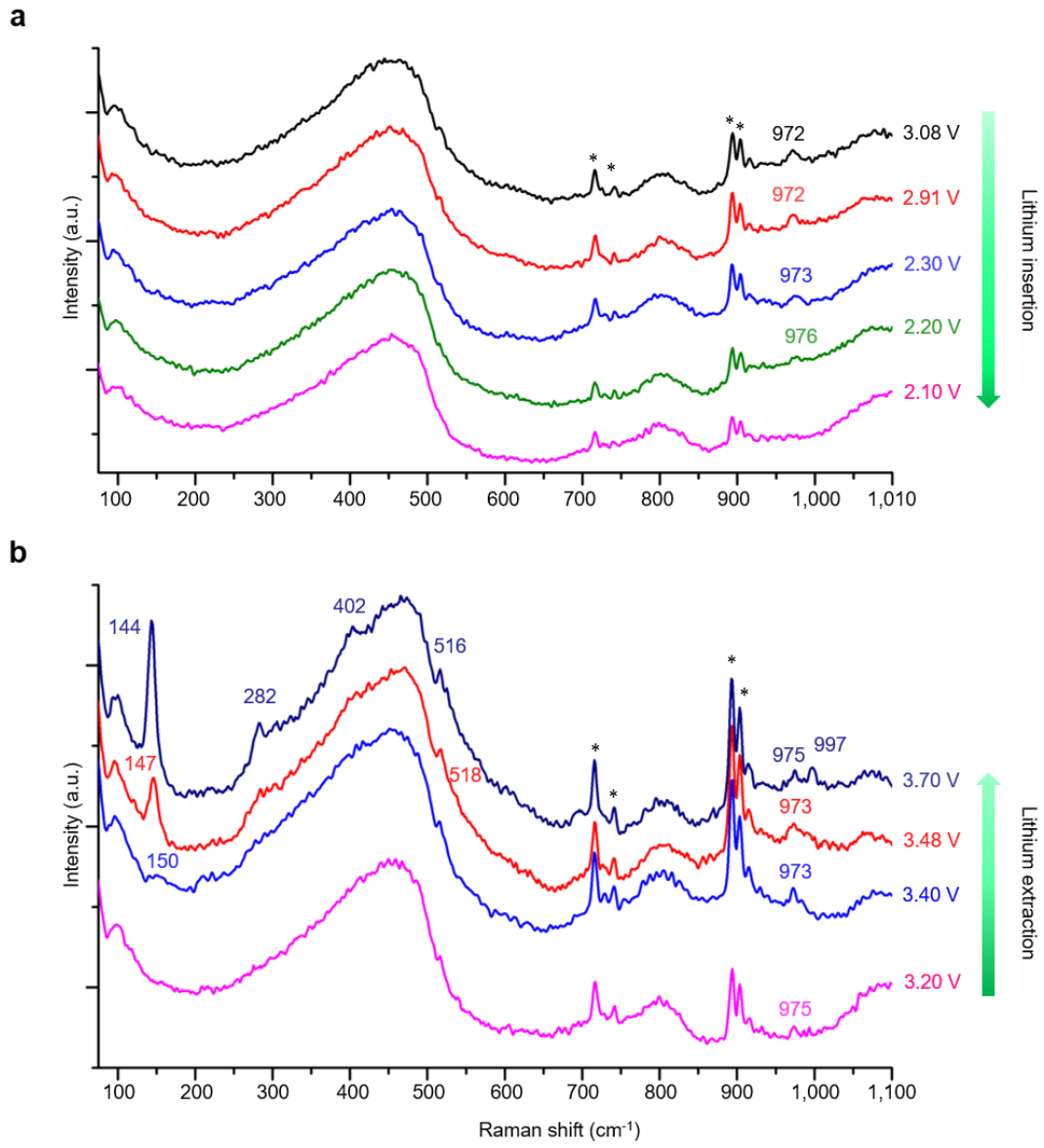

Figure 2-15: Detailed view of the *in situ* Raman spectra collected during the third dischrage and charge cycle of the $Li_xV_2O_5$ electrode in the voltage range of (a) 3.08 to 2.10 V and (b) 3.20 to 3.70 V. *Stars denote $LiPF_6$/EC/DMC bands.

The *in situ* Raman spectra collected for the fifth discharge and charge processes (Figure 2-11(e)) shown in Figure 2-16 display no discernable peaks, indicating that Raman is not able to detect the γ- to ω-phase transition in contrast to the already shown results with the *in situ* Fabry-Perot MEMS sensor (Figure 2-9(b)(6), (7), (8)) (Figure 2-11(e), region III). Even after the electrode is charged back to 3.75 V, no detectable peaks are found, suggesting that the electrochemically formed weakly crystalline ω-phase has a nearly amorphous structure and remains in this metastable state even all the lithium extraction [157].

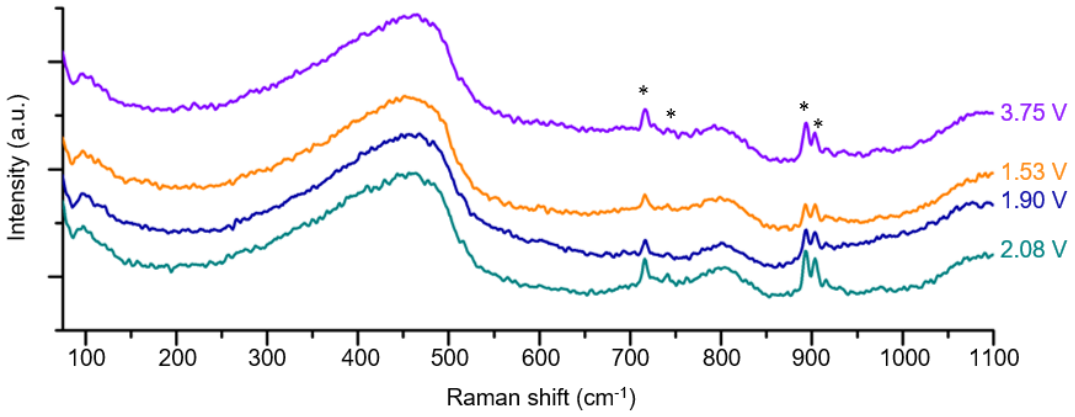

Figure 2-16: Detailed view of the *in situ* Raman spectra collected during the fifth discharge and charge cycle of the $Li_xV_2O_5$ electrode. *Stars denote $LiPF_6$/EC/DMC bands.

The *in situ* μRaman spectroscopy measurement results achieved using the platform match well with the previously Raman study of V_2O_5 electrodes [3,133,152], indicating this technique is capable of characterizing both the stress and microstructural changes concurrently. Fully reversible α- to δ-phase transitions are observed as well as the irreversible transformation in the γ-phase and weakly crystallized ω-phase are

evidenced for the first time using *in situ* μRaman spectroscopy technique in a single, continuous experiment.

2.3.2 C-rate dependent studies

2.3.2.1 *In situ* analysis of qualitative stress

This section investigates the qualitative stress and structural changes in a thin film V_2O_5 electrode over multiple discharge/charge cycles. This has been done by varying charge rates (C-rates). Charge rate has been identified as an important factor affecting the battery performance. Furthermore, the impact of charge rate on the structure and associated stress in the electrode have been analyzed. To achieve better analysis of the stress changes in the $Li_xV_2O_5$ electrode during lithium cycling, an intensity change of the interference pattern achieved from the Fabry-Perot MEMS sensor membrane is recorded throughout the experiment. As the stress in the electrode changes during the discharge-charge processes, the flexible membrane deflects causing the intensity of the interference pattern to change. First, the interference pattern of the pristine electrode (Figure 2-17(a), before the first discharge process started) is recorded and then compared to the interference patterns of the electrode under testing (Figure 2-17(b)). Specifically, the intensity changes at the center of the membrane are analyzed since it is the part of the membrane most sensitive to stress changes.

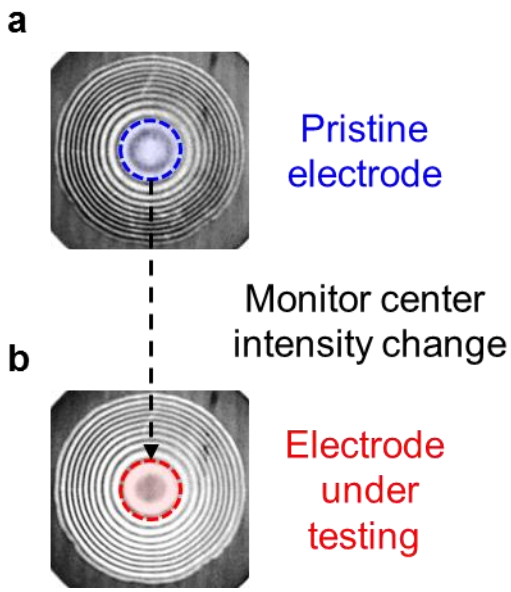

Figure 2-17: (a) Interference patterns of the pristine electrode and (b) electrode under testing. Intensity change at the center of the membrane is highlighted within the dotted circles.

In order to verify that the intensity change varies linearly with the stress in the membrane, the interference intensity change as a function of the stress in the membrane is simulated using MATLAB (Figure 2-18). The details of the analytical equations used in the simulation can be found in our previous work [13]. According to the simulation, the interference intensity varies linearly with the stress in the membrane ($R^2 = 0.99$). Therefore, a decrease in the interference intensity directly corresponds to increasing tensile stress in the membrane, with an increase in the intensity conversely corresponding to increasing compressive stress.

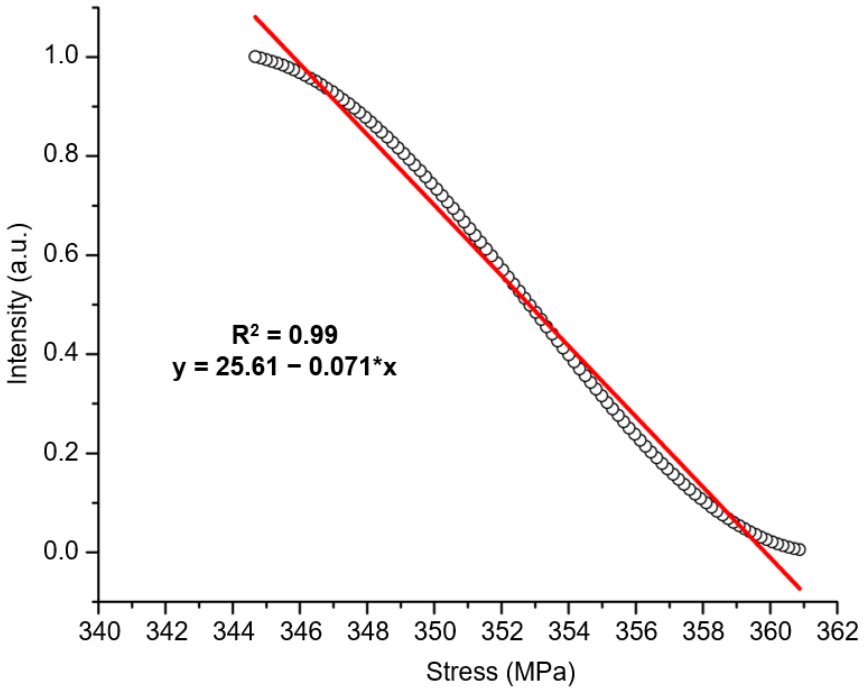

Figure 2-18: Correlation between the interference pattern intensity change and linearly varying stress in the membrane. Increasing tensile stress causes decrease in the interference pattern intensity.

Figure 2-19 shows galvanostatic discharge-charge curve of the ALD-deposited V_2O_5 thin film electrode upon cycling at different C-rates: C/4, C/2, 1C, and C/4. At each rate, the battery is tested for 2 cycles to minimize the impacts from previous cycles with different C-rates. The discharge-charge curve shows the α- to ε-phase and ε- to δ-phase transformation plateaus at 3.4 and 3.2 V, respectively. The observed electrochemical behavior corresponds to well-known phases transitions reported in the previous studies [153,154]. This result validates that the customized cell is functional both in terms of its design to provide good electrical contacts to the cathode layers, as well as adequate hermetic seal such that the cell can be reliably operated in the ambient.

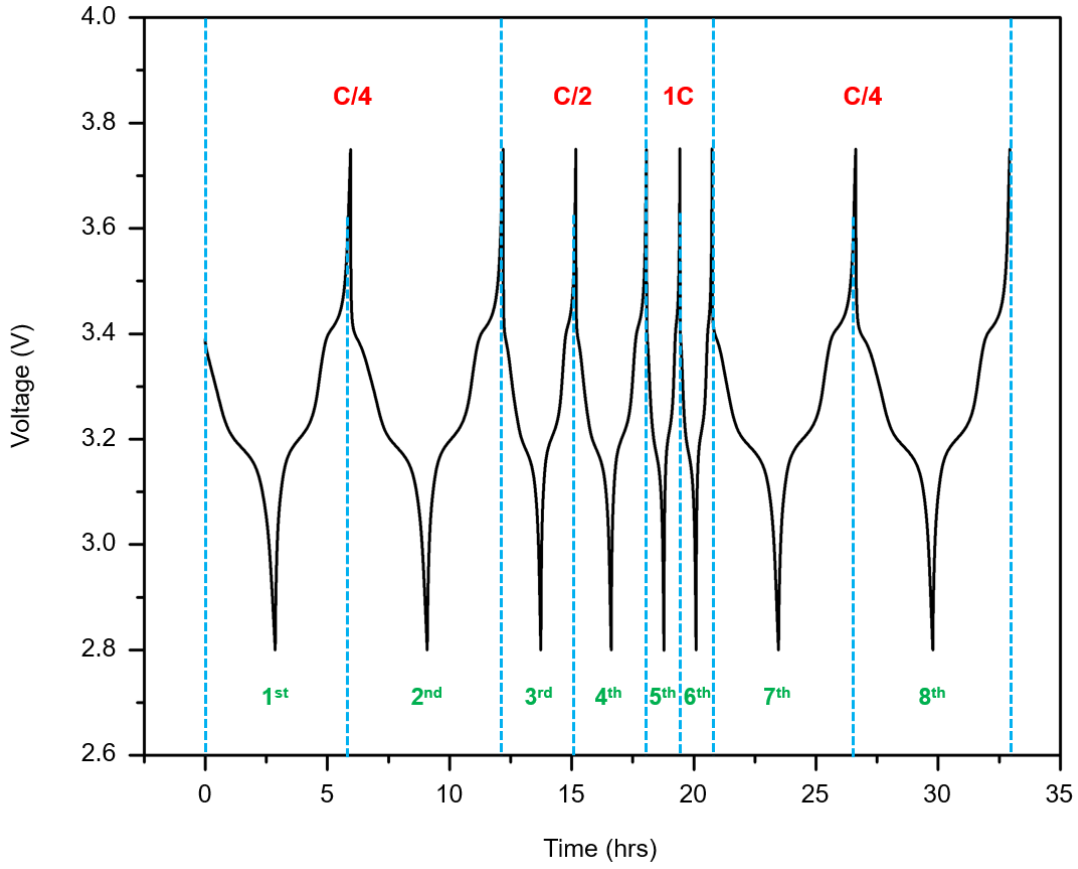

Figure 2-19: Galvanosatic discharge-charge cycling curve of the ALD-deposited V_2O_5 electrode achieved from the *in situ* experimental setup. Different C-rates (C/4, C/2, and 1C in red) have been applied for different cycles (indicated in blue) and their corresponding cycle numbers are indicated in green in the potential window of 2.8 – 3.75 V.

Correlation between the stress and electrochemical discharge-charge of the second cycle (C/4) is shown in Figure 2-20(a). Upon lithium intercalation, the stress in the electrode becomes increasing tensile in general (0.5 to 0.1, indicated in blue dotted arrow in Figure 2-20(a)). This result is expected according to the previous XRD studies. During the lithium intercalation process, the $Li_xV_2O_5$ changes from α- to δ-phase and the phase transition is accompanied by an evolutions in the *a* and *b* lattice constants.

Previous XRD studies have shown that the *a* lattice constant continuously decreases while the *b* parameter remains relatively constant during the phase transition.

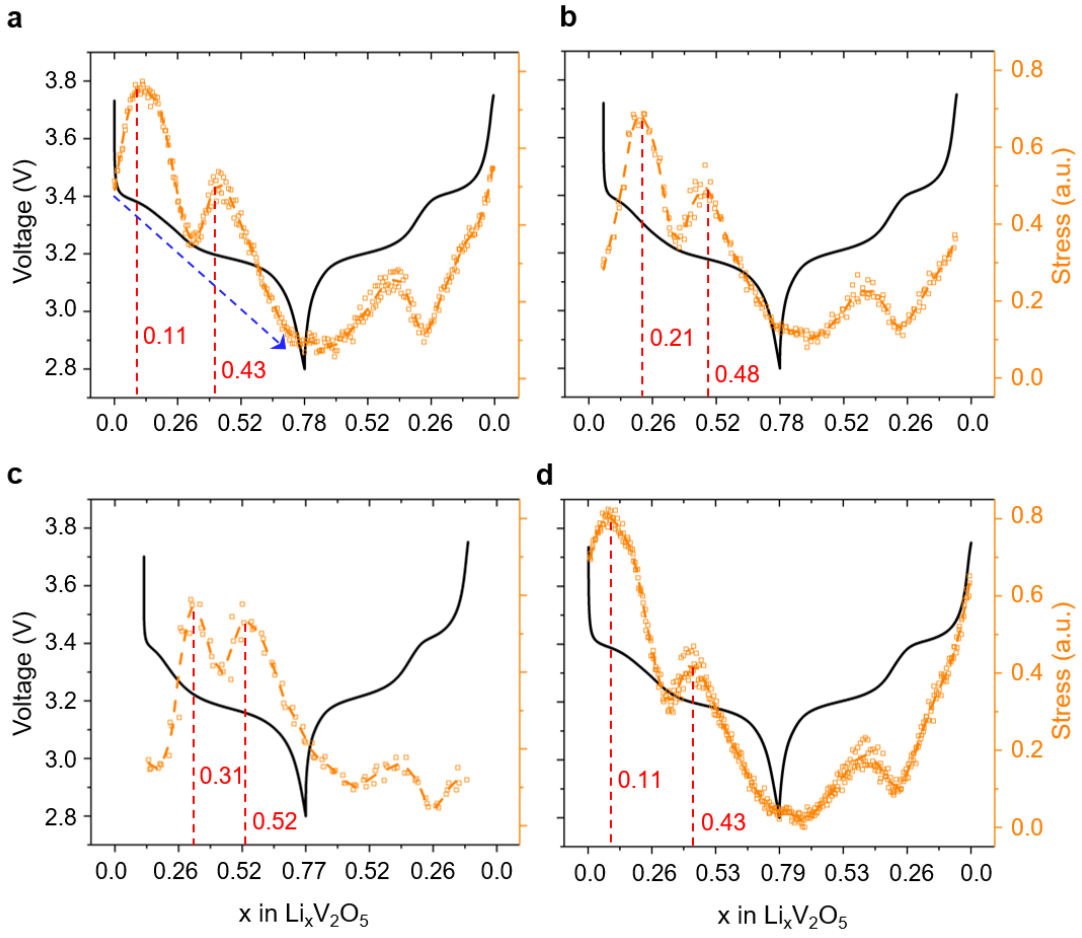

Figure 2-20: Correlation between the stress changes and potential variations during discharge-charge processes of the (a) second (C/4), (b) fourth (C/2), (c) sixth (1C), and (d) eighth cycles (C/4). Inflections observed during discharge processes are marked in red dotted lines.

Changes in the *c* lattice constant should not affect the stress in the membrane since it is free to expand. Therefore, these lattice constants changes should induce an increase in tensile stress, in line with the observed increase in the tensile stress in the electrode. At the same time, inflections in the stress changes are observed, indicated by the red

dotted lines in Figure 2-20(a), and these inflections coincide with well-known two-phase transitions (α- to ε-phase and ε- to δ-phase) during lithiation of V_2O_5 [3,153,154]. This observation indicates the coexistence of two distinct phases of $Li_xV_2O_5$ induces the abnormal stress changes in the electrode, which has not been reported in the previous XRD studies. Upon lithium extraction, the stress returns its initial value.

Analysis of the stress change and electrochemical discharge-charge of the fourth cycle is shown in Figure 2-20(b). Upon discharge process, similar stress change is observed, with the same inflections as seen in the second cycle (Figure 2-20(a)). However, the inflections in the stress change are emerged when the amount of lithium in $Li_xV_2O_5$ is greater (when x = 0.21 and 0.48) than the second cycle (when x = 0.11 and 0.43). The same phenomenon is also observed in the sixth cycle Figure 2-20(c)), and the inflections are observed when the amount of lithium in $Li_xV_2O_5$ is even greater (when x = 0.31 and 0.52). This behavior is believed to be the result of the low diffusion coefficient of lithium ions ($10^{-12} – 10^{-13}$ cm^2 s^{-1}) in V_2O_5 electrodes [162–165], which has been also reported by Soni *et al.* for thin film Si electrode [166]. When the $Li_xV_2O_5$ electrode is cycled at the lowest C-rate (C/4), lithium concentration gradient across the $Li_xV_2O_5$ film thickness is gradual. However, upon cycling at higher C-rates (C/2 and C), the greater amount of lithium is concentrated at the bottom of the $Li_xV_2O_5$ electrode where it is interfaced with the liquid electrolyte, causing a steeper lithium concentration gradient across the $Li_xV_2O_5$ film thickness. This diffusion limited insertion of lithium-ion in $Li_xV_2O_5$ electrode also explains the decreasing discharge capacity (115.53 to 96.40 mAh g^{-1}) when cycled at higher C-rates (C/4 to 1C).

Figure 2-21 displays correlation between the peak-to-peak stress change and discharge capacity variation for different C-rates. The peak-to-peak stress change increased linearly ($R^2 = 0.91$) with the discharge capacity, indicating that the magnitude of the stress change in the $Li_xV_2O_5$ electrode is determined by the total amount of lithium intercalated into the electrode rather than how fast/slowly it is discharged.

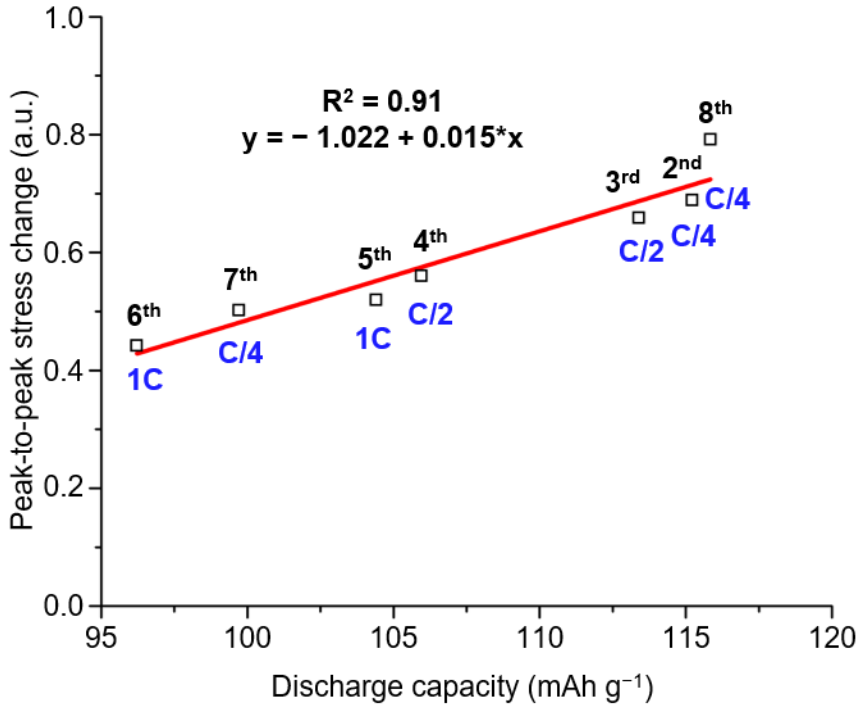

Figure 2-21: Correlation between the peak-to-peak stress change and discharge capacity variation at different cycles. Cycle numbers are specified in black and their corresponding C-rates are specified in blue.

2.3.2.2 *In situ* analysis of microstructural changes

It has been previously reported that an increase of disorder within the $Li_xV_2O_5$ electrode due to the lithium intercalation process leads to a significant decrease in intensity of the 145 cm^{-1} mode (mixture of B_{1g} and B_{3g} modes) [3,133]. Therefore, changes in the intensity (peak height) of the 145 cm^{-1} mode during lithium insertion

(discharge) has been characterized (Figure 2-22) in order to investigate how the level of disorder in the $Li_xV_2O_5$ electrode changes when it is cycled at different C-rates.

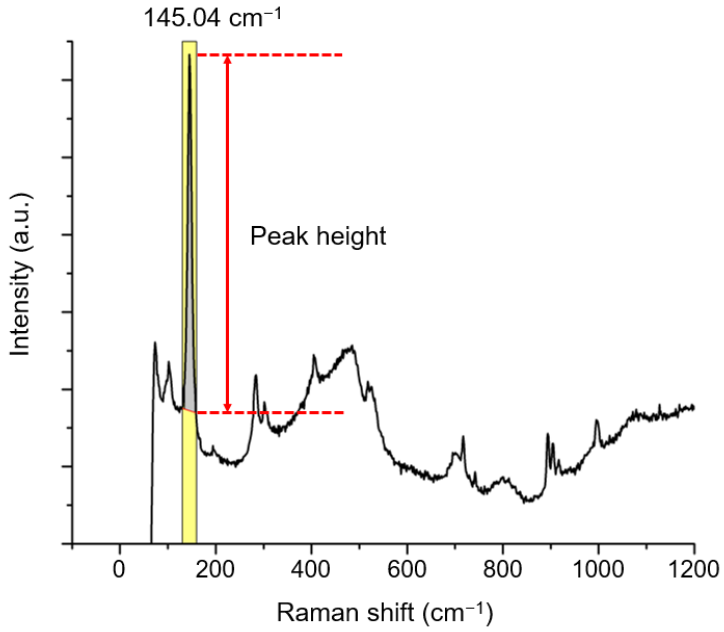

Figure 2-22: *In situ* Raman spectrum collected during the second discharge process of the $Li_xV_2O_5$ electrode and diagram showing how the peak height of the 145 cm^{-1} band is calculated.

First, *in situ* Raman spectra are measured during the second cycle discharge process (Figure 2-23(a)) and their corresponding peak heights of the 145 cm^{-1} mode are correlated with the amount of lithium insertion in the $Li_xV_2O_5$ electrode (Figure 2-23(b)). According to the analysis, the natural logarithm of the peak intensity decreases linearly with the amount of lithium present in the $Li_xV_2O_5$ electrode, which has not been demonstrated before. This correlation has been utilized in order to investigate the impact on the structure of the $Li_xV_2O_5$ when the electrode is cycled at higher C-rates.

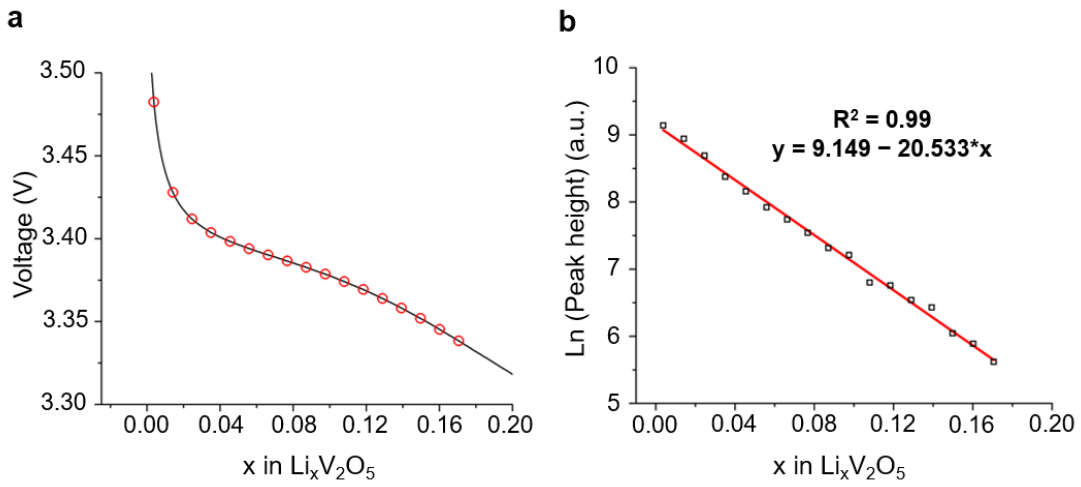

Figure 2-23: (a) Discharge curve of the second cycle; red circles correspond to the point where the *in situ* Raman are analyzed. (b) Correlation between the natural log of the peak height at the 145 cm^{-1} mode as a function of the lithium insertion in $Li_xV_2O_5$ electrode.

When the $Li_xV_2O_5$ electrode is discharged at higher C-rates (C/2, and 1C), the logarithm of the peak height also decreases linearly as a function of the amount of lithium in the electrode (Figure 2-24(b),(c)). However, the slope of the fitted lines changed from −20.53 to −25.80 (Figure 2-24(a),(b),(c)) as the C-rates are increased from C/4 to 1C. This indicates that the level of disorder in the $Li_xV_2O_5$ electrode increases faster when it is discharged at higher C-rates, even when the same amount of lithium is inserted into the electrode. This shows that the level of disorder in the electrode not only depend on the amount of lithium present in the electrode but how fast they are inserted into the electrode. However, when the C-rate is decreased to C/4 again, the slope of the fitted line increased back to −20.16 (Figure 2-24(d)) which is almost identical to the value obtained in Figure 8a. We believe the recovery of the slope from −25.80 (1C) to −20.16 (C/4) corresponds to the fully reversible structural changes

in the $Li_xV_2O_5$ electrode within the voltage range from 3.75 to 2.8 V, experiencing no permanent bond breaking or irreversible loss in the crystallinity [133].

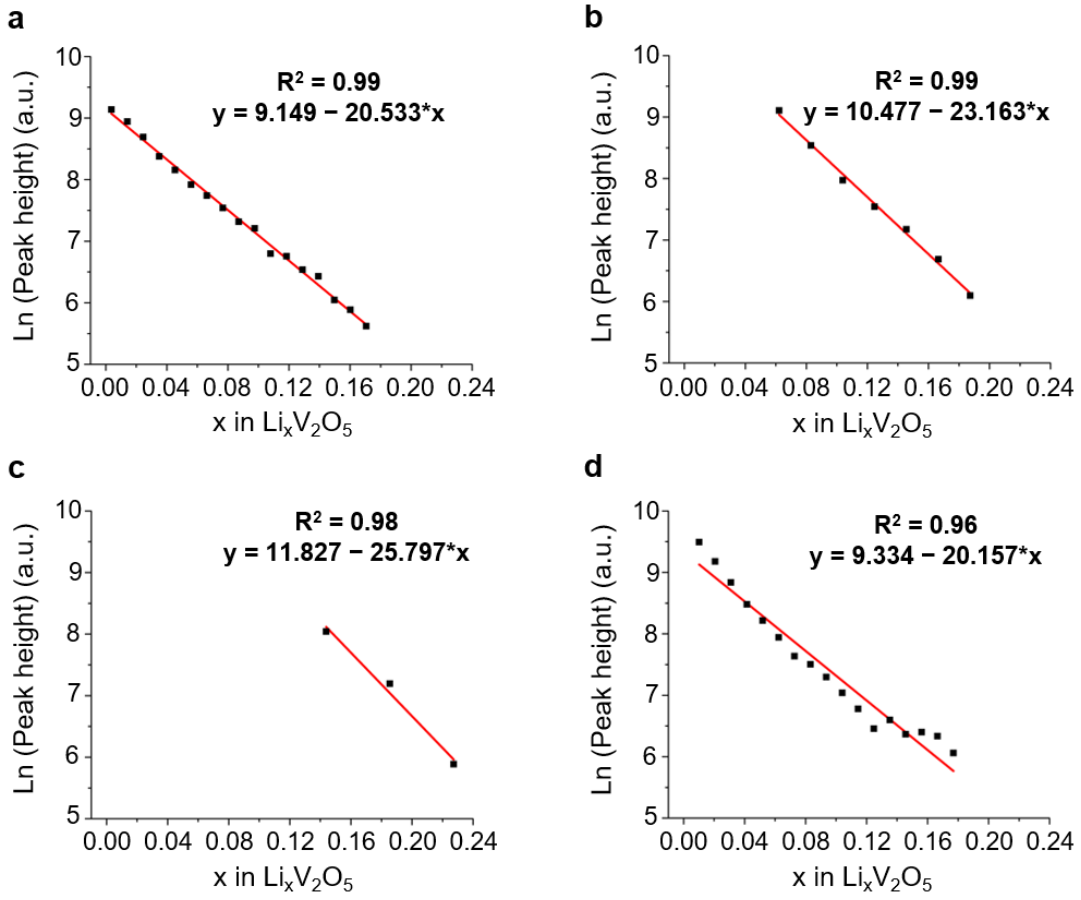

Figure 2-24: Correlation between the natural log of the peak height at the 145 cm^{-1} mode as a function of the lithium insertion in $Li_xV_2O_5$ electrode when discharged at (a) C/4 (2nd cycle), (b) C/2 (4th cycle), (c) 1C (6th cycle), and (d) C/4 (8th cycle).

2.4 Chapter summary

This chapter focuses on the development of the Fabry-Perot MEMS sensor platform. By taking full advantage of the unique design of the Fabry-Perot MEMS sensor and commercially available Raman microspectroscopy measurement setup, the approach allows *in situ* analysis on the qualitative stress changes and characterization

of the microstructural evolutions in different phases of the $Li_xV_2O_5$ electrode. The integrated setup demonstrates a unique advantage in the visualization of the phase evolutions in the $Li_xV_2O_5$ electrode. The stress changes depending on different phases of the electrode are also characterized through analysis of the interference patterns and corresponding structure evolutions are concurrently analyzed using μRaman spectroscopy. Different phases of the $Li_xV_2O_5$ electrode reveal significantly varying stress changes, which are well correlated with the $Li_xV_2O_5$ electrode lattice parameter changes. At the same time, the Raman spectra allow observation of fully reversible structural changes from the α- to δ-phase, irreversible γ-phase with the permanent bond breaking, and weakly crystallized ω-phase.

It has been also shown that the magnitude of the stress changes in the $Li_xV_2O_5$ electrode for different C-rates increase linearly with the amount of lithium present in the electrode, indicating the C-rates do not themselves induce larger intercalation induced stresses. At the same time, inflections in the stress change, which are observed when the $Li_xV_2O_5$ electrode is experiencing α- to ε-phase and ε- to δ-phase transitions, required greater amount of lithium as the electrode is cycled at higher C-rates. This behavior is believed to be caused by the slow lithium-ion diffusion in the $Li_xV_2O_5$ matrix, causing steeper lithium concentration gradients across the $Li_xV_2O_5$ film thickness when it is cycled at higher C-rates. *In situ* Raman spectra accumulated along the discharge processes at different cycles have allowed us to characterize the intensity change at the 145 cm^{-1} mode, an indicator of disorder in the $Li_xV_2O_5$ electrode. A faster increase in the level of disorder within the $Li_xV_2O_5$ electrode has been observed when

it is cycled at higher C-rates. When the C-rate is reduced back down, the evolution of the level of disorder in the $Li_xV_2O_5$ electrode recovers its original trend, indicating that the $Li_xV_2O_5$ electrode experiences fully reversible structure changes when cycled at higher C-rates.

This Fabry-Perot MEMS sensor platform facilitates simultaneous *in situ* investigations of electrochemically-driven stress and microstructural changes in LIB electrodes. The unique can open up new avenues to *in situ* methods for LIB research where most of the *in situ* techniques focus on analyzing either stress or microstructural evolutions in the electrodes. Also, the unique advantage in the visualization of the phase evolutions in the $Li_xV_2O_5$ electrode enables characterization of microstructural change beyond the δ-phases, which has not been demonstrated in the previous *in situ* Raman studies applied to $Li_xV_2O_5$ electrodes.

Chapter 3: Investigation of battery degradation mechanisms using Fabry-Perot MEMS sensor

As previously mentioned in Chapter 1, continuous volume expansion/contraction-induced stress in LIB electrodes gradually deteriorates battery performance. Therefore, considerable efforts have been made to study *in situ* stress evolution. However, stress gradient in the electrode and its effect in the battery performance has largely remained unknown since it can only be studied using finite models or numerical simulations [166]. There is a need for controlling the stress and stress gradient in LIB electrodes and investigating their relationship with battery degradation mechanisms.

This chapter presents the first demonstration of modifying stress and stress gradient in LIB electrodes *via* combining two different crystal phases of an electrode material for investigation of battery degradation mechanisms. The crystal phase-dependent stress changes in V_2O_5 cathodes are characterized *in situ* using the Fabry-Perot MEMS sensor and cycle life test results of the V_2O_5 electrodes are analyzed.

Dr. Chuan-Fu Lin and Ms. Chanyuan Liu contributed to the discussion of the combining two different crystal phases of the V_2O_5 cathode for modifying the stress and stress gradient in the electrode.

3.1 Electrode Design and Experimental Setup

In order to achieve this goal, three different electrodes are prepared and coated on the backside of the membrane for their stress characterization. The

V_2O_5 is chosen as a material of choice to control the stress and stress gradient in the electrode using different crystal phases. TEM images of amorphous V_2O_5 (a-V_2O_5), crystalline V_2O_5 (c-V_2O_5), and stacked V_2O_5 electrodes are shown in Figure 3-1. Compared to a-V_2O_5 (Figure 3-1(a)), c-V_2O_5 (Figure 3-1(b)) shows preferential growth along the (001) direction on an Au layer. The stacked electrode (Figure 3-1(c)) is fabricated by first depositing a-V_2O_5 followed by c-V_2O_5; a sharp boundary is observed between layers in TEM. After electrode deposition, the Fabry-Perot MEMS sensor is packaged in the modified coin cell, connected to a potentiostat, and placed under an optical microscope (Figure 3-2).

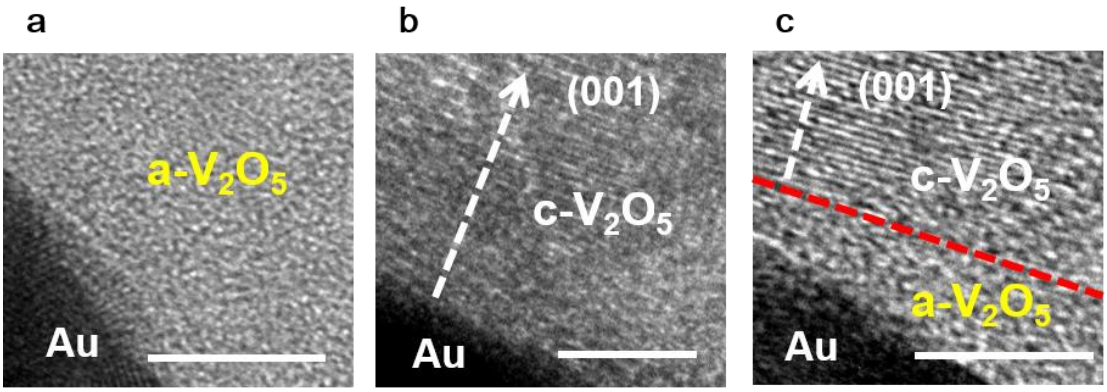

Figure 3-1: TEM of three different V_2O_5 electrodes: (a) amorphous V_2O_5, (b) crystalline V_2O_5, and (c) stacked (amorphous and crystalline) V_2O_5. (Scale bars, 5 nm)

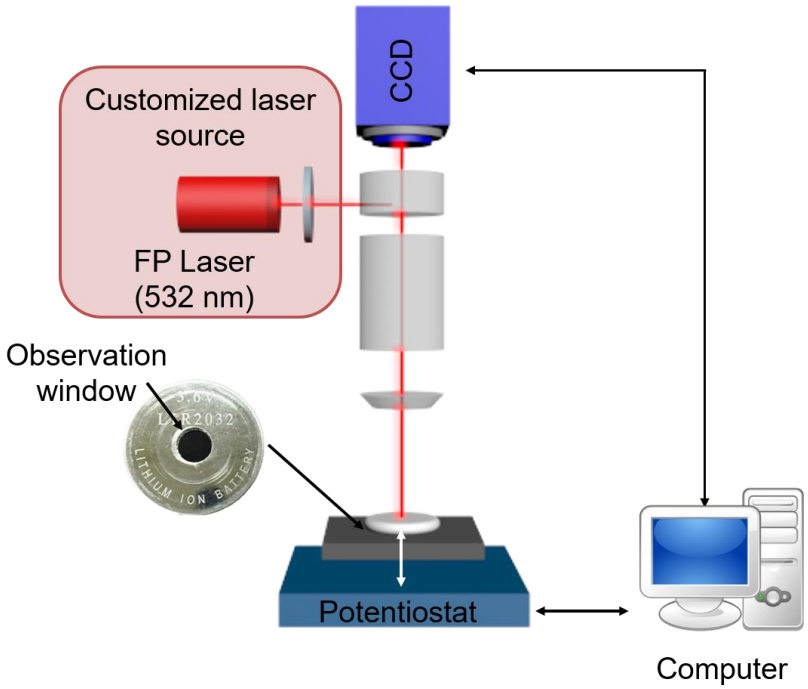

Figure 3-2: Simplified schematic of the experimental setup showing the coin cell under test relative to the optical microscope.

3.2 Experimental results

3.2.1 Stress characterization

Qualitative stress changes in the electrodes are monitored by analyzing the fringe shift of the interference patterns (Figure 3-3(a)), and the results are superimposed on top of the discharge-charge curves (Figure 3-3(b),(c)). Upon lithium insertion, the a-V_2O_5 electrode experiences increasing compressive stress Figure 3-3(b), fringe shift +3) due to the isotropic volume expansion during lithium insertion [159]. On the other hand, the c-V_2O_5 shows the increasing tensile stress (Figure 3-3(c), fringe shift −20) which corresponds to the previous results (2.3.1.2 *In situ* analysis of qualitative stress).

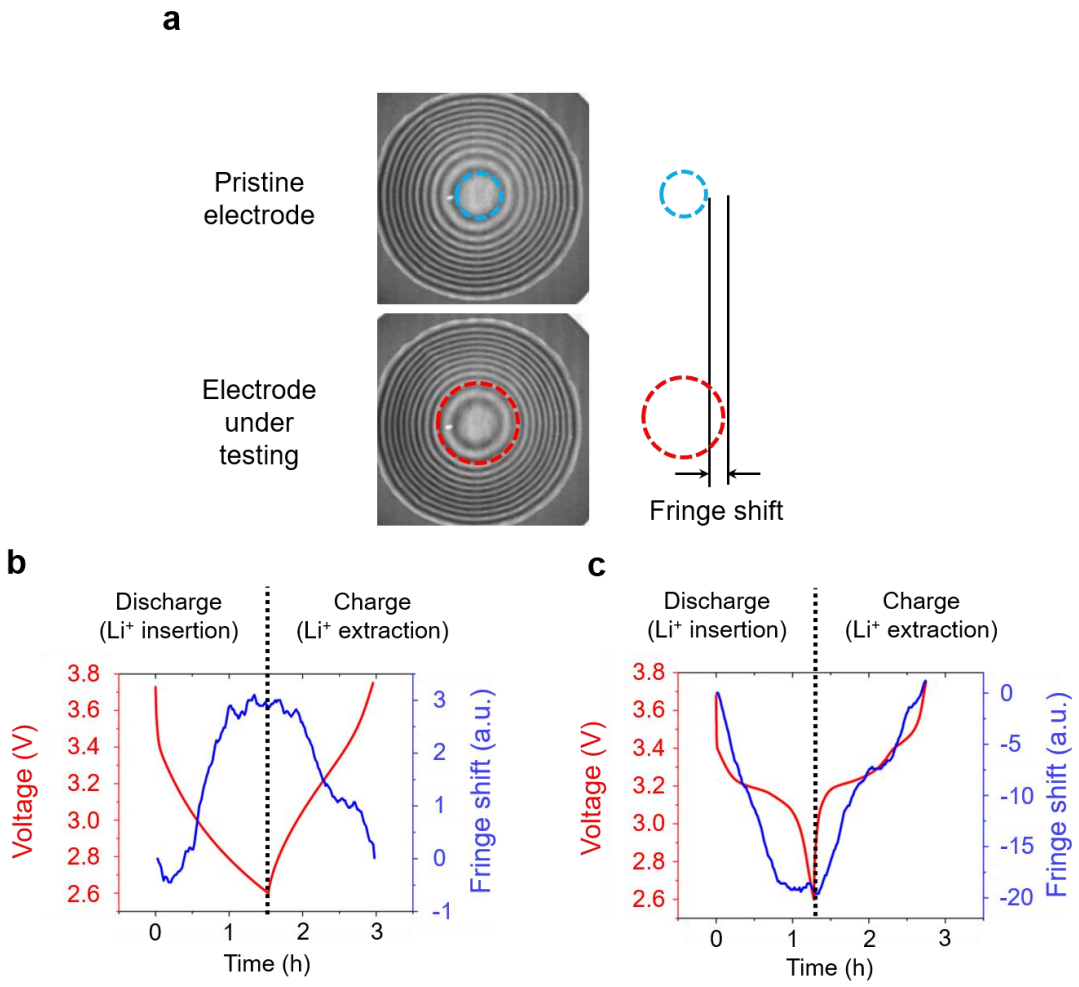

Figure 3-3: (a) Photographs of the experimentally obtained fringe patterns, showing relative fringe radius change. Correlation between the fringe shift and discharge-charge curve of the (b) a-V_2O_5, (c) c-V_2O_5, and (d) stacked V_2O_5.

3.2.2 Modification of stress in V_2O_5 electrode

The stacked electrode (Figure 3-1(c)) undergoes both tensile and compressive stress changes due to the contributions from the c-V_2O_5 and a-V_2O_5 phases, respectively (Figure 3-4). Stress compensation of the alternately stressed layers significantly reduces the fringe shift magnitude (~ 4) and less compressive stress is induced (~ 1.5) in the stacked electrode compared to the c-V_2O_5 and a-

V_2O_5 electrodes, respectively. This result indicates that the stress in the electrode can be modified by stacking alternately stressed layers.

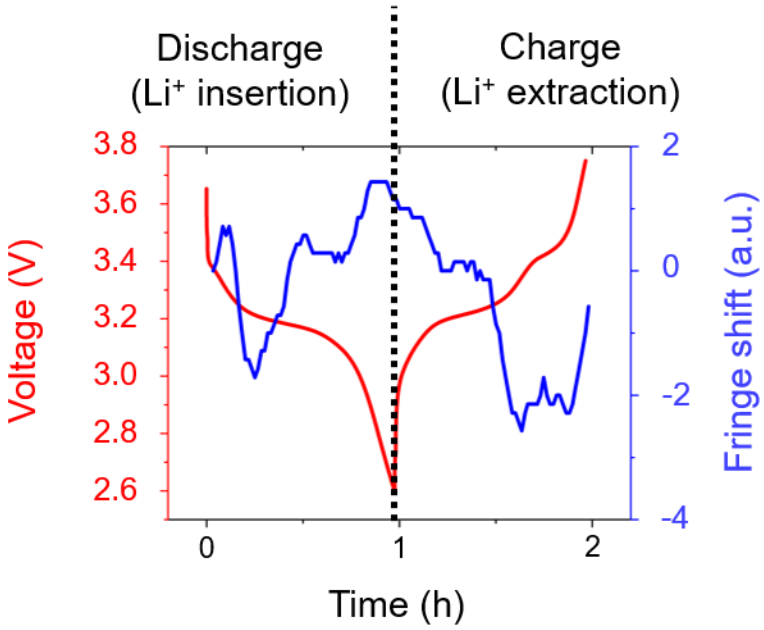

Figure 3-4: Correlation between the fringe shift and discharge-charge curve of the stacked V_2O_5.

3.2.3 Cycle life test of V_2O_5 electrodes

In order to examine how the performance of the stacked electrode, cycle life tests are performed and compared to the c-V_2O_5. Figure 3-5 presents the capacity changes of the first 2000 cycles for the crystalline and stacked electrodes. The c-V_2O_5 electrodes retain ~ 91% of their maximum capacity (Figure 3-5a), while the stacked electrodes retain only ~ 83% (Figure 3-5b). We believe this faster degradation in the stacked electrodes is due to the high stress gradient at the boundary of the layers in spite of the reduced stress, and therefore the results illuminate the importance of the stress gradient within the electrode.

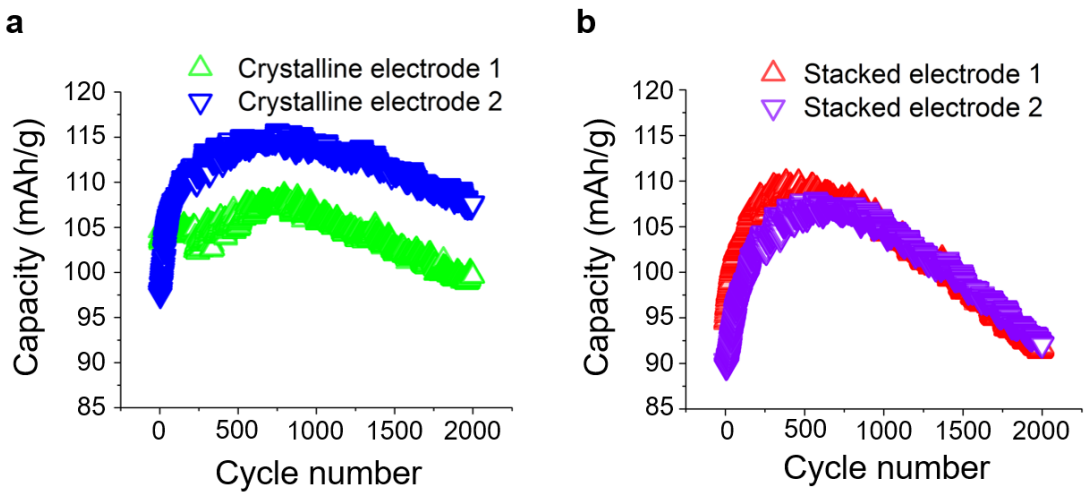

Figure 3-5: Capacity change *vs.* cycle number for (a) crystalline electrodes and (b) stacked electrodes at 5C.

3.4 Chapter summary

The work presented in this chapter demonstrates a unique of way controlling electrochemically-driven stress and stress gradient in LIB electrodes using the alternatively varying stressed layers. Electrochemically induced stress change during battery operation in the a-V_2O_5, c-V_2O_5 and stacked V_2O_5 electrodes are characterized *in situ* using the Fabry-Perot MEMS sensor. Due to the contributions from the c-V_2O_5 and a-V_2O_5 phases, the stacked electrode experiences both the tensile and compressive stress changes, respectively. At the same time, the overall fringe shift magnitude is greatly reduced due to stress compensation of the alternately stressed layers. However, the stacked electrode shows faster capacity loss, due to the high stress gradient at the boundary of the layers in spite of the reduced stress.

This method provides a unique opportunity of exploring effects of the stress and stress gradient on LIB battery performance which have not been achievable previously, and therefore the results illuminate the importance of the stress gradient within the electrode. Previously, surface coatings (passivation layers) have been shown to be an effective approach to mitigate the mechanical degradation in thin film electrodes induced from the stress, improving cycling behavior. However, these coating layers do not participate in the electrochemical reaction and increase dead mass, reducing the specific capacity of the electrodes. Therefore, the approach presented in this work, which utilizes combining two different crystal phases of an electrode material, can be an alternative solution to reduce the degradation in the electrodes without adding the dead mass in the electrodes.

Chapter 4: Design and fabrication of buckled membrane MEMS Sensor

The Fabry-Perot MEMS sensor integrated with different types of scientific equipment (such as Raman spectrometers) demonstrates many advantages compared to other *in situ* techniques. However, observed stress changes remain qualitative due to the following reasons. First, the deflection of the membrane cannot be measured accurately. It is only possible to measure the approximate membrane deflection by counting the number circular rings in the fringe pattern. Nevertheless, due to the wavelength limitation of the laser source (532 nm), the resolution of the measurement is limited to half of the wavelength (266 nm) which is too low to correctly quantify the membrane deflection. Lastly, the fabrication process limits characterization of the residual stress value of the membrane. It is critical to correctly characterize the residual stress of the membrane since the deflection changes correspond to this residual stress value. However, the anodic bonding process, which requires high vacuum and temperatures to form the optical cavity, induces additional stress in the membrane that cannot be easily quantified. Not being able to achieve quantitative stress analysis prevents further investigations such as fracture energy [14] or stress-potential coupling [6] of the lithiated electrode, which can only be deduced from measuring stress changes in the electrode quantitatively.

In order to address this limitation, a buckled membrane MEMS sensor is designed which allows quantifying the stress change in Li-ion battery electrode

during battery operation, while characterizing the microstructural changes at the same time. The sensor is designed based upon the analytical calculations from membrane theory and its results are compared to the finite element analysis simulation results for verification. The multilayer membrane structure is also taken into account for the design of the sensor. Evidence of the bi-stable buckled membrane is observed and the buckling height of the fabricated membranes correspond well with the calculation and simulation results.

Dr. Konstantinos Gerasopoulos contributed to the discussion of designing the buckled MEMS sensor.

4.1 Buckled membrane MEMS sensor design

The buckled membrane MEMS sensor is designed based on equation (11) that is explained in Chapter 1, which describes the relationship between the residual stress and the buckling height of the membrane. Plasma enhanced chemical vapor deposition (PECVD) SiO_2 and Si_3N_4 are selected as structural layers of the membrane. The PECVD SiO_2 layer has a compressive residual stress (-157.9 MPa), which induces buckling of the membrane when it is released from Si substrate. On the other hand, the PECVD Si_3N_4 layer that has a residual tensile stress (231.7 MPa) is added on top of the SiO_2 layer in order to avoid an asymmetric wrinkled membrane [167]. The membrane is required to be designed such that it is sensitive enough to measure the change in buckling height changes induced by the electrode and mechanically robust enough to endure battery assembly and atomic force microscopy (AFM) measurements. Therefore, it is

important to precisely decide the thickness of the structural layers. If the structural layer is too thick, the membrane will provide enough mechanical robustness but will not be sensitive enough to measure the stress changes in the electrode.

During battery operation, the membrane needs to exhibit a continuous buckling height change in order to analyze how the stress evolves in the electrode. However, the stress change in the V_2O_5 electrode has not been reported in literature, which requires an assumption in order to predict how much the stress changes in the V_2O_5 electrode based on a reported electrode stress change in literature. It is reported that the Si electrode experiences a stress change from −1.7 GPa to 1.7 GPa induced by ~300% volume change [8]. Therefore, the V_2O_5 stress change is expected to be much less compared to the Si electrode since V_2O_5 experiences ~25% volume change during lithium cycling [168]. The anticipated V_2O_5 stress change is set to be –1 GPa to 1 GPa, which is higher than expected, in order to prevent the buckled membrane from changing its buckling status from buckled down to buckled up or vice versa during electrochemical cycling.

The buckling height change (100 μm in diameter) as a function of V_2O_5 stress change is shown in Figure 4-1. The buckling height change is achieved from analytical calculation and COMSOL simulation. In the analytical calculation, the effective stress and the flexural rigidity of the membrane are

estimated first using equation (6) and (9). Parameters that are used for the calculation are listed in Table 4.

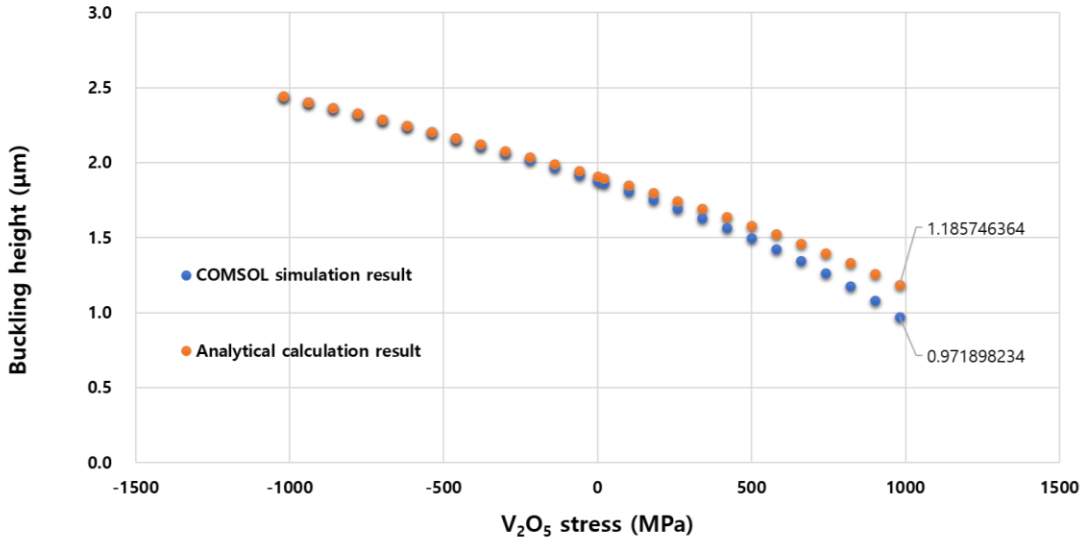

Figure 4-1: Buckling height of the MEMS sensor achieved from the COMSOL simulation (in blue) and analytical calculation (in orange) as a function of the V_2O_5 stress.

Once the effective stress and the flexural rigidity are achieved, the buckling height change according to the V_2O_5 stress change (−1 GPa to 1 GPa) is calculated from equation (11) using MATLAB. For the COMSOL simulation, a circular membrane with clamped edges is drawn (Figure 4-2(a)) first using the same parameters listed in Table 4. The buckling height change is simulated using Solid Mechanics physics, which is supported by COMSOL, according to the same V_2O_5 stress change (−1 GPa to 1 GPa) (Figure 4-2(b)) using a parametric sweep. According to the analytical calculation and the COMSOL simulation results, the buckling height of the membrane changes from 2.44 μm to 1.19 μm and 2.44 μm to 0.97 μm, respectively. The results show that the analytical

calculation and the COMSOL simulation results match well, demonstrating the feasibility of using the membrane theory for quantifying the stress change in Li-ion battery electrode.

Table 4: Parameters that are used for the analytical calculation and the COMSOL simulation

Structure	Material	Thickness	Young's modulus	Poisson's ratio	Residual stress
Layer 1	Si_3N_4	100 nm	250 GPa [169]	0.253 [169]	231.7 MPa
Layer 2	SiO_2	650 nm	70 GPa [169]	0.20 [169]	−157.9 MPa
Layer 3	V_2O_5	40 nm	129.2 GPa [170]	0.25 [170]	−1.0 to 1.0 GPa

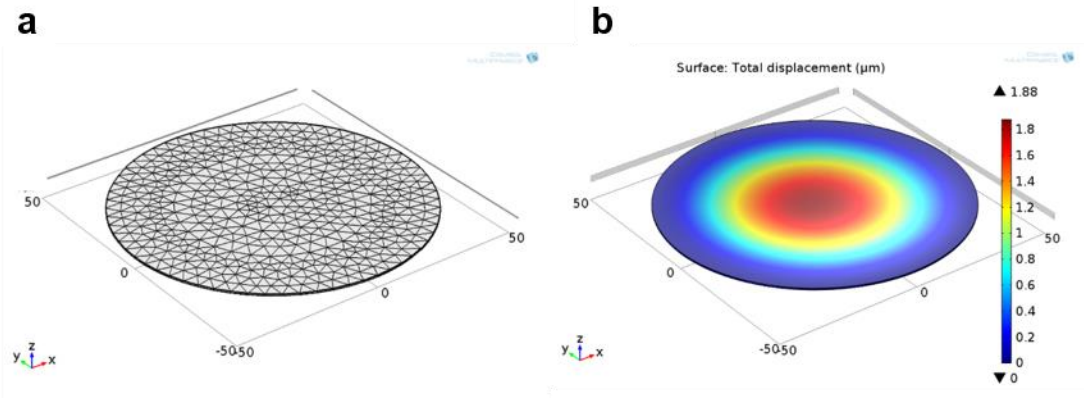

Figure 4-2: Images achieved from COMSOL (a) drawing of the 100 um wide clamped membrane and (b) simulated result of the buckled membrane showing 1.88 um deflection.

4.2 Fabrication results

The MEMS sensor device is fabricated in the MEMS Sensors and Actuators Laboratory and University of Maryland's FabLab. The starting

material is a 4 inch Si (100) wafer (Figure 4-3(a)) as a substrate. First, 12μm deep alignment marks for the atomic force microscope scanning process are formed by deep reactive ion etching (DRIE) on one side of a Si wafer (Figure 4-3(b)-(c)). A 500 nm thick layer of SiO_2 is deposited followed by a 50 nm Si_3N_4 layer on one side using plasma enhanced chemical vapor deposition (PECVD) (Figure 4-3(d)). The Si_3N_4 is used to control the residual stress of the membrane in order to prevent higher order buckling [167], while the SiO_2 serves as both the membrane and an etch stop layer for the second DRIE on the 'battery' side of the wafer (from the bottom). The battery cavities are defined on the 'battery' side of the wafer using photoresist (Figure 4-3(e)) and fabricated by successive etching of Si (DRIE) (Figure 4-3(f)). After the fabrication process, the wafer is diced into individual 1 cm × 1 cm chips. SiO_2, Cr/Au and V_2O_5 thin films are deposited inside the battery cavities to form the passivation, current collector and electrode layers, respectively. When combined with a Li-conducting electrolyte and metallic Li as a counter electrode in a coin cell package, the 'battery' side of the device forms a Li-ion battery system.

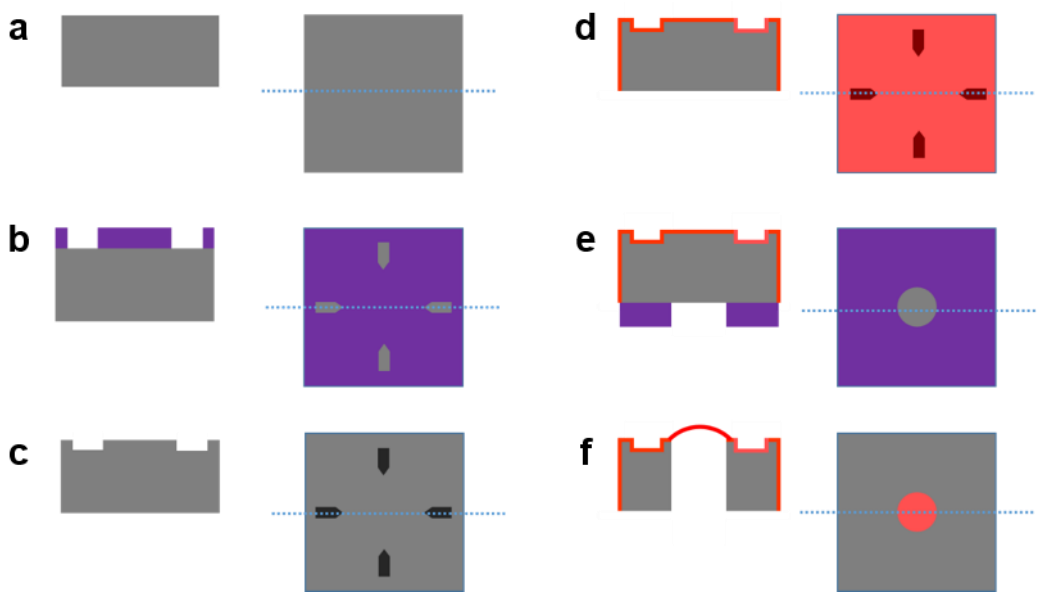

Figure 4-3: MEMS membrane sensor fabrication process showing (a) substrate, (b) photoresist etch mask, (c) DRIE, (d) PECVD Si_3N_4/SiO_2, (e) photoresist mask for backside etch and (f) DRIE to release the membrane.

The fabrication process requires two masks as shown in Figure 4-4. The first mask is used for etching the membrane location indicators on the front side of the Si substrate using DRIE. The indicators are necessary in order to locate the membrane easily during AFM measurements. The second mask determines the membrane diameters (100, 110 and 120 μm) and location on the backside of the Si substrate. The membrane is released using DRIE and SEM images of the fabricated membranes are shown in Figure 4-5.

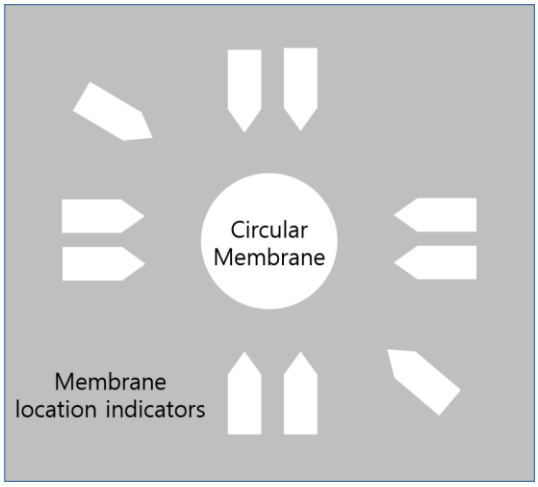

Figure 4-4: Schematic of the buckled MEMS sensor mask design.

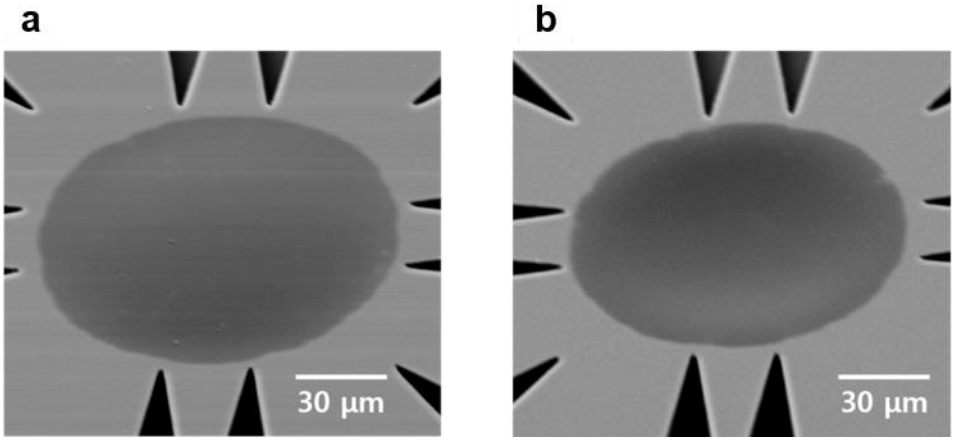

Figure 4-5: SEM images of the 120 µm wide (a) buckled up and (b) buckled down membranes.

The membrane can either buckle up or down since it has the bi-stable state as explained in 1.3.3.1 Membrane buckling. Evidence of the bi-stable buckled membrane is also observed in the fabricated membranes as shown in Figure 4-5. Notwithstanding the buckling height of the membrane being less than 2.5 µm,

there are distinctive differences between the buckled up and down membranes in the SEM images.

4.3 Chapter summary

The study in this chapter focused on designing and fabricating the buckled membrane MEMS sensor based on the membrane theory. The buckled membrane has been adopted for designing the MEMS sensor in order to utilize the ability to translate small in-plane strain into relatively large vertical displacement. The multilayer membrane structure is required in order to perform electrochemical tests as a LIB. Therefore, the effective residual stress and effective flexural rigidity of the multilayer membrane are utilized in the design of the sensor.

After fabricating the buckled membrane MEMS sensor, buckling heights of the MEMS sensor membranes with different diameters (100, 110 and 120 μm) are measured using the AFM. The buckling heights exhibit good agreement with the analytical calculation and the simulation results, which shows the feasibility of the approach for quantifying the stress changes in LIB electrodes.

Chapter 5: *In Situ* Study of V_2O_5 Electrode using buckled membrane MEMS sensor platform

This chapter discusses an integration of the buckled membrane MEMS sensor with advanced microscopy/spectroscopy instrumentation for quantitative stress characterization and microstructural analysis, highlighting the potential of MEMS as enabling tools for advanced scientific investigations of thin film Li-ion battery electrodes.

Dr. Chuan-Fu Lin contributed to designing the buckled membrane MEMS sensor platform and executing experiments.

5.1 Experimental setup

5.1.1 AFM Measurement

Buckling heights of the fabricated MEMS sensor membranes with different diameters (100, 110 and 120 μm) are measured using the AFM (NTEGRA Spectra, NT-MDT), which is shown in Figure 5-1. The equipment is capable of executing sequential AFM and confocal Raman spectroscopy measurements (Figure 5-2).

Figure 5-1: Optical image of the NTEGRA Spectra.

The diced chip (1 cm × 1 cm) containing one buckled membrane MEMS sensor is placed on top of the XYZ scanner stage (Figure 5-2), which is driven by a piezoceramic material. Once the AFM measurement starts, the XYZ scanner stage scans the entire buckled membrane area (120 μm × 120 μm) using tapping mode. The scanning result of the 120 μm wide buckled membrane is shown in Figure 5-3. The AFM measurement results for different membrane diameters are compared with the analytical calculation results (equation (11)) and the COMSOL simulation results (Figure 5-4). The buckling heights exhibit good agreement with the analytical calculation and the simulation results, which shows the feasibility of the approach for quantifying the stress changes in Li-ion battery electrodes.

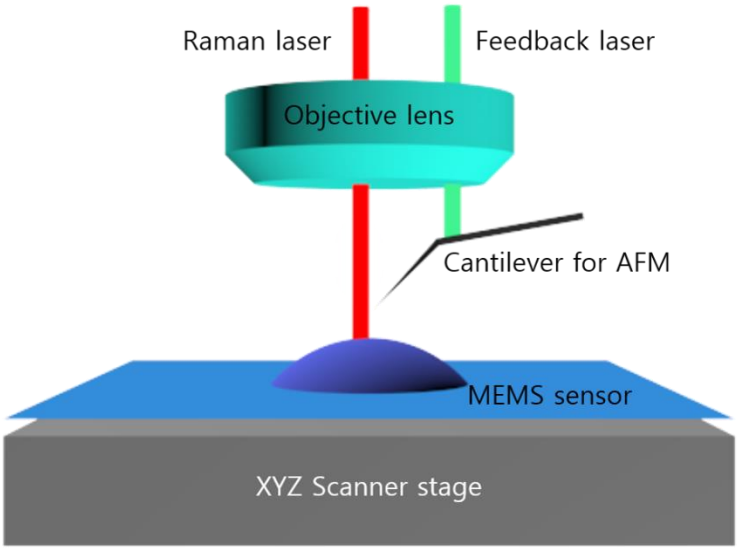

Figure 5-2: Close-up view of the MEMS sensor which is placed on the XYZ scanner stage and under the objective lens for the AFM and Raman spectroscopy measurement, respectively.

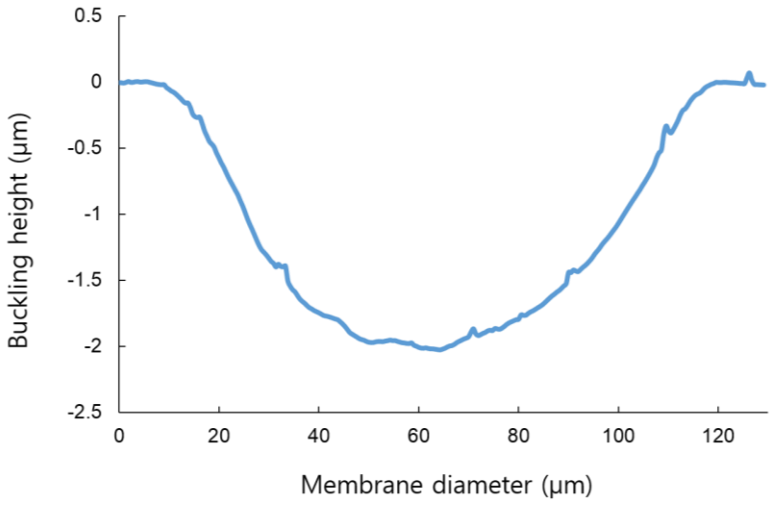

Figure 5-3: AFM scanning profile of the 120 um wide buckled membrane.

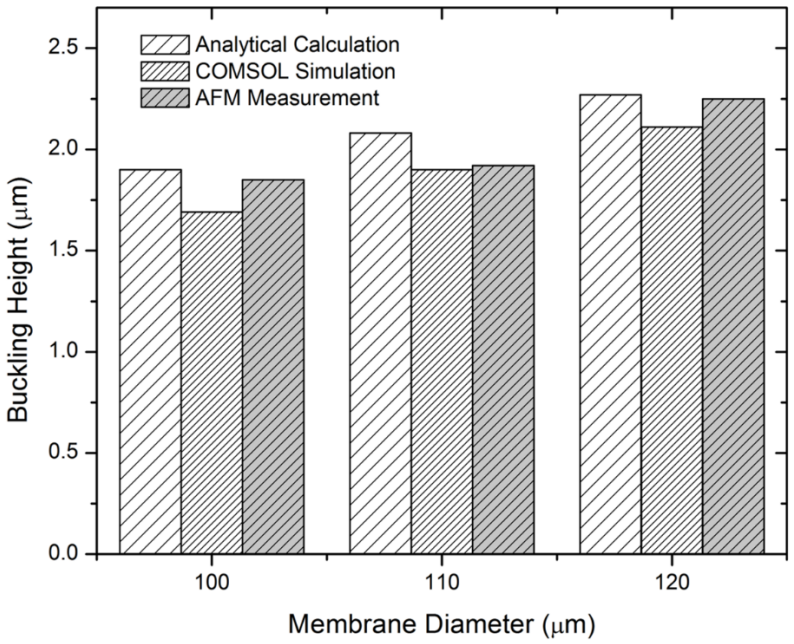

Figure 5-4: Buckling height data for three membranes with different diameters obtained using analytical calculations, COMSOL simulation and AFM measurement.

5.1.2 Raman spectroscopy measurement

Microstructural changes of the electrode during battery operation have been analyzed using Raman spectroscopy measurements. However, the V_2O_5 electrode is placed underneath the structural layers (100 nm Si_3N_4 and 650 nm SiO_2) and the current collector (10 nm Cr and 15 nm Au), which has been discussed in 1.3.3.1 Membrane structure. Therefore, it is important to verify whether the electrode can still be probed through the different layers using Raman spectroscopy. Figure 5-5 shows a comparison between the Raman spectrum of sputtered V_2O_5 from literature and ALD deposited V_2O_5 from an actual measurement using the platform (Figure 5-1). Crystalline V_2O_5 is known to have nine different Raman peaks and their corresponding peak positions are

labeled in Figure 5-5(a) [3]. The same Raman peaks are also observed in the ALD deposited V_2O_5 probed using the measurement setup Figure 5-5(b), which demonstrates that excitation with a 632 nm radiation for analysis using the Raman spectroscopy is capable of accessing the electrode underneath the different layers.

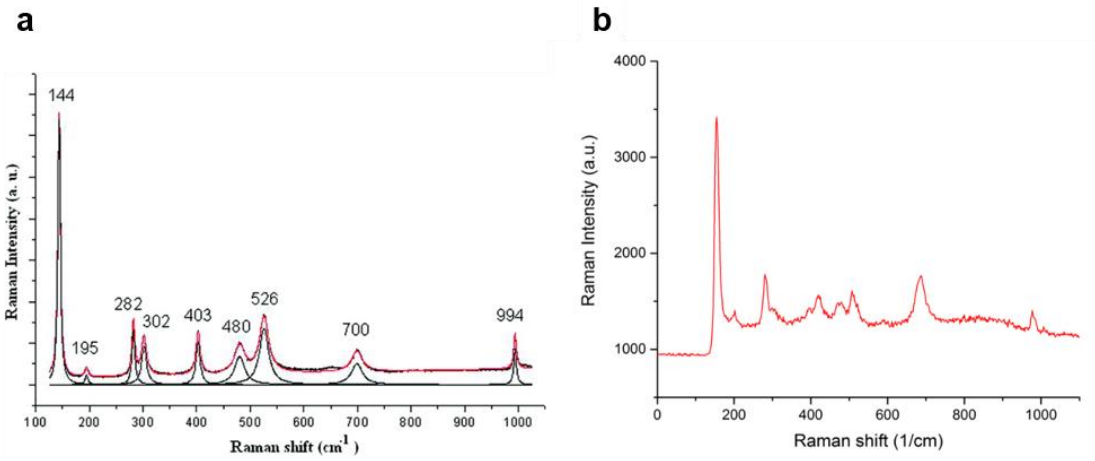

Figure 5-5: Raman spectrum of (a) sputtered V_2O_5 and (b) ALD V_2O_5.

5.2 Packaging

New packaging is devised to facilitate the experiment using the AFM and the Raman spectroscopy measurements during battery operation. Due to the hermetic sealing requirements for proper Li-ion battery operation, a new custom-made electrochemical cell packaging scheme has been created. The new packaging scheme modified the existing packaging scheme, which has been already demonstrated and verified from the previous work reported from our group [13].

A perspective view of the cell that has been developed for packaging the buckled membrane MEMS sensor is shown in Figure 5-6. A standard coin cell is modified with an opening (7 mm in diameter) to enable AFM and Raman spectroscopy measurements. Lithium foil is used as the counter electrode and an organic electrolyte fills the entire coin cell base. A polymer separator is used to prevent direct contact of the Lithium foil with the working electrode. The MEMS device then be placed on top, with the through-hole cavity facing the separator. Aluminum foil with conductive adhesive tape (1179 tape, 3M) is used to interface the device to the conductive top coin cell manifold.

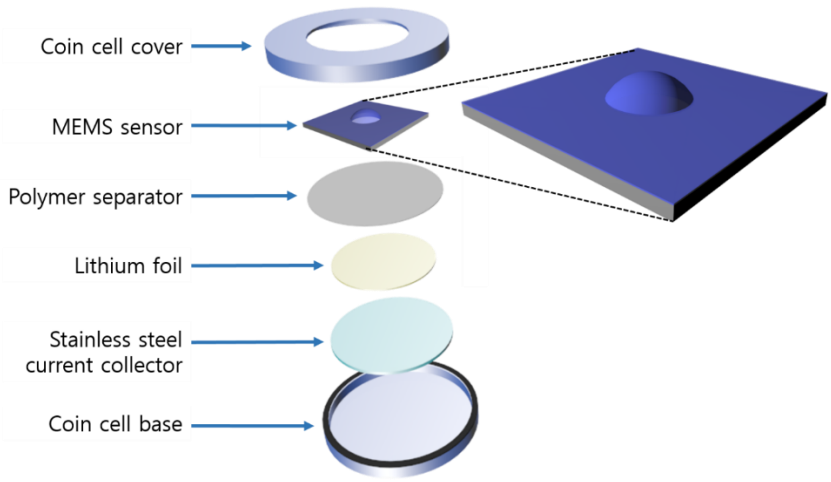

Figure 5-6: Perspective view of the electrochemical cell that has been developed for this work: a standard coin cell is modified with an optical window to give access to AFM and Raman spectroscopy measurements. Lithium foil is used as the counter electrode and a polymer separator is used to facilitate proper wetting with the liquid electrolyte. The MEMS sensor is connected to the coin cell cover with conductive tape.

In the new packaging scheme, the wider opening is created compared to the previous packaging scheme (5 mm) and the thinner conductive tape are used

in order to help the AFM tip to reach the membrane (Figure 5-7). The electrochemical cell is assembled in a glove box; however, the new packaging scheme permits reliable and robust operation in ambient atmosphere. The new packaging scheme is an important enabling factor which allows *in situ* measurements of both AFM and Raman spectroscopy in ambient atmosphere.

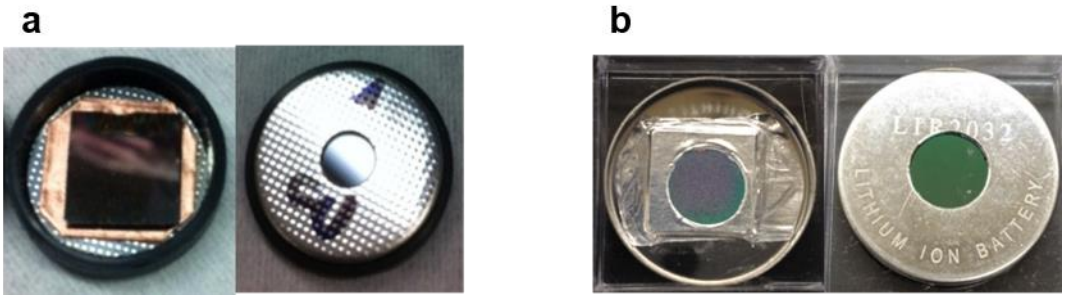

Figure 5-7: Optical image of the (a) previous packaging scheme and (b) new packaging scheme with wider opening and thinner aluminum adhesive tape.

5.3 Experimental results

The buckled membrane MEMS sensor which is packaged in the customized coin cell (Figure 5-7(b)) is connected to a potentiostat (Compactstat.e, Ivium Technologies) and placed under an NTEGRA Spectra microscope as shown in Figure 5-8. A galvanostatic lithium cycling is conducted using the potentiostat in the voltage range of 2.8V - 3.5V with a current density of 350 nA/cm^2. All experiments are conducted in air under normal ambient conditions and both AFM and Raman measurements are taken sequentially during testing.

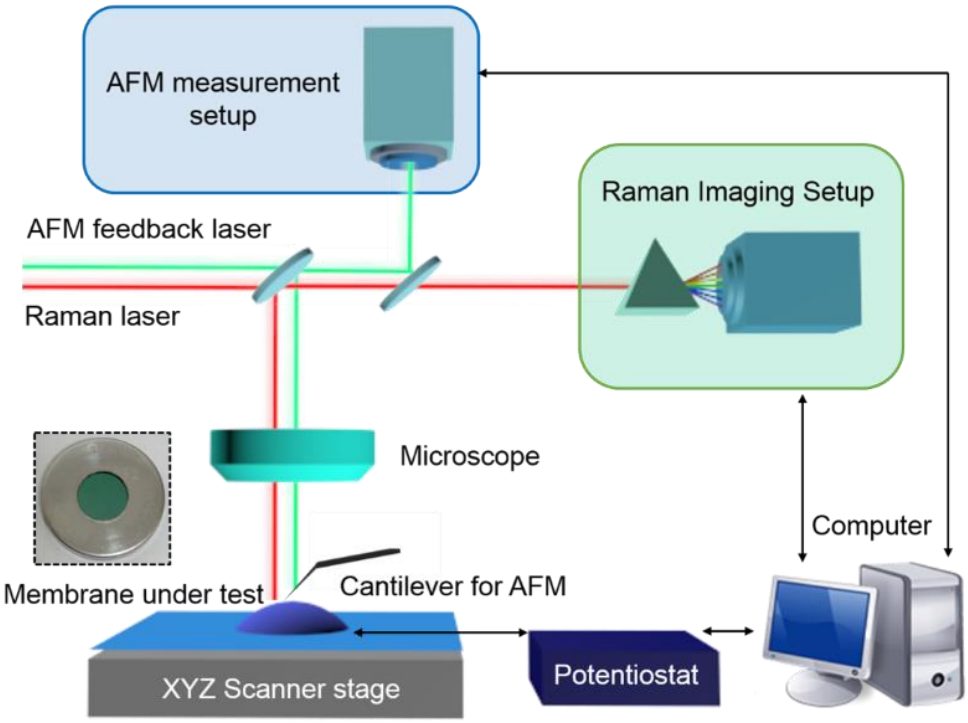

Figure 5-8: Simplified diagrams of the experimental setup and a photograph of the modified coin cell.

The buckling height changes, which are measured using the AFM, are used to quantify the V_2O_5 stress change using the equations discussed in Chapter 4. First, the effective stresses of the membrane at different time points are calculated back from equation (11) by inserting the measured buckling height values. As a result, the effective stress values of the membrane are achieved. The stress values for the V_2O_5 are then calculated from equation (6) and previously measured stress values for other films. Initial stress of the V_2O_5 is calculated from the buckled height of the membrane, which is measured before the electrochemical test. The differential stress values, which are show in Figure 5-9(a), are calculated by subtracting the initial stress values from the V_2O_5 stress

values. Upon lithium insertion (discharge), V_2O_5 contracts and the tensile stress in the V_2O_5 increases gradually until the ε- to δ-phase transition occurs. The lattice constant *a*, which is parallel to the plane direction, elongates in the ε- to δ-phase transition and induces a lower tensile stress as observed in Figure 5-9(a). During lithium extraction (charge), the electrode recovers its initial stress.

Simultaneously, *in situ* Raman spectra are collected and representative data at various points along the discharge/charge curve (black circles in Figure 5-9(a)) are plotted in Figure 5-9(b). The Raman intensity change at 148 cm^{-1} (V_2O_5 layer order/disorder peak) shows that the level of disorder increases during lithium insertion as observed by the disappearance of the peak as shown in Figure 5-9(b). Similarly, the Raman intensity at 148 cm^{-1} progressively recovers as the V_2O_5 lattice structure during lithium extraction becomes more ordered. This can be observed as the re-appearance of the peak at 148 cm^{-1} as seen in Figure 5-9(b).

The results are in good agreement with the expected mechanical behavior and disorder changes in V_2O_5, which is the first demonstration of *in situ* analysis of the quantitative stress and the microstructural changes during battery operation.

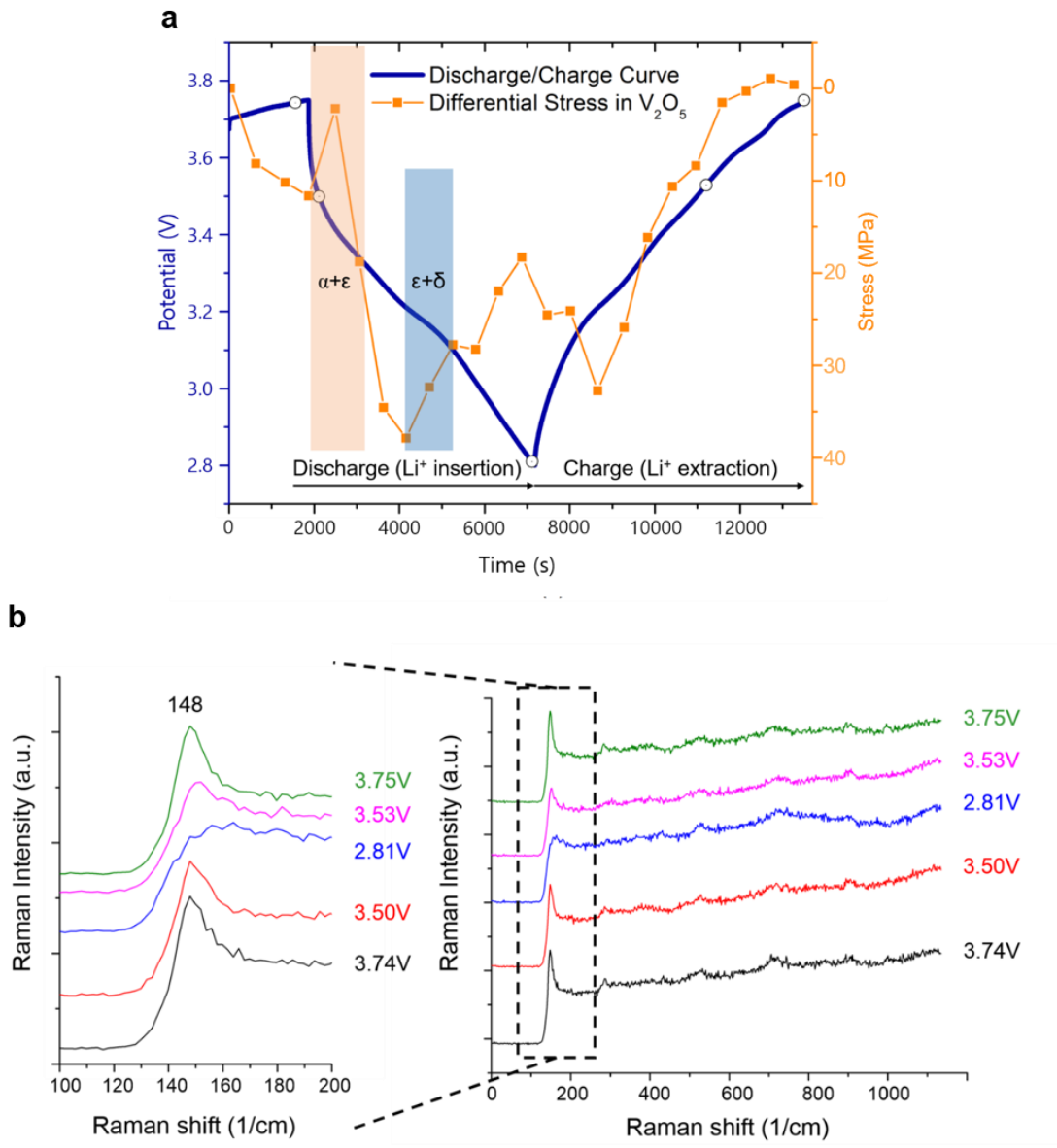

Figure 5-9: (a) Discharge/charge and stress vs. time graphs, (b) *in situ* Raman spectra series at various potentials along the discharge/charge curve (black circles), highlighting the 148 cm^{-1} peak.

5.4 Chapter summary

By integrating the buckled membrane MEMS sensor with the equipment capable of executing sequential AFM and confocal Raman spectroscopy

measurements, a multi-modal *in situ* characterization platform for simultaneous characterization of stress and microstructure evolutions in LIB electrodes is developed. The thin buckled membrane is coated with V_2O_5 cathode on the backside and enables the AFM and Raman spectroscopy from the topside. Using dual-mode measurements, both the induced stress and Raman intensity changes due to lithium cycling are observed during the α- to δ-phase transitions. Results are in good agreement with the expected mechanical behavior and disorder change in V_2O_5 electrode. Additionally, the buckled membrane MEMS sensor platform addresses the qualitative stress analysis limitation of the Fabry-Perot MEMS sensor platform, enabling further investigations of important parameters affecting battery performance (*e.g.* biaxial modulus and fracture energy), which can only be deduced from measuring stress changes in the electrode quantitatively.

The buckled membrane MEMS sensor platform can also be utilized in studying phase dependent stress-potential coupling. The stress-potential coupling has been studied in order to measure loss of the battery efficiency. As previously shown, the coexistence of two distinct phases induces abnormal stress changes in the electrode. Also, the phase transformation from the γ- to ω-phase causes dramatic stress change in the electrode, but its influence on the electric potential due to specific phase transitions/transformations has not been investigated yet. Therefore, the buckled membrane MEMS sensor platform can

be utilized in unraveling the LIB degradation mechanisms and further improving the LIB performance.

Compared to the Fabry-Perot MEMS sensor platform, the buckled membrane MEMS sensor platform has a disadvantage in taking the AFM and Raman spectroscopy measurements due to the equipment capability. The feedback laser for AFM measurement and excitation laser for Raman spectroscopy measurement are guided using the same microscope. This indicates the focal plane of the two lasers should always be the same. However, in order to achieve the highest quality measurement results, the feedback laser for AFM and excitation laser for Raman spectroscopy measurement should be focused on top of the AFM cantilever and the surface of the buckled MEMS sensor membrane, respectively. Hence, currently, the focal plane of the laser is manually changed during measurements in order to achieve the highest quality measurements.

Chapter 6: Concluding Remarks

6.1 Summary

A set of new *in situ* characterization platforms have been designed specifically to aid investigations of LIB electrodes. Many types of *in situ* methods and analysis techniques exist and are widely employed in terms of characterizing stress and microstructural evolutions in the electrodes, and each presents a set of advantages and limitations for LIB research. The platforms created in this work combine the benefits of separate technologies by utilizing MEMS technology to address challenges in the current technology. The MEMS sensors are designed and integrated with scientific equipment to enable *in situ* characterization of stress and microstructural changes in LIB electrode, which has been mainly limited to providing either the stress or microstructural changes for battery research.

The Fabry-Perot MEMS sensor platform developed in this work addresses a need for development of techniques which are capable of capturing in real time the microstructural changes and the associated stress during battery operation, which is crucial for unraveling the LIB degradation mechanisms and further improving the LIB performance. This is accomplished by integrating the Fabry-Perot MEMS sensor with a commercially available Raman microscope which allows simultaneous measurement of microstructural changes using μRaman spectroscopy in parallel with qualitative stress changes *via* optical interferometry. This is the first time such a characterization tool integration has been

accomplished. Characterization of the evolution in microstructure and stress in various crystal phases in the $Li_xV_2O_5$ electrode is achieved, including both reversible and irreversible phase transitions. Also the integrated platform demonstrates a unique advantage in the visualization of the phase transitions and transformations in the electrode, including the pronounced puckering in the V_2O_5 electrode structure and the dramatic change when the electrode is transformed from γ- to ω-phase. The microstructural evolutions in the electrode are analyzed using μRaman spectroscopy and corresponding stress changes depending on different phases of the electrode are concurrently characterized by analyzing the interference patterns of the Fabry-Perot MEMS sensor membrane. Also, previously hypothesized origins of the Raman shifts in certain Raman active modes are confirmed by correlating the spectral shifts with the changes in the electrode stress. Additionally, the Fabry-Perot MEMS sensor platform has been utilized to analyze effects of varying C-rates on the microstructure of and stress in V_2O_5 thin film cathodes. The abrupt changes at certain crystal phase transitions in the $Li_xV_2O_5$ electrode are observed, and the magnitude of the stress changes with the amount of lithium inserted into the electrode are correlated. Simultaneously, a faster increase of disorder within the $Li_xV_2O_5$ layers is observed when the electrode is cycled at higher C-rates.

The Fabry-Perot MEMS sensor has been also utilized to demonstrate stress and stress gradient in LIB electrode can be altered by combining two different crystal phases of an electrode material. This approach presents a unique

technique for controlling the stress and stress gradient in the electrode for investigation of battery degradation mechanisms, which have been studied mainly using finite models or numerical simulations. By stacking alternately stressed layers, the average stress in the electrode is greatly reduced by 75% while a high stress gradient is induced at the boundary of the layers. The crystalline V_2O_5 electrodes retain ~ 91% of their maximum capacity, while the stacked electrodes retain only ~ 83%. This faster degradation in the stacked electrodes is due to the high stress gradient at the boundary of the layers in spite of the reduced stress, and therefore the results illuminate the importance of the stress gradient within the electrode.

The second platform developed in this work addresses the limitation of the Fabry-Perot MEMS sensor platform, which is the qualitative stress characterization, by utilizing the buckled membrane MEMS sensor. The sensor is developed and integrated with equipment capable of performing AFM and Raman spectroscopy measurements in a unified setup. The buckling height changes are measured using AFM, enabling quantification of the stress changes in the electrode. At the same time, Raman spectroscopy is utilized to probe the electrode in order to examine the microstructural changes during battery operation. Thus, the buckled membrane MEMS sensor platform demonstrates a new technique which can simultaneously analyze the two critical factors related to battery degradation mechanisms.

6.2 Future work

The work presented in this dissertation reveals several avenues for further investigation. These research directions can be classified as either technology-driven, integrating two-dimensional Raman mapping functionality into the Fabry-Perot MEMS sensor platform, or as application-driven, investigating the development of a stress-free electrode.

Integrating two-dimensional Raman mapping with Fabry-Perot MEMS sensor platform:

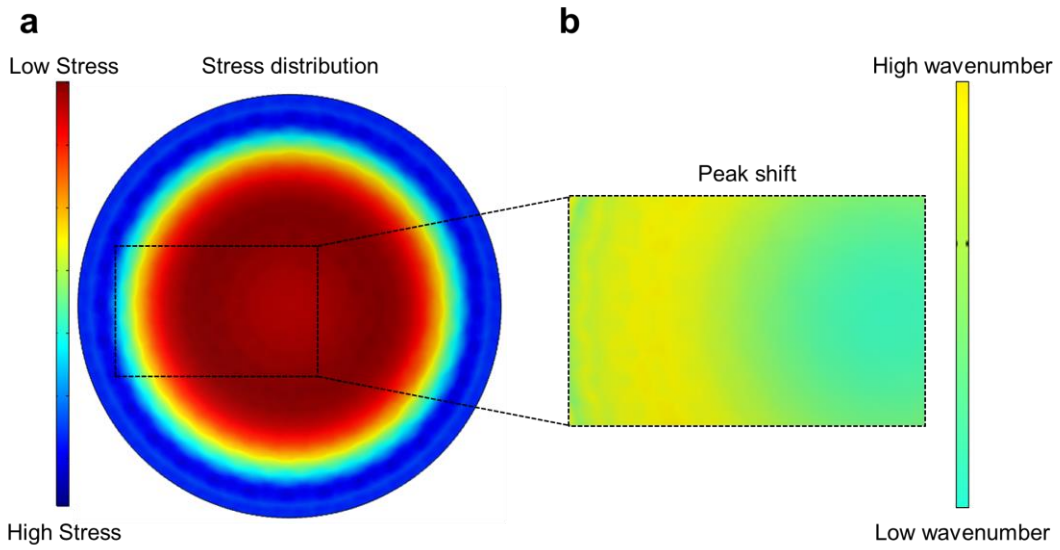

Figure 6-1: (a) Stress distribution of the electrode underneath the clamped circular membrane and (b) Raman mapping of the electrode, illustrating distribution of Raman peak shift.

During the battery operation, the V_2O_5 electrode underneath the clamped circular membrane exhibits stress distribution according to the shape of the membrane (Figure 6-1a). This stress distribution will promote/prevent the Li-ion

diffusion into the electrode, which has largely remained unknown since it can only be studied using finite models or numerical simulations.

Raman mapping is a powerful and non-destructive method capable of measuring mechanical stress with micrometric spatial resolution. This method yields two-dimensional images of the device structure by mapping local strain variations [171]. A complete spectrum is acquired at each and every pixel of the image within the designated area, and then interrogated to generate false color images based on material composition, phase, crystallinity and strain. After integrating this technique with the Fabry-Perot MEMS sensor platform, it will allow you to characterize how Li-ions are inserted into the electrode depending on the stress distribution in the electrode (Figure 6-1b).

Development of a stress-free electrode:

As previously discussed, repeated volume expansion, phase transition, and the associated Li diffusion-induced stress within electrode materials can lead to their pulverization and electrical isolation from the current collector which results in capacity loss. Therefore, considerable efforts have been made to minimize the Li diffusion-induced stress and increase cycle life of LIBs.

Development of a stress-free electrode which enables zero Li diffusion-induced stress during battery operation can lead to extended cycle life. In the previous experiments, the first demonstration of stacking two alternately stressed layers for investigation of battery degradation mechanisms has been presented. However, faster degradation in the stacked electrodes is observed due to the high

stress gradient at the boundary of the layers in spite of the reduced stress. One way to avoid this high stress gradient in the electrode is to stack multiple layers of alternately stressed layers (Figure 6-2). The tensile stress induced in the crystalline V_2O_5 (c-V_2O_5) layers and compressive stress from the amorphous V_2O_5 layers (a-V_2O_5) will compensate each other. At the same time, the stress gradient at the boundary of the layers will be evenly distributed in the vertical direction of the electrode, reducing the high stress gradient.

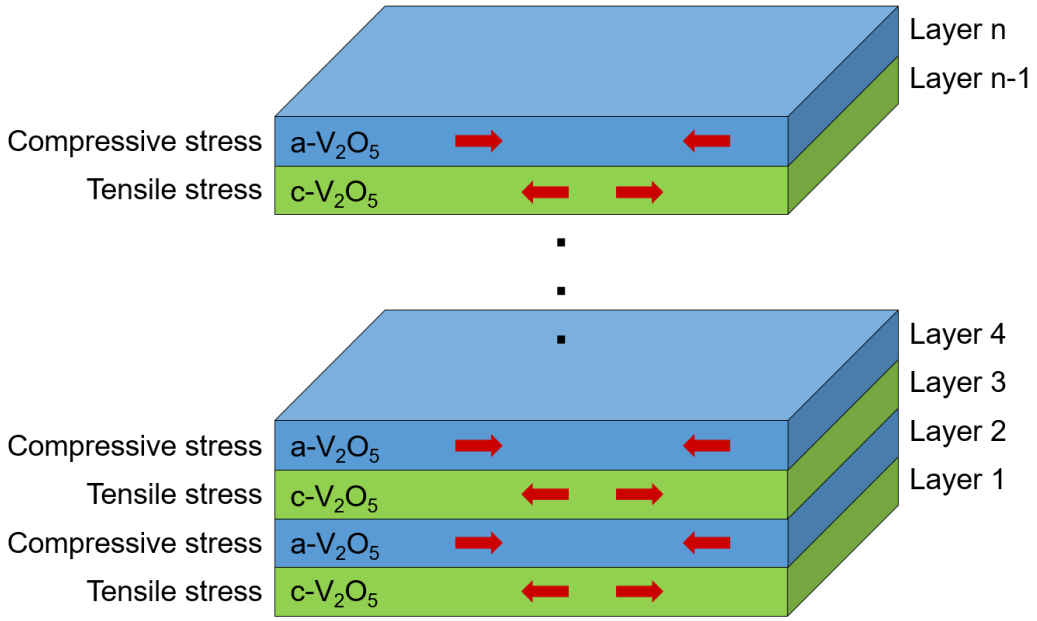

Figure 6-2: Simple diagram showing a stack of alternately stressed crystalline and amorphous V_2O_5 layers.

6.3 Conclusion

LIBs are the most pervasive energy storage devices providing high energy density while being compact and light-weight. Recently, new electric transportation systems including hybrid electric vehicles, plug-in hybrid electric

vehicles, and fully electric vehicles are becoming more and more important and these vehicles require even higher energy density and cycle life as well as improved safety and lower cost. A key challenge in these efforts has been understanding and characterizing these materials during battery operation. This need was addressed in this dissertation through the development MEMS sensor platforms for *in situ* characterization of stress and microstructural evolutions in LIB electrodes. The results demonstrated the unique advantages of using MEMS technology for battery research, especially for integration with different scientific equipment. These MEMS sensor platforms be eventually utilized for optimization of the LIB electrode performance by achieving fundamental understanding of the stress and microstructural changes during battery operation.

Appendix A: JavaScript

This JavaScript code automatically records a series of interference patterns and Raman spectroscopy measurement results sequentially in the computer connected to the Raman microscope throughout the entire experiment, along with a time stamp.

```
' Variable declaration
Const START_VIDEO = 0
Const SHOW_DATA = 0
Const HIDE_DATA = 1
Const REMOVE_DATA = 2
Const STOP_VIDEO = 1
Const GET_VIDEO_ID = 2

' Constant declaration, Use LabSpec parameters
Const ACQ_LABSPEC_PARAM = 2
' Constant declaration, Automatically show the data
Const ACQ_AUTO_SHOW = 10
' Use LabSpec parameters and automatically
Mode = ACQ_LABSPEC_PARAM + ACQ_AUTO_SHOW

Dim MainIndex

'Main Program
For MainIndex = 1 to 9999999 ' Do 2000 iterations For test
   TakeRaman()
   TurnVideoOn()
next
'End of the main program

Private Sub TurnVideoOn()
   Dim VideoIndex
   Dim PauseTime1
   Dim PauseTime2
   Dim sec
   Dim zero
   Dim mon
   Dim dat
   Dim hou
```

```
Dim min
Dim ImagePath
Dim ImageName

zero="0"
PauseTime1 = 5
PauseTime2 = 15
ImagePath="C:\Documents and Settings\RAMAN\ " 'Folder needs to be specified

For VideoIndex = 1 to 2
   LabSpec.Video START_VIDEO ' Start Video
   do
      VideoID = LabSpec.Video(GET_VIDEO_ID) ' Wait for the Video to be ready
   Loop Until VideoID>0
   LabSpec.Exec VideoID, HIDE_DATA, Param ' HIDE_DATA
   LabSpec.Pause PauseTime1 * 1000 ' Pause Time For 5 sec
   LabSpec.Video STOP_VIDEO ' Stop The Video Image

   if DatePart("m",Now()) < 10 then
      mon = zero & DatePart("m",Now())
   else
      mon = DatePart("m",Now())
   end if

   if DatePart("d",Now()) < 10 then
      dat = zero & DatePart("d",Now())
   else
      dat = DatePart("d",Now())
   end if

   if DatePart("h",Now()) < 10 then
      hou = zero & DatePart("h",Now())
   else
      hou = DatePart("h",Now())
   end if

   if DatePart("n",Now()) < 10 then
      min = zero & DatePart("n",Now())
   else
      min = DatePart("n",Now())
   end If

   If DatePart("s",Now()) < 10 then
      sec = zero & DatePart("s",Now())
```

```
        else
           sec = DatePart("s",Now())
        end If

        ImageName = mon & dat & hou & min & sec
        LabSpec.Save VideoID, ImagePath & ImageName & ".jpg", "jpg" ' Save Video
Image
        LabSpec.Exec VideoID, REMOVE_DATA, Param
        LabSpec.Pause PauseTime2 * 1000 ' Pause Time For 15 sec
    next
End Sub

Private Sub TakeRaman()
    Dim FileName ' Variable declaration to store the data file name
    Dim DataID ' variable to store the data ID
    Dim Param ' Variable declaration, not used with SHOW_DATA
    Dim Format ' Variable declaration to store the data format
    Dim ReturnValue ' Variable declaration to store the return value
    Dim Index ' Variable declaration to store the file Index
    Dim Mode ' Variable declaration, Acquisition mode
    Dim IntegrationTime ' Variable declaration, Acquisition time
    Dim AccumulationNum ' Variable declaration, Number of Accumulation
    Dim AcqFrom ' Variable declaration, Spectral range from
    Dim AcqTo ' Variable declaration, Spectral range to
    Dim zero
    Dim mon
    Dim min
    Dim dat
    Dim hou
    Dim sec

    zero="0"
    FilePath = "C:\Documents and Settings\RAMAN\" 'Folder needs to be specified
    IntegrationTime = 30  ' Not used
    AccumulationNum = 3  ' Not used

    LabSpec.Acq Mode,IntegrationTime,AccumulationNum,AcqFrom,AcqTo ' Start
an acquisition
    do
        DataID=LabSpec.GetAcqID() ' Wait until Spectrum is ready (acquisition is
done)
    Loop Until DataID>0

    if DatePart("m",Now()) < 10 then
```

```
        mon = zero & DatePart("m",Now())
    else
        mon = DatePart("m",Now())
    end if

    if DatePart("d",Now()) < 10 then
        dat = zero & DatePart("d",Now())
    else
        dat = DatePart("d",Now())
    end if

    if DatePart("h",Now()) < 10 then
        hou = zero & DatePart("h",Now())
    else
        hou = DatePart("h",Now())
    end if

    if DatePart("n",Now()) < 10 then
        min = zero & DatePart("n",Now())
    else
        min = DatePart("n",Now())
    End If

    If DatePart("s",Now()) < 10 Then
        sec = zero & DatePart("s",Now())
    else
        sec = DatePart("s",Now())
    end if

    FileName = mon & dat & hou & min & sec
    Format= "ngs"
    LabSpec.Save DataID, FilePath & FileName & ".ngs", Format ' Save acquired data
to the disk
    LabSpec.Exec DataID, REMOVE_DATA, Param
End Sub
```

References

[1] J.-M. Tarascon, and M. Armand, "Issues and challenges facing rechargeable lithium batteries," *Nature*, vol.414, pp.359–367, 2001.

[2] M.T. McDowell, S.W. Lee, W.D. Nix, and Y. Cui, "25th anniversary article: Understanding the lithiation of silicon and other alloying anodes for lithium-ion batteries.," *Advanced Materials*, vol.25, pp.4966–85, September 2013.

[3] R. Baddour-Hadjean, and J.-P. Pereira-Ramos, "Raman Microspectrometry Applied to the Study of Electrode Materials for Lithium Batteries," *Chemical Reviews*, vol.110, pp.1278–1319, 2010.

[4] R. Hausbrand, G. Cherkashinin, H. Ehrenberg, M. Gröting, K. Albe, C. Hess, and W. Jaegermann, "Fundamental degradation mechanisms of layered oxide Li-ion battery cathode materials: Methodology, insights and novel approaches," *Materials Science and Engineering: B*, vol.192, pp.3–25, 2015.

[5] M.J. Chon, V.A. Sethuraman, A. McCormick, V. Srinivasan, and P.R. Guduru, "Real-time measurement of stress and damage evolution during initial lithiation of crystalline silicon," *Phys Rev Lett*, vol.107, pp.45503, 2011. http://dx.doi.org/.

[6] V.A. Sethuraman, V. Srinivasan, A.F. Bower, and P.R. Guduru, "In Situ Measurements of Stress-Potential Coupling in Lithiated Silicon," *Journal of The Electrochemical Society* , vol.157 , pp.A1253–A1261, November 2010.

[7] P.P.R.M.L. Harks, F.M. Mulder, and P.H.L. Notten, "In situ methods for Li-ion battery research: A review of recent developments," *Journal of Power Sources*, vol.288, pp.92–105, 2015.

[8] V.A. Sethuraman, M.J. Chon, M. Shimshak, V. Srinivasan, and P.R. Guduru, "In situ measurements of stress evolution in silicon thin films during electrochemical lithiation and delithiation," *Journal of Power Sources*, vol.195, pp.5062–5066, 2010.

[9] X.H. Liu, Y. Liu, A. Kushima, S. Zhang, T. Zhu, J. Li, and J.Y. Huang, "In Situ TEM Experiments of Electrochemical Lithiation and Delithiation of Individual Nanostructures," *Advanced Energy Materials*, vol.2, pp.722–741, 2012.

[10] K.J. Rhodes, R. Meisner, M. Kirkham, N. Dudney, and C. Daniel, "In Situ XRD of Thin Film Tin Electrodes for Lithium Ion Batteries," *Journal of The Electrochemical Society*, vol.159, pp.A294–A299, 2012.

[11] M. Balasubramanian, X. Sun, X.Q. Yang, and J. McBreen, "In situ X-ray diffraction and X-ray absorption studies of high-rate lithium-ion batteries," *Journal of Power Sources*, vol.92, pp.1–8, 2001.

[12] H.. Espinosa, B.. Prorok, and M. Fischer, "A methodology for determining mechanical properties of freestanding thin films and MEMS materials,"

Journal of the Mechanics and Physics of Solids, vol.51, pp.47–67, January 2003.

[13] E. Pomerantseva, H. Jung, M. Gnerlich, S. Baron, K. Gerasopoulos, and R. Ghodssi, "A MEMS platform for in situ , real-time monitoring of electrochemically induced mechanical changes in lithium-ion battery electrodes," *Journal of Micromechanics and Microengineering*, vol.23, pp.114018, 2013.

[14] M. Pharr, Z. Suo, and J.J. Vlassak, "Measurements of the Fracture Energy of Lithiated Silicon Electrodes of Li-Ion Batteries," *Nano Letters*, vol.13, pp.5570–5577, November 2013.

[15] A.S. Aric, P. Bruce, B. Scrosati, J.-M. Tarascon, and W. van Schalkwijk, "Nanostructured materials for advanced energy conversion and storage devices," *Nature Materials*, vol.4, pp.366–377, 2005.

[16] M. Armand, and J.-M. Tarascon, "Building better batteries," *Nature*, vol.451, pp.652–657, 2008.

[17] J.B. Goodenough, and Y. Kim, "Challenges for Rechargeable Li Batteries," *Chemistry of Materials*, vol.22, pp.587, 2009.

[18] H. Li, Z. Wang, L. Chen, and X. Huang, "Research on Advanced Materials for Li-ion Batteries," *Advanced Materials*, vol.21, pp.4593–4607, 2009.

[19] K. Gerasopoulos, INTEGRATION AND CHARACTERIZATION OF TOBACCO MOSAIC VIRUS BASED NANOSTRUCTURED MATERIALS IN THREE-DIMENSIONAL MICROBATTERY ARCHITECTURES, University of Maryland, 2012.

[20] J.O. Besenhard, P. Komenda, A. Paxinos, and E. Wudy, "Binary and ternary Li-alloys as anode materials in rechargeable organic electrolyte Li-batteries," *Solid State Ionics*, vol.Volumes 18, pp.823–827, 1986.

[21] H.J. Jung, M. Park, Y.G. Yoon, G.B. Kim, and S.K. Joo, "Amorphous silicon anode for lithium-ion rechargeable batteries," *Journal of Power Sources*, vol.115, pp.346–351, 2003.

[22] J. Wang, I.D. Raistrick, and R.A. Huggins, "Behavior of Some Binary Lithium Alloys as Negative Electrodes in Organic Solvent-Based Electrolytes," *Journal of the Electrochemical Society*, vol.133, pp.457–460, 1986.

[23] J.O. Besenhard, J. Yang, and M. Winter, "Will advanced lithium-alloy anodes have a chance in lithium-ion batteries?," *Journal of Power Sources*, vol.68, pp.87–90, 1997.

[24] S. Ohara, J. Suzuki, K. Sekine, and T. Takamura, "A thin film silicon anode for Li-ion batteries having a very large specific capacity and long cycle life," *Journal of Power Sources*, vol.136, pp.303–306, 2004.

[25] B.A. Boukamp, G.C. Lesh, and R.A. Huggins, "All-Solid Lithium Electrodes with Mixed-Conductor Matrix," *Journal of the Electrochemical Society*, vol.128, pp.725–729, 1981.

[26] M.K. Datta, J. Maranchi, S.J. Chung, R. Epur, K. Kadakia, P. Jampani, and P.N. Kumta, "Amorphous silicon–carbon based nano-scale thin film anode materials for lithium ion batteries," *Electrochimica Acta*, vol.56, pp.4717–4723, 2011.

[27] U. Kasavajjula, C. Wang, and A.J. Appleby, "Nano- and bulk-silicon-based insertion anodes for lithium-ion secondary cells," *Journal of Power Sources*, vol.163, pp.1003–1039, 2007.

[28] J. Li, A.K. Dozier, Y. Li, F. Yang, and Y.-T. Cheng, "Crack Pattern Formation in Thin Film Lithium-Ion Battery Electrodes," *Journal of The Electrochemical Society*, vol.158, pp.A689–A694, 2011.

[29] C. Navone, R. Baddour-Hadjean, J.P. Pereira-Ramos, and R. Salot, "A kinetic study of electrochemical lithium insertion into oriented V2O5 thin films prepared by rf sputtering," *Electrochimica Acta*, vol.53, pp.3329–3336, 2008.

[30] J.M. Cocciantelli, P. Gravereau, J.P. Doumerc, M. Pouchard, and P. Hagenmuller, "On the preparation and characterization of a new polymorph of V2O5," *Journal of Solid State Chemistry*, vol.93, pp.497–502, 1991.

[31] C. Julien, I. Ivanov, and A. Gorenstein, "Vibrational modifications on lithium intercalation in V2O5 films," *Materials Science and Engineering: B*, vol.33, pp.168–172, 1995.

[32] H. Du, and R. Bogue, "MEMS sensors: past, present and future," *Sensor Review*, vol.27, pp.7–13, 2007.

[33] W. Cheng, M.J. Campolongo, S.J. Tan, and D. Luo, "Freestanding ultrathin nano-membranes via self-assembly," *Nano Today*, vol.4, pp.482–493, 2009.

[34] W.N. Sharpe Jr., Mechanical properties of MEMS materials, in: Semiconductor Device Research Symposium, 2001 International, 2001: pp. 416–417.

[35] S.D. Senturia, "Microsystem design.", Kluwer Academic Publishers Norwell, MA, USA, 2001.

[36] S.M. Spearing, "Materials issues in microelectromechanical systems (MEMS)," *Acta Materialia*, vol.48, pp.179–196, 2000.

[37] R. Zhang, D. Shilo, G. Ravichandran, and K. Bhattacharya, "Mechanical Characterization of Released Thin Films by Contact Loading," *Journal of Applied Mechanics*, vol.73, pp.730–736, 2005.

[38] K.Y. Chung, and K.-B. Kim, "Investigation of Structural Fatigue in Spinel Electrodes Using In Situ Laser Probe Beam Deflection Technique ," *Journal of The Electrochemical Society* , vol.149 , pp.A79–A85, January 2002.

[39] H. Mukaibo, T. Momma, Y. Shacham-Diamand, T. Osaka, and M. Kodaira, "In Situ Stress Transition Observations of Electrodeposited Sn-Based Anode Materials for Lithium-Ion Secondary Batteries," *Electrochemical and Solid-State Letters*, vol.10, pp.A70, 2007.

[40] S.-I. Pyun, K.-H. Kim, and J.-N. Han, "Analysis of stresses generated during hydrogen extraction from and injection into Ni(OH)2/NiOOH film electrode," *Journal of Power Sources*, vol.91, pp.92–98, 2000.

[41] S.J. Lee, J.K. Lee, S.H. Chung, H.Y. Lee, S.M. Lee, and H.K. Baik, "Stress effect on cycle properties of the silicon thin-film anode," *Journal of Power Sources*, vol.Volumes 97, pp.191–193, 2001.

[42] W. Schomburg, "Introduction to Microsystem Design.", Springer, 2011.

[43] B.A.G. and T.M.L. and E.V.M. and J.W.A. and C.K. Harnett, "Bistable out-of-plane stress-mismatched thermally actuated bilayer devices with large deflection," *Journal of Micromechanics and Microengineering*, vol.21, pp.65030, 2011.

[44] D.S. Popescu, T.S.J. Lammerink, and M. Elwenspoek, Buckled membranes for microstructures, in: Micro Electro Mechanical Systems, 1994, MEMS '94, Proceedings, IEEE Workshop on, 1994: pp. 188–192.

[45] V. Ziebart, O. Paul, and H. Baltes, "Strongly buckled square micromachined membranes," *Microelectromechanical Systems, Journal of*, vol.8, pp.423–432, 1999.

[46] R.G. and K.M.W. and T.A.B. Usha, "Fabrication of polyimide bi-stable diaphragms using oxide compressive stresses for the field of "Buckle MEMS,"" *Journal of Micromechanics and Microengineering*, vol.20, pp.75013, 2010.

[47] O.T. von Ramm, and D.R. Chou, Piezoelectric Micromachined Ultrasound Transducers for Medical Imaging, Duke, 2011.

[48] M.O. and T.X. and L.S.O. and J.M.M. and Z.H. Wang, "Investigation of residual stress and its effects on the vibrational characteristics of piezoelectric-based multilayered microdiaphragms," *Journal of Micromechanics and Microengineering*, vol.20, pp.15007, 2010.

[49] M. Li, M. Wang, T. Wang, H. Rong, and X. Chen, Analysis on the optical MEMS pressure sensors based on circular multilayer diaphragm, in: Photonics Asia 2004, International Society for Optics and Photonics, 2004: pp. 238–245.

[50] J.W. Hutchinson, "Stresses and failure modes in thin films and multilayers.", 1996.

[51] O. Zohni, G. Buckner, T. Kim, A. Kingon, J. Maranchi, and S. Richard, "Investigating thin film stresses in stacked silicon dioxide/silicon nitride

structures and quantifying their effects on frequency response," *Journal of Micromechanics and Microengineering*, vol.17, pp.1042, 2007.

[52] A. Mukhopadhyay, and B.W. Sheldon, "Deformation and stress in electrode materials for Li-ion batteries," *Progress in Materials Science*, vol.63, pp.58–116, June 2014.

[53] G.G. Stoney, The Tension of Metallic Films Deposited by Electrolysis, in: Proceedings of the Royal Society A, The Royal Society, London, 1909: pp. 172–175.

[54] L.B. Freund, and S. Suresh, "Thin Film Materials Stress Defect Formation And Surface Evolution | Materials science | Cambridge University Press.", Cambridge Univeristy Press, UK, n.d.

[55] J.J. Brown, S.-H. Lee, J. Xiao, and Z. Wu, "Observations of stress accumulation and relaxation in solid-state lithiation and delithiation of suspended Si microcantilevers," *Physica Status Solidi (a)*, pp.1–13, February 2016.

[56] J.H. Yang, J.C.M. Chen, and M.M.C. Cheng, In-situ nanomechanical characterization of electrochemical cycles in lithium ion batteries, in: Solid-State Sensors, Actuators and Microsystems (TRANSDUCERS & EUROSENSORS XXVII), 2013 Transducers & Eurosensors XXVII: The 17th International Conference on, 2013: pp. 438–441.

[57] Y. Qi, and S.J. Harris, "In Situ Observation of Strains during Lithiation of a Graphite Electrode," *Journal of the Electrochemical Society*, vol.157, pp.A741–A747, 2010.

[58] V.A. Sethuraman, M.J. Chon, M. Shimshak, N. Van Winkle, and P.R. Guduru, "In situ measurement of biaxial modulus of Si anode for Li-ion batteries," *Electrochemistry Communications*, vol.12, pp.1614–1617, 2010.

[59] V.A. Sethuraman, N. Van Winkle, D.P. Abraham, A.F. Bower, and P.R. Guduru, "Real-time stress measurements in lithium-ion battery negative-electrodes," *Journal of Power Sources*, vol.206, pp.334–342, 2012.

[60] M. Pharr, Z. Suo, and J.J. Vlassak, "Variation of stress with charging rate due to strain-rate sensitivity of silicon electrodes of Li-ion batteries," *Journal of Power Sources*, vol.270, pp.569–575, 2014.

[61] S. Bhattacharya, A.R. Riahi, and A.T. Alpas, "In-situ observations of lithiation/de-lithiation induced graphite damage during electrochemical cycling," *Scripta Materialia*, vol.64, pp.165–168, January 2011.

[62] J. Chen, A.K. Thapa, and T.A. Berfield, "In-situ characterization of strain in lithium battery working electrodes," *Journal of Power Sources*, vol.271, pp.406–413, December 2014.

[63] S.J. Harris, A. Timmons, D.R. Baker, and C. Monroe, "Direct in situ measurements of Li transport in Li-ion battery negative electrodes," *Chemical Physics Letters*, vol.485, pp.265–274, January 2010.

[64] P. Maire, H. Kaiser, W. Scheifele, and P. Novák, "Colorimetric determination of lithium-ion mobility in graphite composite electrodes," *Journal of Electroanalytical Chemistry*, vol.644, pp.127–131, June 2010.

[65] K. Nishikawa, T. Mori, T. Nishida, Y. Fukunaka, and M. Rosso, "Li dendrite growth and Li+ ionic mass transfer phenomenon," *Journal of Electroanalytical Chemistry*, vol.661, pp.84–89, October 2011.

[66] K. Nishikawa, H. Munakata, and K. Kanamura, "In-situ observation of one silicon particle during the first charging," *Journal of Power Sources*, vol.243, pp.630–634, December 2013.

[67] F. Sagane, K. Ikeda, K. Okita, H. Sano, H. Sakaebe, and Y. Iriyama, "Effects of current densities on the lithium plating morphology at a lithium phosphorus oxynitride glass electrolyte/copper thin film interface," *Journal of Power Sources*, vol.233, pp.34–42, July 2013.

[68] H. Sano, H. Sakaebe, and H. Matsumoto, "In Situ Morphology Observations of Electrodeposited Lithium in Room-Temperature Ionic Liquids by Optical Microscopy," *Chemistry Letters*, vol.42, pp.77–79, 2013.

[69] J. Steiger, D. Kramer, and R. Mönig, "Microscopic observations of the formation, growth and shrinkage of lithium moss during electrodeposition and dissolution," *Electrochimica Acta*, vol.136, pp.529–536, August 2014.

[70] L.Y. Beaulieu, K.W. Eberman, R.L. Turner, L.J. Krause, and J.R. Dahn, "Colossal Reversible Volume Changes in Lithium Alloys," *Electrochemical and Solid-State Letters*, vol.4, pp.A137–A140, 2001.

[71] M. Rosso, C. Brissot, A. Teyssot, M. Dollé, L. Sannier, J.-M. Tarascon, R. Bouchet, and S. Lascaud, "Dendrite short-circuit and fuse effect on Li/polymer/Li cells," *Electrochimica Acta*, vol.51, pp.5334–5340, 2006.

[72] D. Chen, S. Indris, M. Schulz, B. Gamer, and R. Mönig, "In situ scanning electron microscopy on lithium-ion battery electrodes using an ionic liquid," *Journal of Power Sources*, vol.196, pp.6382–6387, 2011.

[73] F. Orsini, A. Du Pasquier, B. Beaudoin, J.M. Tarascon, M. Trentin, N. Langenhuizen, E. De Beer, and P. Notten, "In situ Scanning Electron Microscopy (SEM) observation of interfaces within plastic lithium batteries," *Journal of Power Sources*, vol.76, pp.19–29, 1998.

[74] D.J. Miller, C. Proff, J.G. Wen, D.P. Abraham, and J. Bareño, "Observation of Microstructural Evolution in Li Battery Cathode Oxide Particles by In Situ Electron Microscopy," *Advanced Energy Materials*, vol.3, pp.1098–1103, August 2013.

[75] S.T. Boles, A. Sedlmayr, O. Kraft, and R. Mönig, "In situ cycling and mechanical testing of silicon nanowire anodes for lithium-ion battery applications," *Applied Physics Letters*, vol.100, pp.243901, 2012.

[76] P. Hovington, M. Dontigny, A. Guerfi, J. Trottier, M. Lagacé, A. Mauger, C.M. Julien, and K. Zaghib, "In situ Scanning electron microscope study and microstructural evolution of nano silicon anode for high energy Li-ion batteries," *Journal of Power Sources*, vol.248, pp.457–464, February 2014.

[77] S.T. Boles, C. V. Thompson, O. Kraft, and R. Mönig, "In situ tensile and creep testing of lithiated silicon nanowires," *Applied Physics Letters*, vol.103, pp.263906, December 2013.

[78] F. Sagane, R. Shimokawa, H. Sano, H. Sakaebe, and Y. Iriyama, "In-situ scanning electron microscopy observations of Li plating and stripping reactions at the lithium phosphorus oxynitride glass electrolyte/Cu interface," *Journal of Power Sources*, vol.225, pp.245–250, March 2013.

[79] M. Nagao, A. Hayashi, M. Tatsumisago, T. Kanetsuku, T. Tsuda, and S. Kuwabata, "In situ SEM study of a lithium deposition and dissolution mechanism in a bulk-type solid-state cell with a Li2S-P2S5 solid electrolyte," *Physical Chemistry Chemical Physics*, vol.15, pp.18600–18606, 2013.

[80] J.Y. Huang, L. Zhong, C.M. Wang, J.P. Sullivan, W. Xu, L.Q. Zhang, S.X. Mao, N.S. Hudak, X.H. Liu, A. Subramanian, H. Fan, L. Qi, A. Kushima, and J. Li, "In Situ Observation of the Electrochemical Lithiation of a Single SnO2 Nanowire Electrode," *Science*, vol.330, pp.1515–1520, 2010.

[81] K. Yamamoto, Y. Iriyama, T. Asaka, T. Hirayama, H. Fujita, C.A.J. Fisher, K. Nonaka, Y. Sugita, and Z. Ogumi, "Dynamic Visualization of the Electric Potential in an All-Solid-State Rechargeable Lithium Battery," *Angewandte Chemie International Edition*, vol.49, pp.4414–4417, 2010.

[82] X.H. Liu, and J.Y. Huang, "In situ TEM electrochemistry of anode materials in lithium ion batteries," *Energy & Environmental Science*, vol.4, pp.3844–3860, 2011.

[83] Q. Liu, Y. Liu, C.-J. Sun, Z. Li, Y. Ren, W. Lu, E.A. Stach, and J. Xie, "The Structural Evolution of V2O5 Nanocystals during Electrochemical Cycling Studied Using In operando Synchrotron Techniques," *Electrochimica Acta*, vol.136, pp.318–322, August 2014.

[84] M.N. Obrovac, and L. Christensen, "Structural Changes in Silicon Anodes during Lithium Insertion/Extraction," *Electrochemical and Solid-State Letters*, vol.7, pp.A93–A96, 2004.

[85] T.D. Hatchard, and J.R. Dahn, "In Situ XRD and Electrochemical Study of the Reaction of Lithium with Amorphous Silicon," *Journal of The Electrochemical Society*, vol.151, pp.A838–A842, 2004.

[86] J. Li, and J.R. Dahn, "An In Situ X-Ray Diffraction Study of the Reaction of Li with Crystalline Si," *Journal of The Electrochemical Society*, vol.154, pp.A156–A161, 2007.

[87] S. Misra, N. Liu, J. Nelson, S.S. Hong, Y. Cui, and M.F. Toney, "In Situ X-ray Diffraction Studies of (De)lithiation Mechanism in Silicon Nanowire Anodes," *ACS Nano*, vol.6, pp.5465–5473, August 2012.

[88] E.S. Takeuchi, A.C. Marschilok, K.J. Takeuchi, A. Ignatov, Z. Zhong, and M. Croft, "Energy dispersive X-ray diffraction of lithium-silver vanadium phosphorous oxide cells: in situ cathode depth profiling of an electrochemical reduction-displacement reaction," *Energy & Environmental Science*, vol.6, pp.1465–1470, 2013.

[89] F. Wang, L. Wu, B. Key, X.-Q. Yang, C.P. Grey, Y. Zhu, and J. Graetz, "Electrochemical Reaction of Lithium with Nanostructured Silicon Anodes: A Study by In-Situ Synchrotron X-Ray Diffraction and Electron Energy-Loss Spectroscopy," *Advanced Energy Materials*, vol.3, pp.1324–1331, October 2013.

[90] H. Arai, K. Sato, Y. Orikasa, H. Murayama, I. Takahashi, Y. Koyama, Y. Uchimoto, and Z. Ogumi, "Phase transition kinetics of LiNi0.5Mn1.5O4 electrodes studied by in situ X-ray absorption near-edge structure and X-ray diffraction analysis," *Journal of Materials Chemistry A*, vol.1, pp.10442–10449, 2013.

[91] L. Baggetto, and P.H.L. Notten, "Lithium-Ion (De)Insertion Reaction of Germanium Thin-Film Electrodes: An Electrochemical and In Situ XRD Study," *Journal of The Electrochemical Society* , vol.156 , pp.A169–A175, March 2009.

[92] M. Fehse, M. Ben Yahia, L. Monconduit, F. Lemoigno, M.-L. Doublet, F. Fischer, C. Tessier, and L. Stievano, "New Insights on the Reversible Lithiation Mechanism of TiO2(B) by Operando X-ray Absorption Spectroscopy and X-ray Diffraction Assisted by First-Principles Calculations," *The Journal of Physical Chemistry C*, vol.118, pp.27210–27218, November 2014.

[93] C.R. Fell, M. Chi, Y.S. Meng, and J.L. Jones, "In situ X-ray diffraction study of the lithium excess layered oxide compound Li[Li0.2Ni0.2Mn0.6]O2 during electrochemical cycling," *Solid State Ionics*, vol.207, pp.44–49, January 2012.

[94] H. He, C. Huang, C.-W. Luo, J.-J. Liu, and Z.-S. Chao, "Dynamic study of Li intercalation into graphite by in situ high energy synchrotron XRD," *Electrochimica Acta*, vol.92, pp.148–152, March 2013.

[95] M. Hirayama, H. Ido, K. Kim, W. Cho, K. Tamura, J. Mizuki, and R. Kanno, "Dynamic Structural Changes at LiMn2O4/Electrolyte Interface during

Lithium Battery Reaction," *Journal of the American Chemical Society*, vol.132, pp.15268–15276, November 2010.

[96] C.-W. Hu, T.-Y. Chen, K.-S. Shih, P.-J. Wu, H.-C. Su, C.-Y. Chiang, A.-F. Huang, H.-W. Hsieh, C.-C. Chang, B.-Y. Shew, and C.-H. Lee, "Real-time investigation on the influences of vanadium additives to the structural and chemical state evolutions of LiFePO4 for enhancing the electrochemical performance of lithium-ion battery," *Journal of Power Sources*, vol.270, pp.449–456, December 2014.

[97] X. Hua, R. Robert, L.-S. Du, K.M. Wiaderek, M. Leskes, K.W. Chapman, P.J. Chupas, and C.P. Grey, "Comprehensive Study of the CuF2 Conversion Reaction Mechanism in a Lithium Ion Battery," *The Journal of Physical Chemistry C*, vol.118, pp.15169–15184, July 2014.

[98] K.C. Kirshenbaum, D.C. Bock, Z. Zhong, A.C. Marschilok, K.J. Takeuchi, and E.S. Takeuchi, "In situ profiling of lithium/Ag2VP2O8 primary batteries using energy dispersive X-ray diffraction," *Physical Chemistry Chemical Physics*, vol.16, pp.9138–9147, 2014.

[99] K. Kirshenbaum, D.C. Bock, C.-Y. Lee, Z. Zhong, K.J. Takeuchi, A.C. Marschilok, and E.S. Takeuchi, "In situ visualization of Li/Ag2VP2O8 batteries revealing rate-dependent discharge mechanism," *Science*, vol.347, pp.149–154, January 2015. http://science.sciencemag.org/content/347/6218/149.abstract.

[100] Q. Liu, H. He, Z.-F. Li, Y. Liu, Y. Ren, W. Lu, J. Lu, E.A. Stach, and J. Xie, "Rate-Dependent, Li-Ion Insertion/Deinsertion Behavior of LiFePO4 Cathodes in Commercial 18650 LiFePO4 Cells," *ACS Applied Materials & Interfaces*, vol.6, pp.3282–3289, March 2014.

[101] D. Lv, J. Bai, P. Zhang, S. Wu, Y. Li, W. Wen, Z. Jiang, J. Mi, Z. Zhu, and Y. Yang, "Understanding the High Capacity of Li2FeSiO4: In Situ XRD/XANES Study Combined with First-Principles Calculations," *Chemistry of Materials*, vol.25, pp.2014–2020, May 2013.

[102] D. Mohanty, S. Kalnaus, R.A. Meisner, K.J. Rhodes, J. Li, E.A. Payzant, D.L. Wood III, and C. Daniel, "Structural transformation of a lithium-rich Li1.2Co0.1Mn0.55Ni0.15O2 cathode during high voltage cycling resolved by in situ X-ray diffraction," *Journal of Power Sources*, vol.229, pp.239–248, May 2013.

[103] W.K. Pang, V.K. Peterson, N. Sharma, C. Zhang, and Z. Guo, "Evidence of Solid-Solution Reaction upon Lithium Insertion into Cryptomelane K0.25Mn2O4 Material," *The Journal of Physical Chemistry C*, vol.118, pp.3976–3983, February 2014.

[104] M.R. Roberts, A. Madsen, C. Nicklin, J. Rawle, M.G. Palmer, J.R. Owen, and A.L. Hector, "Direct Observation of Active Material Concentration Gradients

and Crystallinity Breakdown in LiFePO4 Electrodes During Charge/Discharge Cycling of Lithium Batteries," *The Journal of Physical Chemistry C*, vol.118, pp.6548–6557, April 2014.

[105] K. Sakamoto, M. Hirayama, N. Sonoyama, D. Mori, A. Yamada, K. Tamura, J. Mizuki, and R. Kanno, "Surface Structure of LiNi0.8Co0.2O2: a New Experimental Technique Using in Situ X-ray Diffraction and Two-Dimensional Epitaxial Film Electrodes," *Chemistry of Materials*, vol.21, pp.2632–2640, July 2009.

[106] C.-H. Shen, L. Huang, Z. Lin, S.-Y. Shen, Q. Wang, H. Su, F. Fu, and X.-M. Zheng, "Kinetics and Structural Changes of Li-Rich Layered Oxide 0.5Li2MnO3·0.5LiNi0.292Co0.375Mn0.333O2 Material Investigated by a Novel Technique Combining in Situ XRD and a Multipotential Step," *ACS Applied Materials & Interfaces*, vol.6, pp.13271–13279, August 2014.

[107] C.-H. Shen, Q. Wang, F. Fu, L. Huang, Z. Lin, S.-Y. Shen, H. Su, X.-M. Zheng, B.-B. Xu, J.-T. Li, and S.-G. Sun, "Facile Synthesis of The Li-Rich Layered Oxide Li1.23Ni0.09Co0.12Mn0.56O2 with Superior Lithium Storage Performance and New Insights into Structural Transformation of the Layered Oxide Material during Charge–Discharge Cycle: In Situ XRD Characterization," *ACS Applied Materials & Interfaces*, vol.6, pp.5516–5524, April 2014.

[108] K. Shen, H. Chen, F. Klaver, F.M. Mulder, and M. Wagemaker, "Impact of Particle Size on the Non-Equilibrium Phase Transition of Lithium-Inserted Anatase TiO2," *Chemistry of Materials*, vol.26, pp.1608–1615, February 2014.

[109] A. Singer, A. Ulvestad, H.-M. Cho, J.W. Kim, J. Maser, R. Harder, Y.S. Meng, and O.G. Shpyrko, "Nonequilibrium Structural Dynamics of Nanoparticles in LiNi1/2Mn3/2O4 Cathode under Operando Conditions," *Nano Letters*, vol.14, pp.5295–5300, September 2014.

[110] F.C. Strobridge, R.J. Clément, M. Leskes, D.S. Middlemiss, O.J. Borkiewicz, K.M. Wiaderek, K.W. Chapman, P.J. Chupas, and C.P. Grey, "Identifying the Structure of the Intermediate, Li2/3CoPO4, Formed during Electrochemical Cycling of LiCoPO4," *Chemistry of Materials*, vol.26, pp.6193–6205, November 2014.

[111] S. Taminato, M. Hirayama, K. Suzuki, K. Kim, Y. Zheng, K. Tamura, J. Mizuki, and R. Kanno, "Mechanistic studies on lithium intercalation in a lithium-rich layered material using Li2RuO3 epitaxial film electrodes and in situ surface X-ray analysis," *Journal of Materials Chemistry A*, vol.2, pp.17875–17882, 2014.

[112] A. Ulvestad, A. Singer, H.-M. Cho, J.N. Clark, R. Harder, J. Maser, Y.S. Meng, and O.G. Shpyrko, "Single Particle Nanomechanics in Operando Batteries via Lensless Strain Mapping," *Nano Letters*, vol.14, pp.5123–5127, September 2014.

[113] H. Zhou, M.-A. Einarsrud, and F. Vullum-Bruer, "In situ X-ray diffraction and electrochemical impedance spectroscopy of a nanoporous Li2FeSiO4/C cathode during the initial charge/discharge cycle of a Li-ion battery," *Journal of Power Sources*, vol.238, pp.478–484, September 2013.

[114] W. Zhu, D. Liu, J. Trottier, C. Gagnon, A. Guerfi, C.M. Julien, A. Mauger, and K. Zaghib, "Comparative studies of the phase evolution in M-doped LixMn1.5Ni0.5O4 (M = Co, Al, Cu and Mg) by in-situ X-ray diffraction," *Journal of Power Sources*, vol.264, pp.290–298, October 2014.

[115] W. Zhu, D. Liu, J. Trottier, C. Gagnon, A. Mauger, C.M. Julien, and K. Zaghib, "In-situ X-ray diffraction study of the phase evolution in undoped and Cr-doped LixMn1.5Ni0.5O4 ($0.1 \leq x \leq 1.0$) 5-V cathode materials," *Journal of Power Sources*, vol.242, pp.236–243, November 2013.

[116] C.P. Grey, and N. Dupré, "NMR Studies of Cathode Materials for Lithium-Ion Rechargeable Batteries," *Chemical Reviews*, vol.104, pp.4493–4512, August 2004.

[117] S.A. Krachkovskiy, A.D. Pauric, I.C. Halalay, and G.R. Goward, "Slice-Selective NMR Diffusion Measurements: A Robust and Reliable Tool for In Situ Characterization of Ion-Transport Properties in Lithium-Ion Battery Electrolytes," *The Journal of Physical Chemistry Letters*, vol.4, pp.3940–3944, November 2013.

[118] M. Klett, M. Giesecke, A. Nyman, F. Hallberg, R.W. Lindström, G. Lindbergh, and I. Furó, "Quantifying Mass Transport during Polarization in a Li Ion Battery Electrolyte by in Situ 7Li NMR Imaging," *Journal of the American Chemical Society*, vol.134, pp.14654–14657, September 2012.

[119] L. Zhou, M. Leskes, A.J. Ilott, N.M. Trease, and C.P. Grey, "Paramagnetic electrodes and bulk magnetic susceptibility effects in the in situ NMR studies of batteries: Application to Li1.08Mn1.92O4 spinels," *Journal of Magnetic Resonance*, vol.234, pp.44–57, September 2013.

[120] N.M. Trease, L. Zhou, H.J. Chang, B.Y. Zhu, and C.P. Grey, "In situ NMR of lithium ion batteries: Bulk susceptibility effects and practical considerations," *Solid State Nuclear Magnetic Resonance*, vol.42, pp.62–70, April 2012.

[121] K. Shimoda, M. Murakami, D. Takamatsu, H. Arai, Y. Uchimoto, and Z. Ogumi, "In situ NMR observation of the lithium extraction/insertion from LiCoO2 cathode," *Electrochimica Acta*, vol.108, pp.343–349, October 2013.

[122] N. Schweikert, A. Hofmann, M. Schulz, M. Scheuermann, S.T. Boles, T. Hanemann, H. Hahn, and S. Indris, "Suppressed lithium dendrite growth in lithium batteries using ionic liquid electrolytes: Investigation by electrochemical impedance spectroscopy, scanning electron microscopy, and in situ 7Li nuclear magnetic resonance spectroscopy," *Journal of Power Sources*, vol.228, pp.237–243, April 2013.

[123] S. Chandrashekar, N.M. Trease, H.J. Chang, L.-S. Du, C.P. Grey, and A. Jerschow, "7Li MRI of Li batteries reveals location of microstructural lithium," *Nat Mater*, vol.11, pp.311–315, April 2012. http://dx.doi.org/10.1038/nmat3246.

[124] F. Poli, J.S. Kshetrimayum, L. Monconduit, and M. Letellier, "New cell design for in-situ NMR studies of lithium-ion batteries," *Electrochemistry Communications*, vol.13, pp.1293–1295, December 2011.

[125] K. Gotoh, M. Izuka, J. Arai, Y. Okada, T. Sugiyama, K. Takeda, and H. Ishida, "In situ 7Li nuclear magnetic resonance study of the relaxation effect in practical lithium ion batteries," *Carbon*, vol.79, pp.380–387, November 2014.

[126] P. Mukherjee, A. Lagutchev, and D.D. Dlott, "In Situ Probing of Solid-Electrolyte Interfaces with Nonlinear Coherent Vibrational Spectroscopy," *Journal of The Electrochemical Society* , vol.159 , pp.A244–A252, January 2012.

[127] R. Bhattacharyya, B. Key, H. Chen, A.S. Best, A.F. Hollenkamp, and C.P. Grey, "In situ NMR observation of the formation of metallic lithium microstructures in lithium batteries," *Nat Mater*, vol.9, pp.504–510, 2010.

[128] B. Key, R. Bhattacharyya, M. Morcrette, V. Seznéc, J.-M. Tarascon, and C.P. Grey, "Real-Time NMR Investigations of Structural Changes in Silicon Electrodes for Lithium-Ion Batteries," *Journal of the American Chemical Society*, vol.131, pp.9239–9249, August 2009.

[129] B. Key, M. Morcrette, J.-M. Tarascon, and C.P. Grey, "Pair Distribution Function Analysis and Solid State NMR Studies of Silicon Electrodes for Lithium Ion Batteries: Understanding the (De)lithiation Mechanisms," *Journal of the American Chemical Society*, vol.133, pp.503–512, August 2010.

[130] K. Ogata, E. Salager, C.J. Kerr, A.E. Fraser, C. Ducati, A.J. Morris, S. Hofmann, and C.P. Grey, "Revealing lithium–silicide phase transformations in nano-structured silicon-based lithium ion batteries via in situ NMR spectroscopy," *Nat Commun*, vol.5, 2014.

[131] C.M. Burba, and R. Frech, "Modified Coin Cells for xV2O5 for Lithium Rechargeable Batteries," *Applied Spectroscopy*, vol.60, pp.490–493, 2006.

[132] J. Wu, G.K.P. Dathar, C. Sun, M.G. Theivanayagam, D. Applestone, A.G. Dylla, A. Manthiram, G. Henkelman, J.B. Goodenough, and K.J. Stevenson, "In situ Raman spectroscopy of LiFePO4 : size and morphology dependence during charge and self-discharge," *Nanotechnology*, vol.24, pp.424009, 2013.

[133] R. Baddour-Hadjean, C. Navone, and J.P. Pereira-Ramos, "In situ Raman microspectrometry investigation of electrochemical lithium intercalation into sputtered crystalline V2O5 thin films," *Electrochimica Acta*, vol.54, pp.6674–6679, 2009.

[134] T. Gross, L. Giebeler, and C. Hess, "Novel in situ cell for Raman diagnostics of lithium-ion batteries.," *The Review of Scientific Instruments*, vol.84, pp.073109, July 2013.

[135] S. Hy, Y.-H. Chen, J. Liu, J. Rick, and B.-J. Hwang, "In situ surface enhanced Raman spectroscopic studies of solid electrolyte interphase formation in lithium ion battery electrodes," *Journal of Power Sources*, vol.256, pp.324–328, 2014.

[136] P. Lanz, and P. Novák, "Combined In Situ Raman and IR Microscopy at the Interface of a Single Graphite Particle with Ethylene Carbonate/Dimethyl Carbonate," *Journal of The Electrochemical Society* , vol.161 , pp.A1555–A1563, January 2014.

[137] P. Lanz, C. Villevieille, and P. Novák, "Electrochemical activation of Li2MnO3 at elevated temperature investigated by in situ Raman microscopy," *Electrochimica Acta*, vol.109, pp.426–432, October 2013.

[138] B.R. Long, M.K.Y. Chan, J.P. Greeley, and A.A. Gewirth, "Dopant Modulated Li Insertion in Si for Battery Anodes: Theory and Experiment," *The Journal of Physical Chemistry C*, vol.115, pp.18916–18921, September 2011.

[139] H. Nakagawa, Y. Domi, T. Doi, M. Ochida, S. Tsubouchi, T. Yamanaka, T. Abe, and Z. Ogumi, "In Situ Raman Study of Graphite Negative-Electrodes in Electrolyte Solution Containing Fluorinated Phosphoric Esters," *Journal of The Electrochemical Society* , vol.161 , pp.A480–A485, January 2014.

[140] H. Nakagawa, Y. Domi, T. Doi, M. Ochida, S. Tsubouchi, T. Yamanaka, T. Abe, and Z. Ogumi, "In situ Raman study on the structural degradation of a graphite composite negative-electrode and the influence of the salt in the electrolyte solution," *Journal of Power Sources*, vol.236, pp.138–144, August 2013.

[141] H. Nakagawa, Y. Domi, T. Doi, M. Ochida, S. Tsubouchi, T. Yamanaka, T. Abe, and Z. Ogumi, "In situ Raman study on degradation of edge plane graphite negative-electrodes and effects of film-forming additives," *Journal of Power Sources*, vol.206, pp.320–324, May 2012.

[142] S. Pérez-Villar, P. Lanz, H. Schneider, and P. Novák, "Characterization of a model solid electrolyte interphase/carbon interface by combined in situ Raman/Fourier transform infrared microscopy," *Electrochimica Acta*, vol.106, pp.506–515, September 2013.

[143] R. Schmitz, R. Ansgar Müller, R. Wilhelm Schmitz, C. Schreiner, M. Kunze, A. Lex-Balducci, S. Passerini, and M. Winter, "SEI investigations on copper electrodes after lithium plating with Raman spectroscopy and mass spectrometry," *Journal of Power Sources*, vol.233, pp.110–114, July 2013.

[144] J. Shu, M. Shui, D. Xu, S. Gao, T. Yi, D. Wang, X. Li, and Y. Ren, "Design and comparison of ex situ and in situ devices for Raman characterization of lithium titanate anode material," *Ionics*, vol.17, pp.503–509, 2011.

[145] C. Sole, N.E. Drewett, and L.J. Hardwick, "Insitu Raman study of lithium-ion intercalation into microcrystalline graphite," *Faraday Discussions*, vol.172, pp.223–237, 2014.

[146] P. Novák, J.-C. Panitz, F. Joho, M. Lanz, R. Imhof, and M. Coluccia, "Advanced in situ methods for the characterization of practical electrodes in lithium-ion batteries," *Journal of Power Sources*, vol.90, pp.52–58, September 2000.

[147] G. Turrell, 1 - The Raman Effect BT - Raman Microscopy, in: Academic Press, London, 1996: pp. 1–25.

[148] D. V Esposito, J.B. Baxter, J. John, N.S. Lewis, T.P. Moffat, T. Ogitsu, G.D. O'Neil, T.A. Pham, A.A. Talin, J.M. Velazquez, and B.C. Wood, "Methods of photoelectrode characterization with high spatial and temporal resolution," *Energy & Environmental Science*, vol.8, pp.2863–2885, 2015.

[149] X. Chen, E. Pomerantseva, P. Banerjee, K. Gregorczyk, R. Ghodssi, and G. Rubloff, "Ozone-Based Atomic Layer Deposition of Crystalline V2O5 Films for High Performance Electrochemical Energy Storage," *Chemistry of Materials*, vol.24, pp.1255–1261, April 2012.

[150] W.K. Schomburg, and C. Goll, "Design optimization of bistable microdiaphragm valves," *Sensors and Actuators A: Physical*, vol.64, pp.259–264, 1998.

[151] S.T. Koev, W.E. Bentley, and R. Ghodssi, "Interferometric readout of multiple cantilever sensors in liquid samples," *Sensors and Actuators B: Chemical*, vol.146, pp.245–252, 2010.

[152] R. Baddour-Hadjean, J.P. Pereira-Ramos, C. Navone, and M. Smirnov, "Raman Microspectrometry Study of Electrochemical Lithium Intercalation into Sputtered Crystalline V2O5 Thin Films," *Chemistry of Materials*, vol.20, pp.1916–1923, March 2008.

[153] C. Delmas, H. Cognac-Auradou, J.M. Cocciantelli, M. Ménétrier, and J.P. Doumerc, "The LixV2O5 system: An overview of the structure modifications induced by the lithium intercalation," *Solid State Ionics*, vol.69, pp.257–264, 1994.

[154] J.M. Cocciantelli, J.P. Doumerc, M. Pouchard, M. Broussely, and J. Labat, "Crystal chemistry of electrochemically inserted LixV2O5," *Journal of Power Sources*, vol.34, pp.103–111, March 1991.

[155] E. Meulenkamp, "In-situ X-ray diffraction of Li intercalation in sol–gel V2O5 films," *Solid State Ionics*, vol.126, pp.235–244, November 1999.

[156] C. Leger, S. Bach, P. Soudan, and J.P. Pereira-Ramos, "Structural and Electrochemical Properties of ω - Lix V2O5 $(0.4 \leq x \leq 3)$ as Rechargeable Cathodic Material for Lithium Batteries," *Journal of The Electrochemical Society*, vol.152, pp.A236–A241, 2005.

[157] C. Delmas, S. Brèthes, and M. Ménétrier, "ω-LixV2O5 — a new electrode material for rechargeable lithium batteries," *Journal of Power Sources*, vol.34, pp.113–118, 1991.

[158] E.A. Meulenkamp, W. van Klinken, and A.R. Schlatmann, "In-situ X-ray diffraction of Li intercalation in sol–gel V2O5 films," *Solid State Ionics*, vol.126, pp.235–244, 1999.

[159] J. Scarminio, A. Talledo, A.A. Andersson, S. Passerini, and F. Decker, "Stress and electrochromism induced by Li insertion in crystalline and amorphous V2O5 thin film electrodes," *Electrochimica Acta*, vol.38, pp.1637–1642, 1993.

[160] C. Navone, J.P. Pereira-Ramos, R. Baddour-Hadjean, and R. Salot, "High-Capacity Crystalline V2O5 Thick Films Prepared by RF Sputtering as Positive Electrodes for Rechargeable Lithium Microbatteries," *Journal of The Electrochemical Society*, vol.153, pp.A2287–A2293, 2006.

[161] R. Baddour-Hadjean, E. Raekelboom, and J.P. Pereira-Ramos, "New Structural Characterization of the LixV2O5 System Provided by Raman Spectroscopy," *Chemistry of Materials*, vol.18, pp.3548–3556, July 2006.

[162] Y. Wang, K. Takahashi, K. Lee, and G. Cao, "Nanostructured vanadium oxide electrodes for enhanced lithium-ion intercalation," *Advanced Functional Materials*, vol.16, pp.1133–1144, 2006.

[163] D.-Y. Yoo, I.-H. Yeo, W. Il Cho, Y. Kang, and S.-I. Mho, "Determination of Li(+) diffusion coefficients in the LixV2O5 (x = 0 - 1) nanocrystals of composite film cathodes.," *Analytical Sciences : The International Journal of the Japan Society for Analytical Chemistry*, vol.29, pp.1083–8, 2013.

[164] E. Potiron, A. Le Gal La Salle, A. Verbaere, Y. Piffard, and D. Guyomard, "Electrochemically synthesized vanadium oxides as lithium insertion hosts," *Electrochimica Acta*, vol.45, pp.197–214, 1999.

[165] F. Lantelme, A. Mantoux, H. Groult, and D. Lincot, "Electrochemical Study of Phase Transition Processes in Lithium Insertion in V 2 O 5 Electrodes ," *Journal of The Electrochemical Society* , vol.150 , pp.A1202–A1208, 2003.

[166] S.K. Soni, B.W. Sheldon, X. Xiao, a. F. Bower, and M.W. Verbrugge, "Diffusion Mediated Lithiation Stresses in Si Thin Film Electrodes," *Journal of the Electrochemical Society*, vol.159, pp.A1520–A1527, 2012.

[167] L. Lou, S. Zhang, W.-T. Park, J.M. Tsai, D.-L. Kwong, and C. Lee, "Optimization of NEMS pressure sensors with a multilayered diaphragm using silicon nanowires as piezoresistive sensing elements," *Journal of Micromechanics and Microengineering*, vol.22, pp.55012, 2012.

[168] A.R. Armstrong, C. Lyness, P.M. Panchmatia, M.S. Islam, and P.G. Bruce, "The lithium intercalation process in the low-voltage lithium battery anode Li1+xV1−xO2," *Nat Mater*, vol.10, pp.223–229, 2011.

[169] J. Laconte, D. Flandre, and J.-P. Raskin, "Micromachined Thin-Film Sensors for SOI-CMOS Co-Integration.", Springer US, 2006.

[170] N. Fateh, G.A. Fontalvo, and C. and Mitterer, "Structural and mechanical properties of dc and pulsed dc reactive magnetron sputtered V2O5 films," *Journal of Physics D: Applied Physics*, vol.40, pp.7716, 2007.

[171] F. Bianco, K. Fedus, F. Enrichi, R. Pierobon, M. Cazzanelli, M. Ghulinyan, G. Pucker, and L. Pavesi, "Two-dimensional micro-Raman mapping of stress and strain distributions in strained silicon waveguides," *Semiconductor Science and Technology*, vol.27, pp.085009, August 2012.